Multifunctional platforms based on upconversion nanoparticles for applications in nanomedicine

Thèse en cotutelle
Doctorat en chimie

Karina Nigoghossian

Université Laval
Québec, Canada
Philosophiae doctor (Ph.D.)

et

São Paulo State University
Araraquara, Brazil
Docteure

Multifunctional platforms based on upconversion nanoparticles for applications in nanomedicine

Thèse en cotutelle
Doctorat en chimie

Karina Nigoghossian

Sous la direction de :

Denis Boudreau, directeur de recherche
Sidney J. L. Ribeiro, directeur de cotutelle

FICHA CATALOGRÁFICA

N684m

Nigoghossian, Karina
Multifunctional platforms based on upconversion nanoparticles for applications in nanomedicine / Karina Nigoghossian. – Araraquara: [s.n.], 2018
120 p.: il.

Thesis (doctor) – Universidade Estadual Paulista, Instituto de Química
Advisor: Sidney José Lima Ribeiro
Advisor: Denis Boudreau

1. Surface plasmon resonance. 2. Biomedical materials. 3. Nanoparticles. 4. Rare earth metals. 5. Luminescence. I. Title.

Elaboração: Seção Técnica de Aquisição e Tratamento da Informação
Biblioteca do Instituto de Química, Unesp, câmpus de Araraquara

UNIVERSIDADE ESTADUAL PAULISTA

Câmpus de Araraquara

CERTIFICADO DE APROVAÇÃO

TÍTULO DA TESE: "Plataformas multifuncionais baseadas em nanopartículas para conversão ascendente para aplicações em nanomedicina"

AUTORA: KARINA NIGOGHOSSIAN
ORIENTADOR: SIDNEY JOSE LIMA RIBEIRO

Aprovada como parte das exigências para obtenção do Título de Doutora em QUÍMICA, pela Comissão Examinadora:

Prof. Dr. SIDNEY JOSE LIMA RIBEIRO
Departamento de Química Geral e Inorgânica / Instituto de Química - UNESP - Araraquara

Prof. Dr. YOUNES MESSADDEQ
Departamento de Química Geral e Inorgânica / Instituto de Química - UNESP - Araraquara

Prof. Dr. DENIS BOUDREAU
Chemistry Department / Université Laval - Canadá

Prof. Dr. CID BARTOLOMEU DE ARAUJO
Departamento de Física / Universidade Federal de Pernambuco - Recife - PE

Profª. Drª. ANNA MARIE RITCEY
Department of Chemistry / Université Laval

Prof. Dr. MAURICIO DA SILVA BAPTISTA
Departamento de Bioquímica / Universidade de São Paulo - USP - São Paulo

Profa. Dra. ROGÉRIA ROCHA GONÇALVES

Résumé

Dans le domaine biomédical, il y a une demande croissante pour les nanosystèmes multifonctionnels pour effectuer simultanément l'imagerie et la thérapie, en visant le diagnostic précoce et apporter du bénéfice thérapeutique maximal. Les nanoparticules à conversion ascendante d'energie (UCNPs) ont été proposés comme une bio-sonde idéale en raison de leurs avantages uniques liés au phénomène d'*upconversion* présenté par les matériaux contenant des ions lanthanides, c'est-à-dire l'émission visible obtenue sous excitation dans le proche infrarouge (NIR), tels qu'une meilleure pénétration dans les tissus, une bas taux d'autofluorescence et un photo-dommage minimal. De plus, les propriétés luminescentes des ions lanthanides peuvent être utilisées pour la thermométrie en raison de leur forte dépendance sur la température. La thermométrie par luminescence est une technique sans contact et à haute résolution qui a attiré l'attention en nanomédecine puisque la température est un paramètre clé dans le fonctionnement des cellules. Des dommages thermiques aux cellules peuvent être localement photoinduits par l'utilisation de nanostructures métalliques illuminées dans leur bande de résonance plasmon en raison de leur absorptivité élevée. La prémière partie de ce travail implique le développement d'un système multifonctionnel, basé sur des nanocoquilles d'or (AuNSs) décorées avec des UCNPs, pouvant être utilisé pour augmenter et mesurer la température à l'échelle nanométrique. Ce système a été développé dans le but d'éventuelle utilisation comme agent de thérapie photothermique (PTT), dans laquelle la capacité thermométrique des UCNPs permettra d'optimiser les bénéfices thérapeutiques. La synthèse des UCNPs de $NaGdF_4$ dopées avec les ions Yb^{3+} et Er^{3+} a été réalisée par décomposition thermique des précurseurs de fluorure de lanthanide à des températures elévées (> 300 °C) en présence d'un ligand de coordination (l'acide oléique). Les UCNPs ont été synthétisées à trois températures différentes (310, 315 et 320 °C) et caractérisées selon leurs propriétés morphologiques, structurelles et émissives. Compte tenu des applications biologiques prévues, la surface hydrophobe des UCNPs recouverte de chaînes oléate a été modifiée par un revêtement de silice par un processus Stöber modifié au moyen d'une méthode de microémulsion inverse afin d'obtenir une dispersion suffisante dans l'eau. Des nanocristaux monodisperses de $NaGdF_4$:Yb^{3+}:Er^{3+} à conversion ascendante (~ 25 nm de diamètre) ont été obtenus en phases cubique (à 310, 315 °C) et hexagonale (à 320 °C). Les UCNPs dans la phase hexagonale étaient plus appropriés en tant que capteurs de température en raison du rapport faible entre les émissions rouge/vert et une plus grande sensibilité thermique. Le spectre d'émission des UCNP (recouvertes de silice ou d'oléate) a été enregistré à des températures différentes à proximité de la plage physiologique (20–70 °C) et il a présenté des propriétés appropriées pour leur utilisation comme capteur de température, notamment une excellente linéarité (R^2 > 0,99) et une bonne sensibilité (>3 × 10^{-3} K^{-1}). La surface des AuNS a été décorée avec des UCNP recouvertes de silice. La capacité de chauffage des AuNSs@UCNPs a été vérifiée en mesurant l'émission de l'Er^{3+}, ce qui démontre leur potentiel d'application comme agent d'hyperthermie contrôlée par l'utilisation de la fonction de nanothermomètre.

La deuxième partie de ce projet de thèse a été consacrée au développement d'un nanosystème multifonctionnel pouvant être utilisé comme un système de double capture de lumière UV et de mesure de température. Le complexe $Eu(tta)_3$ (tta-thénoyltrifluoreacetonate) a été préparé *in situ* dans la coquille de silice des UCNPs de $NaGdF_4:Yb^{3+}:Er^{3+}$. Un nanothermomètre à double mode a été obtenu à partir du signal de fluorescence généré grâce à la conversion ascendante (proche infrarouge → visible) par les ions Er^{3+} ainsi que par l'émission par la conversion descendante excitée dans l'UV du complexe $Eu(tta)_3$. Les mesures ont été prises près de la plage de température physiologique (20−50 °C) et montrent une excellente linéarité ($R^2 > 0,99$) et une sensibilité thermique relativement élevée ($\geq 1,5\% \cdot K^{-1}$). L'utilité du complexe $Eu(tta)_3$ présent dans la coquille de silice comme capteur de la lumière UV a été démontré par la dépendance de la luminescence de l'ion Eu^{3+} sur la durée de l'exposition à la lumière UV. Le matériau obtenu présente un potentiel d'application dans les thérapies activées par la lumière, telles que la thérapie photodynamique (PDT) et la PTT, qui nécessitent généralement une lumière UV ou bleue pour l'excitation. Le contrôle de la dose de lumière delivrée aux tissus a une grande importance dans ces procédures thérapeutiques pour éviter le photodommage aux tissus environnants. La fonction thermomètre est utile pour guider de tels processus (PDT et PTT) en synergie avec le dosimètre d'UV.

Mots-Clés : nanoparticules à conversion ascendante d'energie, ions lanthanides, luminescence, nanothermométrie, hybrides organiques-inorganiques, thérapie photothermique.

Abstract

In the biomedical field, there is an increasing demand for multifunctional nanosystems to perform imaging and therapy simultaneously, aiming at early diagnosis and maximum therapeutic benefit. Upconversion nanoparticles (UCNPs) have been proposed as an ideal bio-probe because of their unique advantages related to the upconversion phenomenon presented by materials containing lanthanide ions, *e.g.* visible emission obtained under near-infrared (NIR) excitation, such as deep tissue penetration, low autofluorescence background and low photo-damage. Moreover, the luminescent properties of lanthanide ions may be used for thermometry because of a strongly temperature-dependent effect. Luminescence nanothermometry is a noncontact and high-resolution technique that has been gaining attention in nanomedicine since temperature is a fundamental parameter in events that occur in cells. The thermal damage of cells may be locally photoinduced by using metal nanostructures illuminated at their localized surface plasmon resonance (LSPR) band because of the enhancement of light absorption. In this work, a multifunctional system was designed combining gold nanoshells (AuNSs) and UCNPs intended as an optical heater and temperature probe at the nanoscale. This system was studied aiming its application as an agent for photothermal therapy (PTT), guided by the thermometer capacity of UCNPs, which allows to optimize the therapeutic benefits. The synthesis of $NaGdF_4$ UCNPs doped with ions Yb^{3+}:Er^{3+} was performed via the thermal decomposition of lanthanide ion fluoride precursors at high temperatures (>300 °C) in the presence of a coordinating ligand (oleic acid). UCNPs were synthesized at three different temperatures (310, 315 and 320 °C) and characterized in terms of morphological, structural and emission properties. In view of the intended biological applications, the surface of hydrophobic oleate-capped UCNPs was modified by a silica coating to achieve sufficient water dispersibility, through a modified Stöber process by a reverse micro-emulsion method. Monodisperse $NaGdF_4$:Yb^{3+}:Er^{3+} upconverting nanocrystals (~25 nm dia.) were obtained in cubic (at 310, 315 °C) and hexagonal phase (at 320 °C). The UCNPs in the hexagonal phase showed to be more suitable for application as a temperature sensor, because of its lower red-to-green emission ratio and higher thermal sensitivity. The emission spectra of $NaGdF_4$:Yb^{3+}:Er^{3+} (oleate- or silica-coated) UCNPs were measured at different temperatures in the vicinity of the physiological temperature range (20-70 °C) and presented suitable properties for application as a temperature sensor, such as excellent linearity (R^2 >0.99) and sensitivity (>3 × 10^{-3} K^{-1}). The surface of AuNSs were decorated with silica-coated UCNPs. The heating capacity of such nanocomposites (AuNSs@UCNPs) was verified by monitoring the Er^{3+} emission, enabling potential application as a hyperthermia agent controlled by the nanothermometer function. In a second part of this thesis, a multifunctional nanosystem was designed and applied as a dual sensor of ultraviolet (UV) light and temperature. $Eu(tta)_3$ (tta-thenoyltrifluoroacetonate) complex was prepared *in situ* over the silica shell of $NaGdF_4$:Yb^{3+}:Er^{3+} UCNPs. A dual-mode nanothermometer-UV sensor was obtained from the combination of NIR to visible upconversion fluorescence signal of Er^{3+} ions and the UV-excited downshifted emission

from the $Eu(tta)_3$ complex. Measurements were performed near the physiological temperature range (20-50 °C) revealing excellent linearity (R^2 > 0.99) and relatively high thermal sensitivities (>1.5%·K^{-1}). The $Eu(tta)_3$ complex present in the silica shell was also demonstrated as a UV sensor because of the Eu^{3+} luminescence dependence on UV light exposure. The obtained material shows potential for application in light activated therapies, such as photodynamic therapy (PDT) and PTT, which typically require UV or blue light for excitation. The control of light dose released to the tissue is of great importance in these therapeutic procedures to avoid photodamage to the surroundings. The thermometer function is useful to guide such therapeutic processes (PDT and PTT) synergistically with the UV dosimeter.

Keywords: upconversion nanoparticles, lanthanide ions, luminescence, nanothermomety, organic-inorganic hybrids, photothermal therapy.

Resumo

Na área biomédica, existe uma crescente demanda por nanossistemas multifuncionais para realização de imageamento e terapia simultaneamente, visando um diagnóstico precoce e máximo benefício terapêutico. Nanopartículas para conversão ascendente de energia (UCNPs) vêm sendo propostas como a sonda biológica ideal devido às suas vantagens únicas relacionadas ao fenômeno de *upconversion* apresentado por materiais contendo íons lantanídeos, isto é, emissão no visível obtida sob excitação no infravermelho, tais como penetração profunda nos tecidos, uma baixa taxa de autofluorescência e um fotodano mínimo. Além disso, as propriedades luminescentes dos íons lantanídeos podem ser usadas para termometria por serem fortemente dependentes da temperatura. A termometria luminescente é uma técnica de não-contato e alta resolução que vem ganhando atenção na nanomedicina uma vez que a temperatura é um parâmetro fundamental para o funcionamento das células. Danos térmicos às células podem ser localmente fotoinduzidos pelo uso de nanoestruturas metálicas iluminadas em sua banda de ressonância plasmônica por causa da sua elevada absortividade. A primeira parte deste trabalho consiste no desenvolvimento de um sistema multifuncional baseado em nanocascas de ouro (AuNSs) decoradas com UCNPs podendo ser utilizadas para aumentar e medir a temperatura em escala nanométrica. Este sistema foi desenvolvido com a finalidade de uma eventual utilização como agente em terapia fototérmica (PTT), na qual a capacidade termométrica das UCNPs permitirá otimizar os benefícios terapêuticos. A síntese das UCNPs de $NaGdF_4$ dopadas com os íons Yb^{3+} e Er^{3+} foi realizada via decomposição térmica de precursores de fluoreto de lantanídeo a altas temperaturas (> 300 °C) na presença de um ligante coordenante (o ácido oleico). As UCNPs foram sintetizadas em três diferentes temperaturas (310, 315 e 320 °C) e caracterizadas segundo suas propriedades morfológicas, estruturais e emissivas. Levando-se em conta as aplicações biológicas pretendidas, a superfície hidrofóbica das UCNPs recoberta por cadeias de oleato foi modificada utilizando um revestimento de sílica via um processo Stöber modificado por meio de um método de microemulsão reversa para obter uma dispersão suficiente em água. Nanocristais monodispersos de $NaGdF_4$:Yb^{3+}:Er^{3+} para conversão ascendente (~ 25 nm de diâmetro) foram obtidos nas fases cúbica (a 310, 315 °C) e hexagonal (a 320 °C). As UCNPs na fase hexagonal mostraram-se mais apropriadas como sensores de temperatura, devido a menor razão entre as emissões vermelho/verde e maior sensibilidade térmica. O espectro de emissão das UCNPs (recobertas por sílica ou por oleato) foi registrado a diferentes temperaturas na proximidade do intervalo fisiológico (20–70 °C) e apresentou propriedades adequadas para sua aplicação como sensor de temperatura, especialmente uma excelente linearidade (R^2 > 0,99) e uma boa sensibilidade (>3 × 10^{-3} K^{-1}). A superfície das AuNSs foi decorada com UCNPs recobertas por sílica. A capacidade de aquecimento das AuNSs@UCNPs foi verificada medindo-se a emissão do Er^{3+}, a qual demonstra seu potencial como agente em hipertermia controlada pela utilização da função de nanotermômetro. A segunda parte deste projeto de tese foi dedicada ao desenvolvimento de um nanosistema multifuncional podendo ser utilizado como um sistema

de dupla captura de luz UV e medida de temperatura. O complexo $Eu(tta)_3$ (tta-tenoiltrifluoroacetonato) foi preparado *in situ* na casca de sílica das UCNPs de $NaGdF_4:Yb^{3+}:Er^{3+}$. Um nanotermômetro de modo duplo foi obtido a partir do sinal de fluorescência gerado graças à conversão ascendente (infravermelho próximo → visível) pelos íons Er^{3+} juntamente à emissão por conversão descendente excitada no UV do complexo $Eu(tta)_3$. As medidas foram realizadas próximo à faixa de temperatura fisiológica (20—50 °C) revelando uma excelente linearidade ($R^2 > 0,99$) e uma sensibilidade térmica relativamente alta ($\geq 1,5\% \cdot K^{-1}$). A utilidade do complexo de $Eu(tta)_3$ presente na casca de sílica como sensor de luz UV foi demonstrado pela dependência da luminescência do íon Eu^{3+} sob a duração da exposição à luz UV. O material obtido apresenta potencial para aplicação em terapias ativadas pela luz, tais como a terapia fotodinâmica (PDT) e a PTT, as quais tipicamente requerem luz UV ou azul para excitação. O controle da dose de luz liberada para os tecidos tem grande importância nestes procedimentos terapêuticos para evitar o fotodano aos tecidos circundantes. A função de termômetro é útil para guiar tais processos (PDT e PTT) simultaneamente com o dosímetro de UV.

Palavras-chave: nanopartículas para conversão ascendente de energia, íons lantanídeos, luminescência, nanotermometria, híbridos orgânicos-inorgânicos, terapia fototérmica.

Contents

Résumé v
Abstract vii
Resumo ix
List of figures xiv
List of tables xvi
List of abbreviations and symbols xvii
Acknowledgments xx
Foreword xxiii
Chapter 1. General introduction and statement of the problem 27
1.1. Multifunctional theranostic nanosystems 27
1.2. Luminophores for biomedical applications 28
1.3. Lanthanide-based upconversion nanoparticles 29
1.4. Lanthanide-based luminescent nanothermometry 30
1.5. Photothermal therapy 32
1.6. Multifunctional systems for luminescent thermometry and plasmonic heating 32
References 33
Chapter 2. Theory and review of literature 41
2.1. Basic mechanisms of photoluminescence 41
2.2. Lanthanide photoluminescence properties 42
2.3. Upconversion luminescence mechanisms 43
2.4. Temperature measurement 45
2.5. Luminescence thermometry 46
2.6. Gold nanoparticles for bioapplications 48
References 50
Chapter 3. Objectives 56
3.1. General objective 56
3.2. Specific objectives 56
Chapter 4. Methods 58
4.1. Synthesis procedures 58
4.1.1. Thermal decomposition synthesis 58
4.1.1.1. Synthesis of Gd^{3+}:Yb^{3+}:Er^{3+} trifluoroacetate precursor 58
4.1.1.2. Synthesis of Yb^{3+}:Er^{3+} co-doped $NaGdF_4$ UCNPs 58
4.1.2. Silica coating of $NaGdF_4$:Yb^{3+}:Er^{3+} UCNPs 59
4.1.3. Synthesis of UCNP-metal nanocomposites 59
4.1.4. In situ preparation of the complex $Eu(tta)_3$ at the silica shell of UCNPs 60
4.2. Characterizations 60
4.2.1. Structural characterization 60
4.2.2. Optical characterization 61
4.2.3. Temperature sensing 61
4.2.3.1. Er^{3+} emission-based thermometer 61
4.2.3.2. Eu^{3+} emission-based thermometer 62
4.2.3.3 Thermal sensitivity 63
4.2.4. Photothermal effect 64
4.2.5. UV light sensing 64
References 64

Chapter 5. Upconversion nanoparticle-decorated gold nanoshells for near-infrared induced heating and thermometry 67
Résumé 67
Resumo 67
Abstract 68
5.1. Introduction 68
5.2. Experimental details 70
5.2.1 Materials 70
5.2.2. Synthesis of Yb^{3+}:Er^{3+} co-doped $NaGdF_4$ UCNPs 70
5.2.3. Silica coating of $NaGdF_4$:Yb^{3+}:Er^{3+} UCNPs 71
5.2.4. Synthesis of SiO_2@Au nanoshells 71
5.2.4.1. Silica cores 71
5.2.4.2. SiO_2@NH_2 71
5.2.4.3. Gold seeds 71
5.2.4.4. SiO_2@seeds 72
5.2.4.5 Shell growth 72
5.2.5. Synthesis of nanocomposite AuNSs@UCNPs 72
5.2.5.1. UCNPs@SiO_2–NH_2 72
5.2.5.2. UCNP attachment on AuNSs 72
5.2.6. Morphological and structural characterization 73
5.2.7. Optical characterization 73
5.2.8. Temperature sensing 73
5.2.9. Photothermal effect 73
5.3. Results and discussion 73
5.3.1. Oleate-capped $NaGdF_4$:Yb^{3+}:Er^{3+} UCNPs 73
5.3.2. Silica-coated $NaGdF_4$:Yb^{3+}:Er^{3+} UCNPs 76
5.3.3. Temperature sensing 77
5.3.4. Photothermal effect 80
5.4. Conclusions 83
References 83
Chapter 6. UV and temperature-sensing based on $NaGdF_4$:Yb^{3+}:Er^{3+}@SiO_2−$Eu(tta)_3$ 87
Résumé 87
Resumo 87
Abstract 88
6.1. Introduction 88
6.2. Materials and methods 89
6.2.1. Materials 89
6.2.2. Synthesis of Yb^{3+}:Er^{3+} co-doped $NaGdF_4$ UCNPs 89
6.2.3. Silica coating of $NaGdF_4$:Yb^{3+}:Er^{3+} UCNPs 90
6.2.4. Preparation of $NaGdF_4$:Yb^{3+}:Er^{3+}@SiO_2–$Eu(tta)_3$ 90
6.2.5. Characterization 91
6.3. Results and discussion 91
6.4. Conclusions 98
References 99
Chapter 7. Upconversion nanocomposites for PDT 104
7.1. Introduction 104
7.2. Materials and methods 107
7.2.1 Materials 107

7.2.2. Preparation of UCNPs@SiO_2-PS 107
7.2.3. PDT assays 107
7.3. Results and discussion 108
7.4. Conclusions 114
References 115
Chapter 8. Conclusions 118
References 120

List of figures

Figure 2.1. Energy level scheme for a simplified representation of luminescence process…….. 42

Figure 2.2. Mechanisms to convert low-energy photon pump sources into higher energy output: Simultaneous two-photon absorption (STPA), Second-harmonic generation (SHG), Upconversion (UC). The horizontal dashed (solid) lines indicate virtual (discrete) levels…… 44

Figure 2.3. Energy transfer mechanisms: excited state absorption (ESA) and energy transfer upconversion (ETU). (S: sensitizer ion, A: activator ion) …… 44

Figure 2.4. Extinction spectra of aqueous solutions of gold nanoparticles in different shapes: spheres, rods and shells…… 49

Figure 4.1. Schematic energy-level diagram of Yb^{3+} and Er^{3+} and mechanism of upconversion emissions under 980 nm laser excitation…… 62

Figure 4.2. Schematic energy-level diagram showing the mechanism of energy transfer from tta to Eu^{3+} and downshifting emission under UV excitation……... 63

Figure 5.1. (a) TEM images of $NaGdF_4:Yb^{3+}:Er^{3+}$ nanoparticles prepared at 310, 315 and 320 °C and (b) their respective particle size distributions. ……... 74

Figure 5.2. XRD patterns of $NaGdF_4:Yb^{3+}:Er^{3+}$ UCNPs prepared at different temperatures. Reference diffraction peaks corresponding to cubic and hexagonal $NaGdF_4$. ……... 75

Figure 5.3. Upconversion emission spectra obtained using 980 nm laser pumping at different powers for α-UCNPs (a) and β-UCNPs (c). Integrated intensity (areas) *vs*. pumping intensity for α-UCNPs (b) and β-UCNPs (d). …….. 76

Figure 5.4. (a) TEM image and (b) particle-size distribution of silica-coated UCNPs. …….. 77

Figure 5.5. Schematic energy level diagram of Yb^{3+} and Er^{3+} and the mechanism of upconversion emissions under 980 nm laser excitation. ……. 78

Figure 5.6. Upconversion emission spectra ($\lambda_{exc.}$ 980 nm) at different temperatures (20–70 °C) of α-UCNPs (a), β-UCNPs (b), and β -UCNPs@SiO_2 (c). Boltzmann's plots (d). …….. 79

Figure 5.7. Thermal sensitivities of α-UCNPs, β-UCNPs and silica-coated β -UCNPs. 80

Figure 5.8. (a) TEM image and (b) extinction spectrum of AuNSs@UCNPs. ……. 81

Figure 5.9. Upconversion emission spectra ($\lambda_{exc.}$ 980 nm) for different laser powers of AuNSs@UCNPs (a) and UCNPs@SiO_2 (b). Calculated temperature values (c). …….. 82

Figure 6.1. TEM images of (a) UCNPs and (b) UCNPs@SiO_2. (c) X-ray diffraction pattern and reference diffraction peaks corresponding to hexagonal $NaGdF_4$ (JCPDS file 27-0699). (d) Upconversion emission spectra (λ_{exc} 980 nm) at different temperatures (293 and 323 K) of UCNPs@SiO_2. 92

Figure 6.2. (a) Excitation (λ_{em} 615 nm) and (b) emission spectra for the complex $[Eu(tta)_3(H_2O)_2]$ (black), the compound $[Eu(tta)_3$–host] (red), and UCNPs@SiO_2-$Eu(tta)_3$ (blue). Spectra of $[Eu(tta)_3(H_2O)_2]$ and $[Eu(tta)_3$–host] were adapted from Molina *et al*. 93

Figure. 6.3. Emission spectra of UCNPs@SiO_2–$Eu(tta)_3$ at different temperatures (293–323 K): under (a) UV and (b) NIR excitation. Insets: Corresponding luminescent photographs. Thermal calibration curves: (c) fluorescence intensity (integrated area) vs temperature (λ_{exc} 352 nm) and (d) ln(FIR) vs inverse temperature (λ_{exc} 980 nm). 94

Figure 6.4. Linear function between real and calculated temperature for Er^{3+}- and Eu^{3+}-based thermometers. 95

Figure 6.5. Relative thermal sensitivity (S_r) as a function of temperature for Er^{3+}/Yb^{3+} system (green) and for Eu(tta) system (red). 96

Figure 6.6. Upconversion emission spectra ($\lambda_{exc.}$ 980 nm) and calculated temperature values at different laser powers. 97

Figure 6.7. (a) Emission spectra (λ_{exc} 352 nm) of UCNPs@SiO_2–$Eu(tta)_3$ after different periods of exposure to UV light. (b) Fluorescence intensity (integrated area) under UV (352 nm) and NIR (980 nm) excitation and fluorescence intensity ratio between Eu^{3+} and Er^{3+} emissions vs time (the solid line represents the exponential fit curve). 98

Figure 7.1. Jablonski diagram adapted for a typical photoactivation process. Vibrational sub-levels are not shown for reasons of clarity. 105

Figure 7.2. Chemical structures of halogen-xanthene PDT sensitizers used in the present work. 106

Figure 7.3. TEM image and particle-size distribution of UCNPs@SiO2-PS. 108

Figure 7.4. Absorption spectra of ethanolic solution of PSs (eosin, erythrosin and rose bengal) and upconversion emission spectrum of UCNPs ($NaGdF_4$:Yb^{3+}:Er^{3+}@SiO_2)..... 109

Figure 7.5. Absorption spectra for initial PS solution (black) and for the supernatant collected after the incorporation for UCNPs@SiO_2 (red) and UCNPs@SiO_2-NH_2 (blue) for three initial PS concentrations (10, 50 and 100 nM). 110

Figure 7.6. Excitation (green) and emission (red) spectra for PS-containing UCNPs@SiO_2. 111

Figure 7.7. Upconversion emission spectra pumping at different powers for PS-containing UCNPs@SiO_2 with concentrations: 10, 50 and 100 nM. 112

Figure 7.8. Red-to-green emission intensity ratio for UCNPs@SiO_2-PS (10, 50 and 100 are PS concentrations in nM). Control: PS-free UCNPs@SiO_2. 113

Figure 7.9. Singlet oxygen decay curve and exponential fit for EO (λ_{exc} 516 nm), ER (λ_{exc} 526 nm) and RB (λ_{exc} 549 nm) in UCNPs@SiO_2 dispersions in D_2O with PS concentrations of 10, 50 and 100 nM. Control: PS free in D_2O solution. 114

List of tables

Table 6.1. Calibration parameters of the dual-mode thermometer under UV and NIR excitations. 96

Table 6.2. Maximum relative thermal sensitivity of Yb^{3+}:Er^{3+} doped UCNPs. 97

Table 6.3. Maximum relative thermal sensitivity of Eu^{3+}-based thermometers. 97

Table 7.1. Maximum excitation and emission wavelengths for PS-containing UCNPs@SiO_2. 111

Table 7.2. Singlet oxygen lifetimes (τ) obtained from decay curves for the samples. 114

List of abbreviations and symbols

$^1O_2$	singlet oxygen
α	crystal cubic phase
β	crystal hexagonal phase
λ	wavelength
λ_{em}	emission wavelength
λ_{exc}	excitation wavelength
ν	frequency
∂T	temperature uncertainty
A	active luminescent center in the ground state
A*	active luminescent center in the excited state
Abs $_{free}$	absorbance of PS free in solvent
Abs $_{initial}$	absorbance of PS initial solution
Aji	spontaneous emission rate
APTES	(3-aminopropyl)triethoxysilane
AuNSs	gold nanoshells
BC	bacterial cellulose
ClAlPc	chloroaluminum phtalocyanine
D_2O	deuterium oxide
DLS	dynamic light scattering
E	energy of the level
ΔE	energy gap separating two excited states
EO	eosin B
EPR	enhanced permeation and retention
ER	erythrosine B
ESA	excited-state absorption
ETU	energy transfer upconversion
FIR	fluorescence intensity ratio
g	degeneracy of the state
GFP	green fluorescent protein

h	Planck constant
HE	haematoxylin and eosin
ICDD	International Centre for Diffraction Data
I_{em}	intensity of emission
I_{ex}	pumping intensity
ISC	intersystem crossing
JCPDS	joint committee on powder diffraction standards
k_B	Boltzmann constant
Ln^{3+}	trivalent lanthanide ions
MSNPs	mesoporous silica nanoparticles
n	number of infrared photons
NIR	near-infrared
NIR-I	first biological window
NIR-II	second biological window
NIR-III	third biological window
NR	non-radiative pathway
OIH	organic-inorganic hybrid
OPO	optical parametric oscillator
PEG	polyethylene glycol
PDT	photodynamic therapy
PL	photoluminescence emission spectrum
PLE	photoluminescence excitation spectrum
PS	photosensitizer
PTT	photothermal therapy
Q	experimental parameter
QDs	quantum dots
R	radiative pathway
R^2	regression coefficient
RB	rose bengal
RSD	relative standard deviation
S	absolute thermal sensitivity

S_0	singlet ground state
S_1	singlet excited state
S_r	relative thermal sensitivity
SERS	surface-enhanced Raman scattering
SHG	second-harmonic generation
SPR	surface plasmon resonance
STPA	simultaneous two-photon absorption
T	absolute temperature
TEM	transmission electron microscopy
TEOS	tetraethylorthosilicate
T_1	triplet excited state
tta	thenoyltrifluoroacetonate
UC	upconversion
UCNPs	upconversion nanoparticles
UCNPs@SiO_2	silica coated upconversion nanoparticles
UV	ultraviolet
XRD	X-ray diffraction

Acknowledgments

I am deeply grateful to my supervisor Prof. Dr. Sidney José Lima Ribeiro, who guided me since I was an undergraduate student, having a huge role in my professional development. Although today I cannot see myself doing anything but academic research, since the beginning he gave me the freedom to fulfill or not this fated destiny in science by encouraging me to experience different work fields – from industry to volunteering –, and by allowing me to collaborate with diverse research groups in Brazil and abroad. My way back to research always occurred spontaneously, and thus make me feel safe about my present career choices. I am also grateful to him for giving me autonomy to conceive this thesis, for always propose new ideas, discuss the results and patiently review the manuscripts. And for never doubting my ability to handle very broad research topics, despite my pharmaceutical background.

I would like to express my sincere gratitude to my supervisor Prof. Dr. Denis Boudreau for the continuous support and guidance. For his trust in my work by giving me opportunity to be part of his group. For being always concerned about the management and progress of the research, the students' motivation and the integration of group members, while always keeping a pleasant environment. For carefully reading earlier drafts of this thesis and other scientific texts and giving valuable feedback. And specially for teaching me that I am in control of my work, not the opposite.

I also want to thank Prof. Dr. Younès Messaddeq for the continuous support of my PhD studies, for the essential efforts to make this cotutelle possible and for the warm reception in Québec along with Dr. Sandra Helena Messaddeq. I am glad to still be professionally involved with my very first professor of General and Inorganic Chemistry in the early days of Pharmacy School, one of the most inspiring personalities I have met, being an example of motivation, enthusiasm, and immense knowledge. I cannot fail to mention about how grateful I am to him for giving me the once in a lifetime opportunity to go to France in 2008 in a journey of self-discovery, in one of the most inspirational research experiences I had.

Besides my supervisors, I would like to thank the rest of my thesis committee: Prof. Dr. Cid B. de Araújo, Prof. Dr. Rogéria R. Gonçalves, Prof. Dr. Mauricio S. Baptista and Prof. Dr. Anna Ritcey, for reviewing the written work, for participating in the final oral examination, and for the valuable comments, criticisms and suggestions that brought insights from different perspectives. Specially, Prof. Dr. Mauricio S. Baptista, who gave access to the laboratory and research facilities. I am grateful for the stimulating discussions and for opening a new perspective for my work during the last year of my PhD.

I thank Prof. Dr. Claudine Allen for permitting me to use lab facilities for the synthesis of nanoparticles and the group members Dr. Marie-Ève Lecavalier, Dr. Sébastien Lamarre and Dr. Marc-Antoine Langevin for helping me in the lab.

I thank my kind fellow labmates from Boudreau's group: Dr. Samuel Ouellet, Dr. Jéremie Asselin, Dr. Alexandre Grégoire, Dr. Josée Richard-Daniel, Dr. Félix-Antoine Lavoie, Philippe Legros, Marie-Pier Lambert, Mélina Drouin, Alexe Grenier, Nicolas Fontaine, Lydia Parent, Marie-Pier Côté. I learned so

much from you, whether in the exciting group meetings or during the fun moments in the lab, that I was always worried about how I could contribute back to my colleagues. I learnt that in a group in which everyone recognizes the qualities of each other, there is no place for competition and the synergism bring excellent results for the team.

I also thank my colleagues from Messaddeq's group: Dr. Yannick Ledemi, Dr. Mathilde Loubier, Dr. Maxime Rioux, Dr. Hssen, Dr. Guilherme Marcondes, Dr. Otávio De Brito Silva and Dr. Rim Baklouti.

I thank colleagues that became friends for life from the Laboratory of Photonic Materials (Unesp): Prof. Dr. Danilo Manzani, Dr. Gustavo Galleani, Dr. Silvia H. Santagneli, Dr. Chanchal Hazra, Dr. Sybele Saska, Dr. Hssen Fares, Dr. Hernane Barud, Dr. Rafael Miguel Sábio, Dr. Molíria V. dos Santos, Dr. Robson Rosa da Silva, Dr. Denise de Salvi, Dr. Maurício Cavicchioli, Livia M. Christovam, Laís Galvão, Laís Roncalho, Fernando Maturi, Juliane Resges Orives, Andreia Monteiro, Samira Stain, York Correales, César Polachini, Tâmara J. Oliveira, Prof. Dr. Sajjad Khan, Prof. Dr. Camila Pereira, Prof. Dr. Mauricio Caiut, Prof. Dr. Édison Pecoraro and Prof. Dr. Marcelo Nalin, among so many others that I crossed paths with in this lab in more than a decade.

To the staff of the Institute of Chemistry of Unesp for the commitment to professional formation of the students and continuous improvement, specially to Dr. Sérgio Luís Scarpari, Rafael R. Domeneguetti, Luiz F. Aquino, Valéria C. M. Bizelli and Wennia L. S. dos Santos.

Juninho Moura Basque for the friendship, for helping me to improve my communication skills in so many languages and for constant psychological support.

I would to express my appreciation to my family: my parents Lilian and Rubens, to my brother Rubinho and my sister in law Violeta for inspiring me and for moral support throughout my life in general. I also thank my dear friends Dayana, Josiane, Priscila and Silvia for being by my side and for bringing happiness to my life.

Finally, I acknowledge the financial support from Brazilians Agencies FAPESP and CAPES-CNPq (process numbers 99999.010867/2014-07 and 141253/2014-2). The Natural Sciences and Engineering Research Council of Canada and the *Fonds de recherche du Québec-Nature et Technologies* are also acknowledged for their financial support.

To all the women who walk down their own paths in considerable disadvantage
and fight daily for their independence.
May we evolve towards equality strengthened by our differences.
Together we will be stronger.

Foreword

This thesis has been developed under a cotutelle program between Université Laval (Québec, Canada) and São Paulo State University (Araraquara, Brazil) under the supervision of Prof. Denis Boudreau and Prof. Sidney J. L. Ribeiro in the scope of the Joint International Research Unit (JIRU) UNESP-Laval. The purpose of the project was to investigate the use of lanthanide-based luminescent nanoparticles for UV-sensing and nanothermometry combined with gold nanoshell-based photothermal therapy in multifunctional nanosystems aiming for biomedical applications.

This thesis is structured in chapters as follows:

Chapter 1 brings a general introduction on how nanotechnology allows the development of multifunctional nanoparticles and to contextualize the quite recent theranostic nanomedicine concept, an integration of diagnostics and therapy in a single nanoplatform seeking to maximize the therapeutic benefits. The components of such system are presented, more specifically the conventional luminescent probes and the advantages of lanthanide-based upconversion nanoparticles for biomedical applications. In addition to the bioimaging function, the use of lanthanides luminescence for nanothermometry and the UCNP-metal nanocomposites as multifunctional system for nanomedicine are addressed.

Chapter 2 is focused on theory and review of literature, which start from the basic mechanisms of photoluminescence and then provide the principles of lanthanide photouminescence with an emphasis on the theory for upconversion luminescence of lanthanide ions. The aspects of temperature measurement techniques are discussed. Special attention is given to the various methods of luminescence thermometry with a focus on biological applications. A comprehensive overview of the use of gold nanoparticles for biomedical application in photothermal therapy is given.

The main motivations and goals of this thesis are highlighted in Chapter 3, as well as the specific objectives that must be met in order to achieve the intended research contribution. Chapter 4 provides the fundamentals behind the experimental methodology chosen concerning the synthesis of nanomaterials and the post-synthesis surface modification strategies, and the characterization methodology used to investigate structural and optical properties as well as the promising applications in thermometry and UV light sensing. The results and discussions obtained generated two scientific papers, presented in Chapters 5 and 6. Chapter 7 presents additional results concerning the development of a upconversion-based nanosystem for use in photodynamic therapy. Chapter 8 concludes the thesis.

Chapter 5 presents the article “Upconversion nanoparticle-decorated gold nanoshells for near-infrared induced heating and thermometry”. This work was devoted to the use of lanthanides and metallic particles for applications in nanomedicine as heater and thermometer under near-infrared excitation. This new nanoplatform is dispersible in an aqueous environment, thus being attractive for guiding light activated hyperthermia therapies to avoid overheating of normal tissues. Modifications with respect to the original article consists of additional paragraph in Section 5.3 about the temperature reaction effect on nanoparticles morphology, size and phase.

Publication details

Authors: Karina Nigoghossian, Samuel Ouellet, Jérôme Plain, Younès Messaddeq, Denis Boudreau, Sidney José Lima Ribeiro

Journal: Journal of Materials Chemistry B

Submitted: 13th June 2017

Accepted: 1st August 2017

Published: 2nd August 2017

DOI: 10.1039/c7tb01621b

The work “UV and temperature-sensing based on $NaGdF_4:Yb^{3+}:Er^{3+}@SiO_2-Eu(tta)_3$” is addressed in Chapter 6. In this paper, the use of lanthanides for sensing applications was explored. The obtained material presented multiple applications in luminescent thermometry, under ultraviolet or near-infrared excitation, and in UV light sensing for applications in nanomedicine to avoid photodamage and excessive heating of non-targeted tissues. Additional information, not present in the original article, are: (i) Linear function between real and calculated temperature for Er^{3+}- and Eu^{3+}-based thermometers (Figure 6.4); (ii) Relative thermal sensitivity (S_r) as a function of temperature for Er^{3+}/Yb^{3+} system (green) and for Eu(tta) system (red) (Figure 6.5); (iii) Maximum relative thermal sensitivity of $Yb^{3+}:Er^{3+}$ doped UCNPs (Table 6.2); (iv) Maximum relative thermal sensitivity of Eu^{3+}-based thermometers (Table 6.3); and (v) Upconversion emission spectra ($\lambda_{exc.}$ 980 nm) and calculated temperature values at different laser powers (Figure 6.6).

Publication details

Authors: Karina Nigoghossian, Younès Messaddeq, Denis Boudreau, Sidney José Lima Ribeiro

Journal: ACS Omega

Submitted: 16th January 2017

Accepted: 3rd May 2017

Published: 15th May 2017

DOI: 10.1021/acsomega.7b00056

The author of this thesis wrote the research project for the evaluation of postgraduate programs of both universities, conceived the experimental plan, performed the experimental work of synthesis and characterization of obtained samples, analyzed the results, presented preliminary findings at the groups meetings, wrote draft manuscripts, and is thus the first author of both manuscripts. The experimental part was performed at the laboratories of the following professors: Prof. Sidney J. L. Ribeiro, head of the Laboratory of Photonic Materials, in the Institute of Chemistry (UNESP) with expertise in luminescent lanthanide-based materials; Prof. Denis Boudreau at Université Laval, who has been heading the investigation of surface plasmon resonance effects in nanoparticle systems for several years; and Prof. Younès Messaddeq, who leads the research activities on materials for optics and photonics including nanostructured materials at the Centre of Optic Photonic and Lasers (COPL), Université de Laval, Québec, Canada. These professors provided guidance for all activities mentioned above, proposing ideas, discussing the results and reviewing the manuscripts, reports and thesis redaction. Samuel Ouellet prepared gold nanoshells samples following a methodology that he developed during his PhD at Prof. Jérôme Plain's laboratory at Université de Technologie de Troyes in France.

The main results were presented in the following conferences:

1. Nigoghossian, K.; Vorpagel, A. J.; Peres, M. F. S.; Primo, F. L.; Tedesco, A. C.; Pecoraro, E.; Messaddeq, Y.; Ribeiro, S. J. L. "Bacterial cellulose-yttrium vanadate nanoparticles composite membranes", at XIII Brazilian Materials Research Society Meeting, João Pessoa, PB, Brazil, 2014 (Oral presentation).
2. Nigoghossian, K.; Ribeiro, S. J. L.; Messaddeq, Y.; Boudreau, D. "Nanoscale thermometry based on core-shell upconverting nanoparticles for biological applications", at 7th International Conference on Optical, Optoelectronic and Photonic Materials and Applications (ICOOPMA 2016), Montréal, QC, Canada, 2016 (Poster presentation).
3. Nigoghossian, K.; Ouellet, S.; Ribeiro, S. J. L.; Messaddeq, Y.; Boudreau, D. "Luminescent nanothermometers based on upconversion nanoparticles for applications in nanomedicine." at XVIII BMIC Brazilian Meeting on Inorganic Chemistry and 7th Brazilian Meeting on Rare Earths, São Pedro, SP, Brazil, 2016 (Oral presentation).
4. Nigoghossian, K.; S.; Messaddeq, Y.; Boudreau, D.; Ribeiro, S. J. L. "Dual-sensor of UV-light and temperature based on $NaGdF_4:Yb^{3+}:Er^{3+}@SiO_2$-$Eu(tta)_3$ nanoparticles" at 10th International Conference on Nanophotonics (ICNP), Recife, PE, Brazil, 2017 (Poster presentation).
5. Nigoghossian, K.; S.; Messaddeq, Y.; Boudreau, D.; Ribeiro, S. J. L. "UV and temperature sensing based on $NaGdF_4:Yb^{3+}:Er^{3+}@SiO_2$-$Eu(tta)_3$ nanoparticles" at Spectral shaping for biomedical and energy applications (SHIFT), Tenerife, Canary Islands, Spain, 2017 (Poster presentation).

“All sudden understanding is finally the revelation of an acute incomprehension.”
Clarice Lispector

Chapter 1.

General introduction and statement of the problem

1.1. Multifunctional theranostic nanosystems

Current research in the biomedical field is focused on the needs for early and accurate diagnosis, as well as minimally invasive, more efficient, less toxic and fast response treatment techniques. In this direction, nanomedicine is a growing field in which the nanotechnology is applied to pharmaceutical and biomedical sciences to improve the efficacy and safety of conventional medicine.[1,2] Nanometer-scale materials can interact with biological entities in the same (1–100 nm) or close scale length in processes that involve molecules, cells and tissues. Therefore, the use of nanomaterials is a tool to obtain target selectivity and spatiotemporal controlled therapy or sensing.[3–5]

The recent advances in nanotechnology has enabled the fabrication of engineered nanoparticles with tunable optical, electrical and magnetic features by controlling their size, shape, surface chemistry and physicochemical properties.[6] In the biological environment, these features determines the particles' interactions with biological components, such as adsorption of ions and proteins, cellular uptake, biodistribution, and clearance mechanisms.[7] For instance, particle size is a critical parameter that dictates whether the clearance occurs rapidly through the kidneys followed by urinary excretion (<10 nm) or whether a more complex clearance mechanism occurs *via* the liver (>10 nm).[8,9] Administration of therapeutic agents in nanoparticles not only prevents its loss of function by degradation or denaturation, but also modulates the pharmacodynamics and pharmacokinetics, minimizing undesirable side effects.[10]

Specific properties may be combined in a single composite material to obtain a multifunctional platform, in which each component performs its respective function, or they can act synergistically to produce an enhanced effect.[11–14] The development of multifunctional nanosystems for integrated diagnosis and treatment is a growing research field in nanomedicine recently named as theranostic.[15] The multitask particles are aimed to perform diagnosis, drug delivery or therapy activation, and monitoring the therapeutic responses in real time, thus maximizing the therapeutic benefits. The assembly of components in well-defined nanostructures must preserve each function. The core-shell structure is the adequate one for biological applications since the particle dispersion is essential. Such systems usually combine an imaging component at the core, surrounded by a carrier shell able to encapsulate therapeutic agents, and

with a chemically reactive surface to allow for functionalization with a targeting agent for cellular recognition.[16]

The design of carriers for drug delivery explores primarily liposomes[17] and polymers[18]. Rigid nanoparticles may be used as well.[19,] Within them, those based on SiO_2 are by far the most widely used and detailed *in vivo* toxicity studies have been performed.[20–24] Mesoporous silica nanoparticles (MSNPs) with tuned pore-size distribution, pore geometry, and pore network tortuosity, ordered arrays, as well as radial dendritic structures can be achieved by controlling the synthesis parameters.[25] Specific molecules can be retained in pores by electrostatic interactions or H-bonds, as well as by reversible chemical reactions.[26–28] Once in the cytoplasm, the encapsulated molecules can be passively released by mere desorption, by erosion of MPSN or by a combination of both.[29] This process can be triggered by changes in pH,[30–32] temperature,[33,34] light irradiation,[35,36] magnetic field[37] or complementary molecules or functional groups.[38–40]

Concerning targeting strategies, the leaky tumor blood vasculature makes the nanoparticles preferentially accumulate into tumor tissues than their normal counterparts. This mechanism is known as enhanced permeation and retention (EPR).[41] Moreover, with the purpose of selectively delivering the molecules into cells, functionalization of the nanoparticles' surface with bioactive molecules, such as antibodies,[42] peptides,[43] folic acid,[44] aptamers,[45] allows for cell-targeting based on molecule recognition. Such systems may be designed for cytoplasmic delivery and even offer the possibility of designing robust systems for the active targeting of different cell populations.[46]

1.2. Luminophores for biomedical applications

Luminescent materials are widely used for biological applications, mainly for imaging and assays, in processes where light is involved as a response in diagnostics or as the required source of photons for therapy activation (*e.g.* photodynamic therapy or photothermal therapy). The optical properties of biological tissues are a relevant factor to consider when developing luminescent systems for biological applications. The main chromophores present in the tissues (hemoglobin and melanin) present high absorption bands at wavelengths shorter than 600 nm and water begins to absorb significantly at wavelengths greater than 1200 nm. For these reasons, the so-called "biological transparency window" defines the range of wavelengths where the effective tissue penetration of light is maximized because of the reduced absorbance by chromophores present in the tissue. It covers the red and near-infrared (NIR) wavelengths (600–1200 nm).[47]

The excitation light used to perform biomedical imaging is absorbed by the fluorescent contrast agent as well as the absorbing components present in the tissue. The latter is responsible for inducing the autofluorescence effect depending on the wavelength of irradiation. Tissue autofluorescence is a limitation when performing imaging *in vivo* as it reduces the signal to background ratio. Blue light excitation

increases tissue autofluorescence when compared to green excitation, but such an effect remains significant across the visible range. To overcome this limitation, the use of NIR light reduces fluorescence background.[48]

The main conventional luminophores are organic dyes,[49] *e.g.* fluorescein, which is widely used in visualization of the blood flow in the vessels of the retina, choroid and iris,[50] and quantum dots (QDs),[51] semiconductor nanocrystals with high intensity of luminescence, such as CdSe, CdS, and CdTe, typically 1 to 10 nm in size. These luminophores require an excitation source in the UV-visible region and emit photons of lower energy (longer wavelength), in processes involving a single photon. This is known as Stokes emission and the energy loss is called Stokes' shift. Most luminescent materials follow the Stokes' law. The inconvenient features related to this single photon process are due to the wavelength of the excitation source, which presents low penetration by the tissues and causes autofluorescence of biological tissues. Moreover, the high energy of the excitation source required may cause considerable photodamage to biological materials, such as DNA damage and cell death.[52]

The use of luminophores that may be excited with a wavelength within the biological transparency window, as it happens with lanthanide-based upconversion nanoparticles, is a promising solution.

1.3. Lanthanide-based upconversion nanoparticles

Lanthanide-based upconversion nanoparticles (UCNPs) are currently touted as being ideal candidates for bio-probes for biological labeling and imaging because of the possibility to excite their luminescence under near infrared (NIR) illumination.[53] Materials based on trivalent lanthanide ions (Ln^{3+}) may present upconversion properties, *e.g.* visible emission obtained by excitation at NIR region in a multiphoton process. The NIR excitation matches the biological transparency window, allowing deeper tissue penetration depth due to the minimal absorption and scattering of tissues at this spectral region. Additionally, NIR excitation enables sensitive detection without the usual interference from autofluorescence background.[54] Another advantage is the lower photo-damage potential because of the low-energy of NIR photons used for excitation.[55]

Multiphoton luminescence may be obtained with conventional luminophores, organic dyes[56,57] and QDs[58]. However, it requires a very high photon density, provided by a costly high-power pulsed laser, to induce the simultaneous absorption of two photons to accumulate the energy for photon upconversion. On the other hand, the Ln^{3+}-based upconversion emission results from the sequential absorption of photons due to intermediate electronic states able to store one low-energy photon until a second one arrives, thereby being possible to use low power densities to excite the upconversion emission.[59,60]

Nanosized upconversion materials are composed of an inorganic host matrix and doping ions. The main factor in host selection is the low phonon energy to minimize non-radiative losses. The phonon energies of oxides and phosphates are quite high (~500-1000 cm^{-1}).[61] Fluorides hosts, such $NaYF_4$ and

$NaGdF_4$ present low phonon energies (~ 350 cm^{-1}) rendering them ideal hosts.[62] UCNPs are typically doped with ytterbium (Yb^{3+}) sensitizer ions, which absorb infrared radiation and non-radiatively transfer their excitation to activator ions such as erbium (Er^{3+}), thulium (Tm^{3+}) or holmium (Ho^{3+}).[63] Multiplexed biological labeling can be achieved conveniently under a single wavelength excitation by changing activator ions and relative concentrations. Capabilities for the simultaneous imaging and tracking of multiple molecular targets are therefore extended, allowing the classification and differentiation of complex human diseases.[64]

As UCNPs are one of the most important luminescent nanomaterials, the development of multifunctional nanosystems based on lanthanides brings a great impact in nanomedicine advances.[65] The biological application of UCNPs requires water dispersibility, biocompatibility and the possibility of subsequent surface (bio)functionalization. The post-synthetic procedures applied to hydrophobic UCNPs involve two strategies: (i) the deposition of either an additional amphiphilic or silica coating while maintaining the original hydrophobic capping on the UCNPs; (ii) the complete exchange of the original oleic acid ligands by a hydrophilic ligand.[66] Silica coating is the most common technique for nanoparticle surface modification due to its high biocompatibility. Additionally, silica is known to be highly stable and optically transparent, to present abundant Si–OH active bonds available for surface functionalization, and to have high pore volumes where drugs molecules may be stored.[67]

1.4. Lanthanide-based luminescent nanothermometry

The temperature dependence of lanthanide luminescence stimulates its use for thermometry at the nanoscale. Temperature is a fundamental variable that governs diverse intracellular chemical and physical interactions in the life cycle of biological cells.[68] Measuring cell temperature allows optimization of therapeutic processes (*e.g.* hyperthermal tumor treatment).[69] Luminescence nanothermometry is a non-contact and high-resolution technique based on several kinds of materials including rare earth-doped nanoparticles, QDs and organic dyes that allow to determine intracellular temperatures within 0.5 °C.[70]

A thermometer at the nanoscale may be obtained from the fluorescence signal of lanthanide ions, which is a strongly temperature-dependent effect.[71–73] The most used dopant ion in lanthanide-based nanothermometers is Er^{3+} due to the strong temperature dependence of relative intensity of its two green luminescence bands, associated with the effect of thermal equilibrium in the population of excited states.[7475] The earliest work to propose the temperature sensing by using the ratio between the intensity of two emission lines, determined by a Boltzmannian population of the excited states, was made by Berthou and Jörgensen in 1990,[76] in which the upconversion-based luminescent thermometer consisted of a fluoride glass matrix co-doped with Yb^{3+} and Er^{3+} ions. The same ratiometric method was used by Maciel *et al.* in 1995 to study a new class of fluoroindate glasses doped with Er^{3+} using a 1.48 μm continuous wave diode for excitation of visible emission.[77] As an extension to this work, the study on temperature

sensing capability of Er^{3+}-doped fluoroindate glasses was further investigated for a broader temperature range from -250 to 175 °C.[78] The use of nanocrystals for temperature sensing based on the ratiometric method was reported by Alencar *et al.* in 2004.[79] The Er^{3+}-doped $BaTiO_3$ nanocrystals were used for temperature detection by measuring the green upconverted emissions using a 980 nm diode laser as excitation source. The authors then reported that variations in surrounding medium (water, glycerol and air) and temperature (from 27.1 up to 47.1 °C) does not change the sensor sensitivity, considering the possibility of using the $BaTiO_3$:Er^{3+} nanocrystals in biological environments.[80] Besides working in biological fluids, thermometers for bioapplications must present resolution of the order of 0.2 °C, since temperature variations of 1 °C are very significative in biological dynamics. Additionally, the sensor should be nontoxic and soluble in water. Vetrone *et al.*[81] in 2010 were able to an accurate measure of temperature in HeLa cancer cells from 25 °C to its thermally induced death at 45 °C using $NaYF_4$:Yb^{3+}:Er^{3+} UCNPs.

Neodymium ions (Nd^{3+}) are gaining attention in optical thermometry because of its transitions in NIR originated from energy levels that are thermally coupled and thus their populations follow the Boltzmann distribution. Nd^{3+} ions allow absorption and emission in the NIR spectra region, thus being more suitable for biological applications. Recently, new biological transparency windows have been identified in the over 1000 nm spectral region, aiming at bioprobes that offer deeper penetration depth to excitation light as well as deeper propagation of emitted light through biological tissues compared to existing luminophores. Despite the spectral ranges differ depending on the authors, the division considers the water absorption as well as the attenuation coefficient of human skin, blood and fatty tissue. Three distinctive regions are coomonly stabilished: the first biological window (NIR-I) from 700 nm to 950 nm, the second biological window (NIR-II) from 1000 to 1350 nm, and the third biological window (NIR-III) from 1550 to 1870 nm.[82–85]

Silva *et al.*[86] studied the photoluminescence behavior of $Al_4B_2O_9$:Yb^{3+}:Nd^{3+} nanocrystals as a function of temperature. The samples were excited with a laser operating at 977.7 nm to obtain the upconversion emissions from 770 to 940 nm in the temperature range of 26–60 °C. In this system, Yb^{3+} participate as sensitizer in an upconversion process that involves participation of phonons, known as phonon-assisted energy transfer (PAET). In addition, Nd^{3+} may be employed as the sensitizer of upconversion luminescence under 800 nm irradiation in core-shell nanostructures owing to a cascade energy transfer process from Nd^{3+} to Yb^{3+} and a subsequent from Yb^{3+} to activator ion (Er^{3+} or Tm^{3+}).[87–89] This upconversion approach minimize the heating of tissues due to significant lower water absorption at 800 nm compared to conventional excitation at 980 nm. Moura *et al.*[90] reported the temperature dependence of intensity ratio between two spectral lines at 1063.5 nm and 1065.1 nm due to Nd^{3+} transitions in $NdAl_3(BO_3)_4$ nanocrystals by exciting at 811 nm.

The work reported by Kamimura *et al.*[91] applies the ratiometric method to the emission intensity bands from two activator ions present in $NaYF_4$:Yb^{3+}:Ho^{3+}:Er^{3+} nanoparticles. The intensity ratio of the emission peaks in NIR-II (at 1150 nm of Ho^{3+}) and NIR-III (at 1550 nm of Er^{3+}) under NIR-I excitation (at 980 nm) showed almost linearly temperature-dependence for nanoparticles dispersed in both non-polar

and polar media (*i.e.*, cyclohexane and water, respectively) within the biological range of temperatures. The fluorescence *in vivo* imaging of a live mouse was demonstrated by injecting the PEGylated nanoparticles dispersed in physiological saline into the tail vein.

1.5. Photothermal therapy

Target cells can be supressed through heat produced locally by a nanometric system in a therapy modality known as hyperthermia. Heating a cell above its normal temperature leads to cytotoxic effects, for instance, protein denaturation occurs at temperature greater than 39 °C and cells viability is further limited because of the aggregation of these molecules. The effects are more severe as temperature and duration of the treatment increase. For example, above 48 °C, rapid necrotic cell death takes place, bringing higher efficacy, but a lack of selectivity. For this reason, there is a clinical temperature range for hyperthermia process between 41–48 °C.[92]

The heat induction must be well localized to ensure the selectivity of hyperthermia procedures. Localized thermal ablation of cells can be achieved by using a nanoscale material as a heater agent. Such a nanoparticle is a photoabsorber capable of efficiently generate heat under illumination with laser radiation. When light interacts with a nanoparticle, part of the incident photons are scattered and part are absorbed. The absorbed energy is released by a non-radiative pathway (heat release) or by the emission of photons of different energy (luminescence).[92] Therefore, large absorption efficiencies and low luminescence quantum yields are some of the required features of a viable nanoheater agent.

Photothermal therapy (PTT) is an attractive therapeutic modality due to spatial specificity and minimal invasiveness, when compared to most conventional antitumor treatment techniques such as surgery, radiotherapy and chemotherapy.[93] UCNPs are not efficient photoabsorbers because of the low extinction coefficient of lanthanide ions, and thus are not good candidates for PTT.[94] Metallic nanoparticles can be efficient sources for local heating when illuminated at their surface plasmon resonance (SPR) band due to the enhancement of light absorption. This behaviour allows the application of these materials to convert light directly into heat and to induce localized thermal damage of a diseased tissue.[95–97]

1.6. Multifunctional systems for luminescent thermometry and plasmonic heating

The combination of UCNPs and metal nanostructures leads to additional functionalities for potential application in PTT.[98,99] The imaging capability of multifunctional nanosystems based on UCNPs has been used for guiding the therapy for real-time monitoring of therapeutic responses.[100] A temperature detector in PTT is important for better controlling the NIR irradiation to regulate the heat released to the

surrounding medium, thereby permitting guiding the therapy.[100,101] Recently, the combination of luminescent thermometry and plasmonic heating in single platforms for the real-time monitoring of the heat fluxes has been successfully demonstrated.[71,102] The most recent reports published in the literature tend to shift the plasmon resonance to NIR wavelengths to match the excitation of UC by using more complex gold nanorods.[103–105] The NIR excitation allows the use of a single laser for UC luminescence and photothermal excitation and improve the heating to reach deeper layers of tumor tissue. In addition, Debasu *et al.*[105] demonstrated that the use of gold nanorods instead of spherical nanoparticles allows the use of much lower (by an order of magnitude) laser power excitation densities to achieve the same temperature increase.

Taking into account the state of the art presented in literature, the main goal of this thesis was to design multifunctional platforms based on upconversion nanoparticles for applications in nanomedicine in thermometry and Au nanoparticles-based photothermal therapy.

References

1 PRASAD, P. N. **Introduction to nanomedicine and nanobioengineering**. New Jersey: John Wiley & Sons, 2012.

2 RIEHEMANN, K.; SCHNEIDER, S. W.; LUGER, T. A.; GODIN, B.; FERRARI, M.; FUCHS, H. Nanomedicine—challenge and perspectives. **Angew. Chem. Int. Ed.**, v. 48, p. 872–897, 2009.

3 ZHANG, X.-Q.; XU, X., BERTRAND, N.; PRIDGEN, E.; SWAMI, A.; FAROKHZAD, O. C. Interactions of nanomaterials and biological systems: Implications to personalized nanomedicine. **Adv. Drug. Deliv. Rev.**, v. 64, p. 1363–1384, 2012.

4 SHIN, T.-H.; CHEON, J. Synergism of nanomaterials with physical stimuli for biology and medicine. **Acc. Chem. Res**, v. 50, p. 567–572, 2017.

5 SHI, J.; KANTOFF, P. W.; WOOSTER, R.; FAROKHZAD, O. C. Cancer nanomedicine: Progress, challenges and opportunities. **Nat. Rev. Cancer**, v. 17, p. 20–37, 2017.

6 CHAN, W. C. W. Nanomedicine 2.0. **Acc. Chem. Res.**, v. 50, p. 627–632, 2017.
7 NEL, A. E.; MÄDLER, L.; VELEGOL, D.; XIA, T.; HOEK, E. M.; SOMASUNDARAN, P.; KLAESSIG, F.; CASTRANOVA, V.; THOMPSON, M. Understanding biophysicochemical interactions at the nano-bio interface. **Nat. Mat.**, v. 8, p. 543–557, 2009.

8 CHOI, H. S.; LIU, W.; MISRA, P.; TANAKA, E.; ZIMMER, J. P.; IPE, B. I.; BAWENDI, M. G.; FRANGIONI, J. V. Renal clearance of nanoparticles. **Nat Biotechnol.**, v. 25, p. 1165–1170, 2007.

9 LONGMIRE, M.; CHOYKE, P. L.; KOBAYASHI, H. Clearance properties of nano-sized particles and molecules as imaging agents: Considerations and caveats. **Nanomedicine**, v. 3, p. 703–717, 2008.

10 ALLEN, T. M.; CULLIS, P. R. Drug delivery systems: entering the mainstream. **Science**, v. 303, p. 1818–1822, 2004.

11 DENG, Y.; CAI, Y.; SUN, Z.; LIU, J.; LIU, C.; WEI, J.; LI, W.; LIU, C.; WANG, Y.; ZHAO, D. Multifunctional mesoporous composite microspheres with well-designed nanostructure: a highly integrated catalyst system. **J. Am. Chem. Soc.**, v. 132, p. 8466–8473, 2010.

12 LI, C.; ZHANG, Y.; CHEN, G.; HU, F.; ZHAO, K.; WANG, Q. Engineered multifunctional nanomedicine for simultaneous stereotactic chemotherapy and inhibited osteolysis in an orthotopic model of bone metastasis. **Adv. Mater.**, v. 29, p. 1605754–1605754, 2017.

13 MOHAMMADI, M.; RAMEZANI, M.; ABNOUS, K.; ALIBOLANDI, M. Biocompatible polymersomes-based cancer theranostics: Towards multifunctional nanomedicine. **Int. J. Pharm**., v. 519, p. 287–303, 2017.

14 GAO, J.; GU, H.; XU, B. Multifunctional magnetic nanoparticles: Design, synthesis, and biomedical applications. **Acc. Chem. Res.**, v. 42, p. 1097–1107, 2009.

15 GYAWALI, D.; PALMER, M.; TRAN, R. T.; YANG, J. Progress of nanobiomaterials for theranostic systems. In: TIWARI, A.; RAMALINGAM, M.; HISATOSHI K.; TURNER, A. P. F. **Biomedical materials and diagnostic devices**. Beverly: Scrivener Publishing LLC, 2012. chap. 14, p. 435–476.

16 CINTEZA, L. O. Multifunctional nanosystems for cancer theragnostics. **Biomedical Optics and Medical Imaging. SPIE Newsroom**, v. 10, p. 003432, 2011.

17 ZHOU, F.; HUANG, L. Liposome-mediated cytoplasmic delivery of proteins: An effective means of accessing the MHC class I-restricted antigen presentation pathway. **Immunomethods**, v. 4, p. 229–235, 1994.

18 BALASUBRAMANIAN, V. ONACA, O.; ENEA, R.; HUGHES, D. W.; PALIVAN, C. G. Protein delivery: From conventional drug delivery carriers to polymeric nanoreactors. **Expert Opin. Drug Deliv.**, v. 7, p. 63–78, 2010.

19 WANG, Z.; LIU, G.; ZHENG, H.; CHEN, X. Rigid nanoparticle-based delivery of anti-cancer siRNA: Challenges and opportunities. **Biotechnol. Adv.**, v. 32, p. 831–843, 2014.

20 FADEEL, B.; GARCÍA-BENNETT, A.E. Better safe than sorry: Understanding the toxicological properties of inorganic nanoparticles manufactured for biomedical applications. **Adv. Drug Deliver. Rev.**, v. 62, p. 362–374, 2010.

21 HUANG, X.; LI, L.; LIU, T.; HAO, N.; LIU, H.; CHEN, D.; TANG, F. The shape effect of mesoporous silica nanoparticles on biodistribution, clearance, and biocompatibility in vivo. **ACS Nano**, v. 5, p. 5390–5399, 2011.

22 LLOPIS-LORENTE, A.; LOZANO-TORRES, B.; BERNARDOS, A.; MARTÍNEZ-MÁÑEZ, R.; SANCENÓN, F. Mesoporous silica materials for controlled delivery based on enzymes. **J. Mater. Chem. B**, v. 5, p. 3069–3083, 2017.

23 DE OLIVEIRA, L. F.; BOUCHMELLA, K.; GONÇALVES, K. D. A.; BETTINI, J.; KOBARG, J.; CARDOSO, M. B. Functionalized silica nanoparticles as an alternative platform for targeted drug-delivery of water insoluble drugs. **Langmuir**, v. 32, 3217–3225, 2016.

24 VIVERO-ESCOTO, J. L.; SLOWING, I. I.; TREWYN, B. G.; LIN, V. S. Y. Mesoporous silica nanoparticles for intracellular controlled drug delivery. **Small**, v. 6, p. 1952–1967, 2010.

25 WU, S. H.; MOU, C. Y.; LIN, H. P. Synthesis of mesoporous silica nanoparticles. **Chem. Soc. Rev.**, v. 42, p. 3862–3875, 2013.

26 DE OLIVEIRA FREITAS, L. B. BRAVO, I. J. G.; DE ALMEIDA MACEDO, W. A.; DE SOUSA, E. M. B. Mesoporous silica materials functionalized with folic acid: Preparation, characterization and release profile study with methotrexate. **J. Sol-Gel Sci. Technol**., v. 77, p. 186–204, 2016.

27 ZHANG, Z.; ZHANG, X.; NIU, D.; LI, Y.; SHI, J. Large-pore, silica particles with antibody-like, biorecognition sites for efficient protein separation. **J. Mater. Chem. B**, v. 5, p. 4214–4220, 2017.

28 ZOU, Z.; HE, D.; CAI, L.; HE, X.; WANG, K.; YANG, X.; LI, L.; LI, S.; SU, X. Alizarin complexone functionalized mesoporous silica nanoparticles: A smart system integrating glucose-responsive double-drugs release and real-time monitoring capabilities. **ACS Appl. Mater. Interfaces**, v. 8, p. 8358–8366, 2016.

29 SHEN, D.; YANG, J.; LI, X.; ZHOU, L.; ZHANG, R.; LI, W.; CHEN, L.; WANG, R.; ZHANG, F.; ZHAO, D. Biphase stratification approach to three-dimensional dendritic biodegradable mesoporous silica nanospheres. **Nano Lett.**, v. 14, p. 923–932, 2014.

30 CHENG, W.; NIE, J.; XU, L.; LIANG, C.; PENG, Y.; LIU, G.; WANG, T.; MEI, L.; HUANG, L.; ZENG, X. A pH-sensitive delivery vehicle based on folic acid-conjugated polydopaminemodified mesoporous silica nanoparticles for targeted cancer therapy. **ACS Appl. Mater. Interfaces**, v. 9, p. 18462–18473, 2017.

31 KURCH, S.; SCHLÖDER, J.; BERGES, C.; OSE, R.; SCHUPP, J.; TUETTENBERG, A.; WEISS, H.; SCHULTZE, J.; WINZEN, S.; SCHINNERER, M.; KOYNOV, K.; MEZGER, M.; HAASS, N. K.; TREMEL, W.; JONULEIT, H. Dendritic mesoporous silica nanoparticles for pH-stimuli-responsive drug delivery of TNF-alpha. **Adv Healthc. Mater.**, v. 6, p. 1700012, 2017.

32 CHEN, X. YUAN, P.; LIU, Z.; BAI, Y.; ZHOU, Y. Dual responsive hydrogels based on functionalized mesoporous silica nanoparticles as an injectable platform for tumor therapy and tissue regeneration. **J. Mater. Chem. B**, v. 5, p. 5968–5973, 2017.

33 DONG, J.; ZINK, J. I. Light or heat? The origin of cargo release from nanoimpeller particles containing upconversion nanocrystals under IR irradiation. **Small**, v. 11, p. 4165–4172, 2015.

34 AZNAR, E.; MONDRAGÓN, L.; ROS-LIS, J. V.; SANCENÓN, F.; MARCOS, M. D.; MARTÍNEZ-MÁÑEZ, R.; SOTO, J.; PÉREZ-PAYÁ, E.; AMORÓS, P. Finely tuned temperature-controlled cargo release using paraffin-capped mesoporous silica nanoparticles. **Angew Chem Int Ed Engl.**, v. 50, p. 11172–11175, 2011.

35 MAL, N. K.; FUJIWARA, M.; TANAKA, Y. Photocontrolled reversible release of guest molecules from coumarin-modified mesoporous silica. **Nature**, v. 421, p. 350–353, 2003.

36 CHAI, S.; GUO, Y.; ZHANG, Z.; CHAI, Z.; MA, Y.; QI, L. Cyclodextrin-gated mesoporous silica nanoparticles as drug carriers for red light-induced drug release. **Nanotechnology**, v. 28, p. 145101, 2017.

37 RUIZ-HERNÁNDEZ, E.; BAEZA, A.; VALLET-REGÍ, M. Smart drug delivery through DNA/magnetic nanoparticle gates. **ACS Nano**, v. 5, p. 1259–1266, 2011.

38 ZHANG, J.; YUAN, Z. F.; WANG, Y.; CHEN, W. H.; LUO, G. F.; CHENG, S. X.; ZHUO, R. X.; ZHANG, X. Z. Multifunctional envelope-type mesoporous silica nanoparticles for tumor-triggered targeting drug delivery. **J. Am. Chem. Soc.**, v. 135, p. 5068–5073, 2013.

39 LEE, J.; HAN, S.; LEE, J.; CHOI, M.; KIM, C. Stimuli-responsive α-helical peptide gatekeepers for mesoporous silica nanocarriers. **New J. Chem***,* v. 41, p. 6969–6972, 2017.

40 SONG, Y.; LI, Y.; XU, Q.; LIU, Z. Mesoporous silica nanoparticles for stimuli-responsive controlled drug delivery: Advances, challenges, and outlook. **Int. J. Nanomedicine**, v. 12, p. 87–110, 2017.

41 FERRARI, M. Cancer nanotechnology: Opportunities and challenges, **Nat. Rev. Cancer**, v. 5, p. 161–171, 2005.

42 KUMAR, S.; AARON, J.; SOKOLOV, K. Directional conjugation of antibodies to nanoparticles for synthesis of multiplexed optical contrast agents with both delivery and targeting moieties. **Nat. Protoc.**, v. 3, p. 314–320, 2008

43 AMIN, M.; BADIEE, A.; JAAFARI, M. R. Improvement of pharmacokinetic and antitumor activity of PEGylated liposomal doxorubicin by targeting with N-methylated cyclic RGD peptide in mice bearing C-26 colon carcinomas. **Int. J. Pharm.**,v. 458, p. 324–333, 2013.

44 LU, J.; ZHAO, W.; HUANG, Y.; LIU, H.; MARQUEZ, R.; GIBBS, R. B.; LI, J.; VENKATARAMANAN, R.; XU, L.; LI, S. Targeted delivery of doxorubicin by folic acid-decorated dual functional nanocarrier. **Mol. Pharm.**, v. 11, p. 4164–4178, 2014.

45 OH, S. S.; LEE, B. F.; LEIBFARTH, F. A.; EISENSTEIN, M.; ROBB, M. J.; LYND, N. A.; HAWKER, C. J.; SOH, H. T. Synthetic aptamer-polymer hybrid constructs for programmed drug delivery into specific target cells. **J. Am. Chem. Soc.**, v. 136, p. 15010–15015, 2014.

46 BALE, S. S.; KWON, S. J.; SHAH, D. A.; BANERJEE, A.; DORDICK, J. S.; KANE, R. S. Nanoparticle-mediated cytoplasmic delivery of proteins to target cellular machinery. **ACS Nano**, v. 4, p. 1493–1500, 2010.

47 HAMBLIN, M. R.; DEMIDOVA, T. N. Mechanisms of low level light therapy. In: HAMBLIN, M. R.; WAYNANT, R. W.; ANDERS, J. (Ed.). **Mechanisms of low level light therapy**. Bellingham: SPIE – The International Society for Optical Engineering, 2006. v. 6140, p. 614001/1-614001/12.

48 FRANGIONI, J. V. *In vivo* near-infrared fluorescence imaging. **Current Opinion in Chem. Biol.***,* v. 7, p. 626–634, 2003.

49 SAMEIRO, M.; GONÇALVES, T. Fluorescent labeling of biomolecules with organic probes. **Chem. Rev.**, v. 109, p. 190–212, 2009.

50 BERKOW, J. W.; FLOWER, R. W.; ORTH, D. H.; KELLEY, J. S. **Fluorescein and indocyanine green angiography**: technique and interpretation. 2nd ed. San Francisco: The Foundation of the American Academy of Ophthalmology, 1997.

51 MEDINTZ, I. L.; UYEDA, H. T.; GOLDMAN, E. R.; MATTOUSSI, H. Quantum dot bioconjugates for imaging, labelling and sensing. **Nat. Mater.**, v. 4, p. 435–446, 2005.

52 ZHOU, J.; LIU, Z.; LI, F. Upconversion nanophosphors for small-animal imaging. **Chem. Soc. Rev.**, v. 41, p. 1323–1349, 2012.

53 LIU, Q.; FENG, W.; LI, F. Water-soluble lanthanide upconversion nanophosphors: synthesis and bioimaging applications *in vivo*. **Coord. Chem. Rev.**, v. 273-274, p. 100–110, 2014.

54 TU, D.; ZHENG, W.; LIU, Y.; ZHU, H.; CHEN. X. Luminescent biodetection based on lanthanide-doped inorganic nanoprobes. **Coord. Chem. Rev.**, v. 273-274, p. 13–29, 2014.

55 YUAN, P.; LEE, Y. H.; GNANASAMMANDHAN, M. K.; GUAN, Z.; ZHANG, Y.; XU, Q. H. Plasmon enhanced upconversion luminescence of $NaYF_4$:Yb,Er@SiO_2@Ag core-shell nanocomposites for cell imaging. **Nanoscale**, v. 4, p. 5132–5137, 2012.

56 WANG, X. L.; KREBS, J.; AL-NURI, M. H.; PUDAVAR, E.; GHOSAL, S.; LIEBOW, C.; NAGY, A. A.; SCHALLY, A. V.; PRASAD, P. N. A chemically labeled cytotoxic agent: two-photon fluorophore for optical tracking of cellular pathway in chemotherapy. **Proc. Natl. Acad. Sci. U. S. A**., v. 96, p. 11081–11084, 1999.

57 MOREAUX, L.; SANDRE, O.; CHARPAK, S.; BLANCHARD-DESCE, M.; MERTZ, J. Coherent scattering in multi-harmonic light microscopy. **Biophys. J.**, v. 80, 1568, 2001.

58 PADILHA, L.A. FU, J.; HAGAN, D. J.; VAN STRYLAND, E. W.; CESAR, C. L.; BARBOSA, L. C.; CRUZ, C. H. Two-photon absorption in CdTe quantum dots. **Opt. Express**, v. 13, p. 6460–6467. 2005.

59 AUZEL, F. Upconversion and anti-stokes processes with f and d ions in solids. **Chem. Rev.**, v. 104, p. 139–173, 2004.

60 BETTINELLI, M.; CARLOS, L.; LIU, X. Lanthanide-doped upconversion nanoparticles. **Phys. Today**, v. 68, p. 38–44, 2015.

61 WANG, F.; LIU, X. Recent advances in the chemistry of lanthanide-doped upconversion nanocrystals. **Chem. Soc. Rev.**, v. 38, p. 976–989, 2009.

62 XU, C. T.; ZHAN, Q.; LIU, H.; SOMESFALEAN, G.; QIAN, J.; HE, S.; ANDERSSON-ENGELS, S. Upconverting nanoparticles for pre-clinical diffuse optical imaging, microscopy and sensing: Current trends and future challenges. **Laser and Photonics Rev.**, v. 7, p. 663–697, 2013.

63 ZHAO, J.; JIN, D.; SCHARTNER, E. P.; LU, Y.; LIU, Y.; ZVYAGIN, A. V.; ZHANG, L.; DAWES, J. M.; XI, P.; PIPER, J. A.; GOLDYS, E. M.; MONRO, T. M. Single-nanocrystal sensitivity achieved by enhanced upconversion luminescence. **Nat. Nanotech.**, v. 8, p. 729–734, 2013.

64 DOANE, T. L.; BURDA, C. The unique role of nanoparticles in nanomedicine: imaging, drug delivery and therapy. **Chem. Soc. Rev.**, v. 41, p. 2885–2911, 2012.

65 WANG, H.; HAN, R. L.; YANG, L. M.; SHI, J. H.; LIU, Z. J.; HU, Y.; WANG, Y.; LIU, S. J.; GAN, Y. Design and synthesis of core−shell−shell upconversion nanoparticles for NIR-induced drug release, photodynamic therapy, and cell imaging**. ACS Appl. Mater. Interfaces**, v. 8, p. 4416–4423, 2016.

66 WILHELM, S.; KAISER, M.; WÜRTH, C.; HEILAND, J.; CARRILLO-CARRION, C.; MUHR, V.; WOLFBEIS, O. S.; PARAK, W. J.; RESCH-GENGER, U.; HIRSCH, T. Water dispersible upconverting nanoparticles: effects of surface modification on their luminescence and colloidal stability. **Nanoscale**, v. 7, p. 1403–10, 2015.

67 LI, C.; HOU, Z.; DAI, Y.; YANG, D.; CHENG, Z.; MA, P.; LIN, J. A facile fabrication of upconversion luminescent and mesoporous core–shell structured β-$NaYF_4$:Yb^{3+}, Er^{3+}@mSiO_2 nanocomposite spheres for anti-cancer drug delivery and cell imaging. **Biomater. Sci.**, v. 1, p. 213–223, 2013.

68 ZOHAR, O.; IKEDA, M.; SHINAGAWA, H.; INOUE, H.; NAKAMURA, H.; ELBAUM, D.; ALKON, D. L.; YOSHIOKA, T. Thermal imaging of receptor-activated heat production in single cells. **Biophys. J.**, v. 74, p. 82–89, 1998.

69 HUANG, H.; DELIKANLI, S.; ZENG, H.; FERKEY, D. M.; PRALLE, A. Remote control of ion channels and neurons through magnetic-field heating of nanoparticles. **Nat. Nanotechnol.**, v. 5, p. 602–606, 2010.

70 GOTA, C.; OKABE, K.; FUNATSU, T.; HARADA, Y.; UCHIYAMA, S. Hydrophilic fluorescent nanogel thermometer for intracellular thermometry. **J. Am. Chem. Soc.**, v. 131, p. 2766–2767, 2009.

71 DEBASU, M. L.; ANANIAS, D.; PASTORIZA-SANTOS, I.; LIZ-MARZÁN, L. M.; ROCHA, J.; CARLOS, L. D. All-in-one optical heater-thermometer nanoplatform operative from 300 to 2000 K based on Er^{3+} emission and blackbody radiation. **Adv. Mater.**, v. 25, p. 4868–4874, 2013.

72 BRITES, C. D. S.; LIMA, P. P.; SILVA, N. J. O.; MILLÁN, A.; AMARAL, V. S.; PALACIO, F.; CARLOS, L. D. Thermometry at the nanoscale. **Nanoscale**, v. 4, p. 4799–4829, 2012.

73 BRITES, C. D. S.; LIMA, P. P.; SILVA, N. J. O.; MILLÁN, A.; AMARAL, V. S.; PALACIO, F.; CARLOS, L. D. A luminescent molecular thermometer for long-term absolute temperature measurements at the nanoscale. **Adv. Mater.**, v. 22, p. 4499–4504, 2010.

74 WADE, S. A.; COLLINS, S. F.; BAXTER, G. W. Fluorescence intensity ratio technique for optical fiber point temperature sensing. **J. Appl. Phys.**, v. 94, p. 4743–4756, 2003.

75 ZHANG, F. Upconversion nanoparticles for thermal sensing. In: _____. **Photon Upconversion Nanomaterials.** Berlin: Springer-Verlag, 2015. chap. 10, p. 343–374.

76 BERTHOU, H.; JÖRGENSEN, C. K. Optical-fiber temperature sensor based on upconversion-excited fluorescence. **Opt. Lett.**, v. 15, p. 1100–1102, 1990.

77 MACIEL, G. S.; MENEZES, L. de S.; GOMES, A. S. L.; de ARAÚJO, C. B.; MESSADDEQ, Y.; FLOREZ, A.; AEGERTER, M. A. Temperature sensor based on frequency upconversion in Er^{3+}-doped fluoroindate glass. **IEEE Photon. Technol. Lett.**, v. 7, p. 1474–1476, 1995.

78 MACIEL, G. S.; de ARAÚJO, C. B.; MESSADDEQ, Y.; AEGERTER, M. A. Frequency upconversion in Er^{3+}-doped fluoroindate glasses pumped at 1.48 μm. **Phys. Rev. B**, v. 55, p. 6335–6342, 1997.

79 ALENCAR, M. A. R. C.; MACIEL, G. S.; de ARAÚJO, C. B.; PATRA, A. Er^{3+}-doped $BaTiO_3$ nanocrystals for thermometry: Influence of nanoenvironment on the sensitivity of a fluorescence based temperature sensor. **Appl. Phys. Lett.**, v. 84, p. 4753–4755, 2004.

80 MACIEL, G. S.; ALENCAR, M. A. R. C.; de ARAÚJO, C. B.; PATRA, A. Upconversion emission of $BaTiO_3$:Er^{3+} nanocrystals: influence of temperature and surrounding medium. **J. Nanosci. Nanotechnol.**, v. 10, p. 2143–2148, 2010.

81 VETRONE, F.; NACCACHE, R.; ZAMARRON, A.; SANZ-RODRIGUEZ, F.; MAESTRO, L. M.; RODRIGUEZ, E. M.; JAQUE, D.; SOLE, J. G.; CAPOBIANCO, J. A. Temperature sensing using fluorescent nanothermometers. **ACS Nano**, v. 4, p. 3254–3258, 2010.

82 HEMMER, E.; BENAYAS, A.; LÉGARÉ, F.; VETRONE, F. Exploiting the biological windows: current perspectives on fluorescent bioprobes emitting above 1000 nm. **Nanoscale Horiz.**, v. 1, p. 168–184, 2016.

83 SMITH, A. M.; MANCINI, M. C.; NIE, S. Second window for *in vivo* imaging. **Nat Nanotechnol.**, v. 4, p. 710–711, 2009.

84 JAQUE, D.; RICHARD, C.; VIANA, B.; SOGA, K.; LIU, X.; GARCÍA SOLÉ, J. Inorganic nanoparticles for optical bioimaging. **Adv. Opt. Photonics**, v. 8, p. 1–103, 2016.

85 DIAO, S.; BLACKBURN, J. L.; HONG, G.; ANTARIS, A. L.; CHANG, J.; WU, J. Z.; ZHANG, B.; CHENG, K.; KUO, C. J.; DAI, H. Fluorescence imaging in vivo at wavelengths beyond 1500 nm. **Angew. Chem. Int. Ed.**, v. 54, p. 14758–14762, 2015.

86 SILVA, A. F.; ELAN, F.; FALCÃO-FILHO, E. L.; MAIA, L. J. Q.; de ARAÚJO, C. B. Thermal sensitivity of frequency upconversion in $Al_4B_2O_9$:Yb^{3+}/Nd^{3+} nanoparticles. **J. Mater. Chem. C**, v. 5, p. 1240–1246, 2017.

87 XIMENDES, E. C.; ROCHA, U.; JACINTO, C.; KUMAR, K. U.; BRAVO, D.; LOPEZ, F. J.; RODRIGUEZ, E. M.; GARCIA-SOLE, J.; JAQUE, D. Self-monitored photothermal nanoparticles based on core–shell engineering. **Nanoscale**, v. 8, p. 3057–3066, 2016.

88 JIANG, G.; ZHOU, S.; WEI, X.; CHEN, Y.; DUAN, C.; YIN, M.; YANG, B.; CAO, W. 794 nm excited core–shell upconversion nanoparticles for optical temperature sensing. **RSC Adv.**, v. 6, p. 11795–11801, 2016.

89 CHEN, W.; SHI, C.; TAO, T.; JI, M.; ZHENG, S.; SANG, X.; LIU, X.; QIU, J. Optical temperature sensing with minimized heating effect using core–shell upconversion nanoparticles. **RSC Adv.**, v. 6, p. 21540–21545, 2016.

90 MOURA, A. L.; PINCHEIRA, P. I. R.; MAIA, L. J. Q.; GOMES, A. S. L.; de ARAÚJO, C. B. Two-color random laser based on a Nd^{3+} doped crystalline powder. **J. Lumin.**, v. 181, p. 44–48, 2017.

91 KAMIMURA, M.; MATSUMOTO, T.; SUYARI, S.; UMEZAWA, M.; SOGA, K. Ratiometric near-infrared fluorescence nanothermometry in the OTN-NIR (NIR II/III) biological window based on rare-earth doped β-$NaYF_4$ nanoparticles. **J. Mater. Chem. B**, v. 5, p. 1917–1925, 2017.

92 JAQUE, D.; MARTÍNEZ MAESTRO, L.; ROSAL, B. DEL; HARO-GONZALEZ, P.; BENAYAS, A.; PLAZA, J. L.; MARTÍN RODRÍGUEZ, E.; GARCÍA SOLÉ, J. Nanoparticles for photothermal therapies. **Nanoscale**, v. 6, p. 9494–9530, 2014.

93 EL-SAYED, I. H.; HUANG, X.; EL-SAYED, M. A. Selective laser photo-thermal therapy of epithelial carcinoma using anti-EGFR antibody conjugated gold nanoparticles. **Cancer Letters**, v. 239, p. 129–135, 2006.

94 CHEN, G.; QIU, H.; PRASAD, P. N.; CHEN, X. Upconversion nanoparticles: Design, nanochemistry, and applications in Theranostics. **Chem. Rev.**, v. 114, p. 5161–5214, 2014.

95 HUANG, X.; JAIN, P. K.; EL-SAYED, I. H.; EL-SAYED, M. A. Plasmonic photothermal therapy (PPTT) using gold nanoparticles. **Laser Med. Sci.**, v. 23, p. 217–228, 2008.

96 CHERUKURI, P.; GLAZER, E. S.; CURLEY, S. A. Targeted hyperthermia using metal nanoparticles. **Adv. Drug Delivery Rev.**, v. 62, p. 339–345, 2010.

97 LAL, S.; CLARE, S. E.; HALAS, N. J. Nanoshell-enabled photothermal cancer therapy: impending clinical impact. **Acc. Chem. Res.**, v. 41, p. 1842, 2008.

98 CHENG, L.; YANG, K.; LI, Y.; CHEN, J.; WANG, C.; SHAO,M.; LEE, S.-T.; LIU, Z. Facile preparation of multifunctional upconversion nanoprobes for multimodal imaging and dual-targeted photothermal therapy. **Angew. Chem. Int. Ed.**, v. 50, p. 7385–7390, 2011.

99 CHENG, L.; YANG, K.; LI, Y.; ZENG, X.; SHAO, M.; LEE, S.-T.; LIU, Z. Multifunctional nanoparticles for upconversion luminescence/MR multimodal imaging and magnetically targeted photothermal therapy. **Biomaterials**, v. 33, p. 2215–2222, 2012.

100 DONG, B.; XU, S.; SUN, J.; BI, S.; LI, D.; BAI, X.; WANG, Y.; WANG, L.; SONG. H. Multifunctional $NaYF_4$:Yb^{3+},Er^{3+}@Ag core/shell nanocomposites: integration of upconversion imaging and photothermal therapy. **J. Mater. Chem.**, v. 21, p. 6193–6200, 2011.

101 MAESTRO, L. M.; HARO, P.; IGLESIAS-DE LA CRUZ, M. C.; SANZ-RODRÍGUEZ, F.; JUARRANZ, Á.; SOLÉ, J. G.; JAQUE, D. Fluorescent nanothermometers provide controlled plasmonic-mediated intracellular hyperthermia. **Nanomedicine**, v. 8, p. 379–388, 2013.

102 BRITES, C. D. S.; FUERTES, M. C.; ANGELOMÉ, P. C.; MARTÍNEZ, E. D.; LIMA, P. P.; SOLER-ILLIA, G. J.; CARLOS, L. D. Tethering luminescent thermometry and plasmonics: Light manipulation to assess real-time thermal flow in nanoarchitectures. **Nano Lett.**, v. 17, p. 4746–4752, 2017.

103 HUANG, Y.; ROSEI, F.; VETRONE, F. A single multifunctional nanoplatform based on upconversion luminescence and gold nanorods. **Nanoscale**, v. 7, p. 5178–5185, 2015.

104 ROHANI, S.; QUINTANILLA, M.; TUCCIO, S.; DE ANGELIS, F.; CANTELAR, E.; GOVOROV, A. O.; RAZZARI, L.; VETRONE, F. Enhanced luminescence, collective heating, and nanothermometry in an ensemble system composed of lanthanide-doped upconverting nanoparticles and gold nanorods**. Adv. Opt. Mater.**, v. 3, p. 1606–1613, 2015.

105 DEBASU, M. L.; BRITES, C. D.; BALABHADRA, S.; OLIVEIRA, H.; ROCHA, J.; CARLOS, L. D. Nanoplatforms for plasmon-induced heating and thermometry. **ChemNanoMat**, v. 2, p. 520–527, 2016.

Chapter 2.

Theory and review of literature

2.1. Basic mechanisms of photoluminescence

Luminescence consists of the emission of light by a molecule or ion after absorption of energy. Luminescent substances, called phosphors, can convert energy into electromagnetic radiation in ultraviolet, visible or infrared spectral regions. The emission of light corresponds to a transition from one energy state to another. The excited state is populated by an external excitation source, such as electroluminescence (excitation by an electric voltage), chemiluminescence (by the energy of a chemical reaction), and photoluminescence (by an electromagnetic radiation).[1]

The interaction of light with matter in a photoluminescence process is represented in Figure 2.1 by an energy level scheme. When the phosphor is illuminated, the incident photons can be scattered or absorbed. After absorption of a photon, the active luminescent center in the ground state (A) is promoted to an excited state (A*). The release of energy is given by a radiative pathway (R) and thus the return to the ground state results in luminescence. Alternatively, part of the absorbed energy excites the vibrations of the host lattice, resulting in the release of heat to the medium. This non-radiative pathway (NR) process competes with radiative emission. The efficiency of luminescent species relies on the ratio of the radiative and the nonradiative rates of return to the ground state. In some cases, when the absorption of energy by phosphors is too weak, a sensitizer with higher absorption coefficient is added to the luminescent system. The exciting energy is absorbed by the sensitizer, followed by the energy transfer from the sensitizer to the active luminescent center.[1]

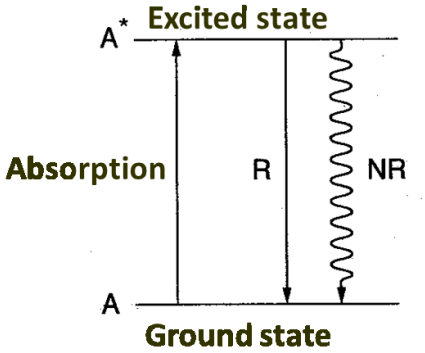

Figure 2.1. Energy level scheme for a simplified representation of luminescence process.

The properties of the emitted photons depend on the properties of the electronic states involved in the emission process. For example, lifetime (the average time between its excitation and return to the ground state) depends on the nature of the excited state. Shorter lifetimes (ns time scale) are observed for excited singlet states in a luminescence process called fluorescence. Phosphorescence, another category of luminescence, originates from triplet excited stated and the resulting emission has a longer time scale (up to hours or even days).[2,3]

2.2. Lanthanide photoluminescence properties

Lanthanide-containing materials possess special luminescence properties allowing high technology applications in diverse fields, such as photonics, medicine, sensing, and imaging as well.[4–6] Lanthanides refer to the fifteen elements with atomic numbers in the range 57–71, from lanthanum to lutetium, with electronic configuration [Xe]$4f^n$. Lanthanide ions essentially exist in their most stable oxidation state as trivalent ions (Ln^{3+}). The electrons are consecutively added to 4f orbitals from La^{3+} configuration ($4f^0$) to Lu^{3+} ($4f^{14}$). The electrons of the partially filled 4f shell are shielded from local environment by the outer $5s^25p^6$ shells. Their photoluminescence properties are related to radiative transitions through the diverse energy levels within $4f^n$ electron configurations and present attractive features including narrow emission peaks, high resistance to photobleaching, tunable photostability, relatively high emission quantum yields, and emission lines spanning the electromagnetic spectrum from the ultraviolet to the infrared region. Considering bioapplications, the spectral discrimination among different Ln^{3+} sharp emissions lines enables multiplexed biological assays. Moreover, long luminescence lifetimes (μs–ms) eliminate the autofluorescence effect, when both analyte and the surroundings emit synchronously (ns), thus improving detection sensitivity.[7,8]

Rare earth elements, comprised of the lanthanides plus scandium and yttrium, are characterized by the high similarity among their physical and chemical properties, and thus the separation of these

elements is extremely difficult.[9] However, Sc^{3+}, Y^{3+}, La^{3+} and Lu^{3+} are not optically active since they do not present unpaired 4f electrons and thus usually used as host materials. The lanthanide ions from Ce^{3+} to Yb^{3+} may be used as luminescent centers in inorganic (*e.g.* UCNP) or molecular (*e.g.* β-diketonate complexes) compounds, or even in organic-inorganic hybrid materials (OIH).[10,11] In OIH materials, a molecular lanthanide complex is incorporated in an inorganic host matrix[12], or an inorganic lanthanide compound is incorporated in an organic polymer matrix[13].

Since the f–f transitions are symmetry forbidden (Laporte rule), the direct excitation of lanthanides at 4f levels is inefficient because of very low molar absorption coefficients, resulting in weak luminescence. Organic ligands with large absorption cross-sections are used for the indirect excitation of Ln^{3+}. Sensitization through a ligand is known as the antenna effect.[14] The coupling with vibrational states changes the geometric arrangement around the metal ion and thus its symmetry.[4]

The luminescence properties of Ln^{3+} ions doped in inorganic nanocrystal hosts or other inorganic materials are influenced by the symmetry around the lanthanides. Lowering the symmetry can lead to relaxation of the selection rule, increasing the probability of transitions, resulting in an enhancement of luminescence emission intensity.[15]

2.3. Upconversion luminescence mechanisms

The photoluminescence in special cases may lead to the emitted photon having a higher energy than the absorbed one. This anti-Stokes emission process may occur by three different mechanisms illustrated in Figure 2.2: simultaneous two-photon absorption (STPA), second-harmonic generation (SHG), and upconversion (UC). In STPA process, two photons are absorbed simultaneously to excite two-photon absorption molecules to the excited states. SHG is a phenomenon in which the emission has half the wavelength of the coherent radiation incident light. Upconversion is the most efficient anti-Stokes process, with no requirement of coherent or high-intensity radiation.[16] In the general principle of upconversion process, the metastable intermediate excited (1) state has a relatively long lifetime that allows the absorption of a second low-energy photon and thus promotion to the higher energy state (3). The radiative decay to the ground state results in a higher-energy photon emission.[17]

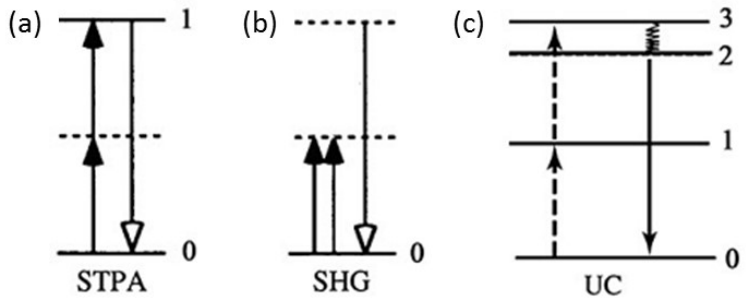

Figure 2.2. Mechanisms to convert low-energy photon pump sources into higher energy output: Simultaneous two-photon absorption (STPA), Second-harmonic generation (SHG), Upconversion (UC). The horizontal dashed (solid) lines indicate virtual (discrete) levels.[16]

The main mechanisms involved in upconversion processes for nanoscale materials are excited-state absorption (ESA) and energy transfer upconversion (ETU), illustrated in Figure 2.3. ESA is a mechanism for singly doped materials, in which occurs the sequential absorption of two photons and the ion is excited to higher state via a real intermediate state. A low concentration of active ion in the doped particles is necessary in ETA to avoid transfer losses through cross-relaxation between luminescent centers. ETU involves a sensitizer (S) ion that is excited to the intermediary states by ground state absorption followed by non-radiative energy transfer to an activator (A) ion. ETU is by far the most efficient upconversion process.[18 19]

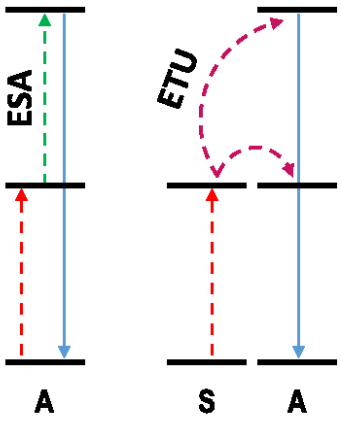

Figure 2.3. Energy transfer mechanisms: excited state absorption (ESA) and energy transfer upconversion (ETU). (S: sensitizer ion, A: activator ion).

These Ln^{3+}-based materials are capable of emitting in the visible following near-infrared excitation. As mentioned in Chapter 1, UCNPs are composed of an inorganic crystalline host matrix in which are co-doped different lanthanide ions: a sensitizer ion (usually Yb^{3+}) and one or two activator ions (the most commons are Er^{3+}, Ho^{3+} and Tm^{3+}). Yb^{3+} has a single energy level at the excited state, which may be easily populated by using a laser operating at 980 nm. A nonradiative energy transfer from Yb^{3+} to the activator ion results in the promotion to its first excited state. This metastable state has a relatively long

lifetime that allows the absorption of a second photon and thus promotion to an even higher excited state. The radiative decay leads to upconversion emission, in which the emitted photon has a higher energy than the individual excitation photons.[20]

2.4. Temperature measurement

Temperature is probably the most important parameter in scientific investigations and technological development. Temperature monitoring is fundamental in industrial processes and in diverse segments, such as electronic devices, automobile systems, as well as health and environment fields. The global market for temperature sensors is influenced mainly by the growing demand from the electronics and automotive industries and is expected to reach $6.13 billion by 2020.[21] Temperature measurement accounts for 75-80% of the worldwide sensor market.[22] The technological demands for microelectronics, photonics and nanomedicine are not satisfied by the conventional thermometers. Such emerging applications require measurements on a submicron scale and without physical contact between the probe and the material to be analyzed.[23]

The miniaturisation of electronics devices has increased the necessity for measuring the temperature in tiny regions of microcircuits to ensure their proper functioning.[24] Yarimaga *et al.*[25] used a thermochromic composite film based on polydiacetylene supramolecules embedded in a host polymer matrix to estimate the temperature distribution in an integrated circuit chip. Polydiacetylene polymers contain alternating double and triple bonds formed from diacetylene monomers. In this methodology, the color of the composite film changes from blue to red in response to the thermal stress caused by heat generation in device components.

Temperature measurement devices comprise a transducer to convert a temperature-dependent phenomenon into a signal. A calibration curve is constructed to obtain the equation of signal as a function of temperature.[26] Thermometry techniques at the nanoscale may be classified into three main groups according to the physical nature of the phenomenon used to measure temperature: electrical, mechanical and optical. Electrical and mechanical approaches are based on a thermocouple or thermistor positioned at the tip of an atomic force microscope with a diameter of the order of 20 to 100 nm. These scanning thermal techniques are able to map the temperature of a sample surface with a spatial resolution higher than 100 nm.[27,28] Limitations encountered when working at the submicron scale include the requirement of physical contact between the thermal probe and the specimen, resulting in invasive bioprobes and hindering the measurement of fast-moving objects.[29–31]

A solution is the use of noncontact techniques, performed by optical thermometers. A wide variety of techniques are based on variations of optical properties induced by changes in temperature,[32] such as:

(i) Raman scattering thermometry, which exploits the inelastic scattering of light from an irradiated sample and the exchange of energy with lattice vibrations;[33]

(ii) thermoreflectance, a technique based on the refractive index of a material, in which temperature changes induce variations in reflection of light at an interface;[34]

(iii) techniques based on the spectral analysis of light emitted by luminescent nanometric probes in the visible and NIR range, in which temperature variations induce different effects such as changes in fluorescence intensity, decay lifetime, wavelength and excitation spectral profile.[35,36]

(iv) infrared thermal imaging, which works by measuring the thermal radiation emitted by a body using an infrared sensitive camera (Planck's blackbody law).[37]

The most popular optical method is infrared thermal imaging for night vision. This technique also finds applications in medicine. Physiological changes in tissue are indicated by an increase in temperature because of higher metabolic activity, which precedes pathological states, such as a malignant tumor, fibrosis, infection or inflammation. The temperature of tumor tissue is about 2.5 °C higher than unaffected tissue in the vicinity. Thermography presents potential for early detection of breast cancer, but limitations are related to the low resolution of thermal pictures and the difficulty to detect deep tumors.[38–40]

2.5. Luminescence thermometry

Among different optical methods, luminescence thermometry is more practical to obtain high-resolution measurements because of the use of nanometric probes. Luminescent techniques are based on several kinds of nanoprobes including rare earth-doped nanoparticles, quantum dots, carbon dots and organic dyes. Luminescent nanothermometers offer remote response with high detection sensitivity (> 1%·K^{-1}) and spatial resolution (< 10 μm) in short acquisition times (<1 ms). In addition, they work even in biological fluids, strong electromagnetic fields and fast-moving objects.[23]

Temperature variations may induce different effects on luminescence, including:

(i) Decrease of emission intensity based on the increase of nonradiative relaxation rates with temperature. In this case, the thermal sensing principle is the analysis of the luminescence intensity. This method is susceptible to errors related to variations in probe concentration, excitation power or detection efficiency;[41]

(ii) Decrease of excited state lifetime because of thermal activation of multiphonon-assisted electron recombination. The fluorescent lifetime method requires more complex equipment. However, fluorescence lifetime thermometry offers advantages over intensity-based methods such as independence *vs*. phosphor concentration variations or fluctuations of excitation intensity;[42,43]

(iii) Shifting of the peak of the spectrum to lower energies because of thermal expansion of the lattice. This a relevant effect in semiconductor QDs for which the bang-gap energy is reduced with increase in temperature;[44]

(iv) Bandwidth broadening mainly due to intrinsic vibrations of the lattice phonons;[45]

(v) Decrease of the degree of polarization (anisotropy) of the fluorescence as temperature increase. Temperature sensing is performed by monitoring the fluorescence polarization anisotropy;[46]

(vi) Band shape variations because of electronic state populations redistribution following Boltzmann statistics. Subsequent variations in the relative intensity between different spectral lines that make up a luminescence spectrum are observed. The electronic states from which emissions lines are generated are very close in energy such that they are thermally coupled. This ratiometric method is the most widely used and more reliable one because of its self-referencing feature which eliminates variations due to probe concentration, inhomogeneities and fluctuations of the excitation source and detectors.[41]

Organic dyes, such as rhodamine, fluorescein, isothiocyanates, are an example of intensity-based luminescence thermometry, for which the temperature increase favors the nonradiative relaxation of the excited states caused by increase of frequency and energy of molecules collisions in solution, as well as the amplitude of internal molecular vibrations, and thus the quenching of emission.[47] Paviolo *et al.*[48] employed an organic dye, Rhodamine B, as a temperature sensor in the temperature range from 21 to 80 °C under visible excitation at 514 nm. In this study, two techniques were compared: fluorescence intensity- and lifetime-based techniques. Intensity values decrease more steeply than lifetime, giving this technique higher detection sensitivity. The use of organic dyes presents some drawbacks due to their hydrophobicity, which limits their administration in physiological environment, and the decrease in emission intensity with time caused by photobleaching and photoblinking effects. Photobleaching is the main limitation to the use of organic dyes to follow temperature changes that require continuous long-term temperature measurements.[49]

Red-shift and fluorescence quenching with temperature increase are known effects in QD thermometry.[50] Walker *et al.*[51] demonstrated the strongly temperature-dependent steady-state photoluminescence of CdSe QDs with a ZnS overlayer. The emission was measured under excitation at 480 nm in the temperature range from -173 to 42 °C. The luminescence intensity was observed to decrease as the temperature increased and the peak position was red-shifted. Yang *et al*.[52] observed the red-shift as well for the emission spectrum of CdSe nanocrystals. Such effect is explained by the fact that the lattice becomes dilated at elevated temperatures, which in turn alters the electron-lattice interaction. Haro-González *et al.*[44] have demonstrated that the fluorescence time decay is strongly dependent on the dot's size and temperature. QDs offer several advantages over dyes, such as absorption and emission band positions tunable by particle size and more symmetric and narrower emission bands.[53] Nevertheless, several drawbacks preclude their use in bioapplications, particularly blinking under continuous illumination, poor stability in aqueous solutions, inhomogeneous luminescence and the release of toxic heavy metal ions such as Cd.[54]

Carbon nanoparticles (< 10 nm in diameter) are emerging luminescent materials with intense and tunable emission. Stability in aqueous solutions and absence of toxic elements (*e.g.* Cd) render them potential candidates to replace QDs. However, the relationship among synthesis routes, structure and properties still not well understood and limits their application.[55] Kalytchuk *et al*.[56] developed a carbon dot-

based nanothermometer exploiting the temperature dependence (between 15–45 °C) of visible luminescence lifetime under UV excitation. The nanoprobes presented a maximum sensitivity of 1.79% K^{-1} with a statistical accuracy of 0.27 °C, and the capacity for *in vitro* sensing in HeLa cells was demonstrated.

Green fluorescent proteins (GFP), widely used as contrast agent in biology, can also be used as a biocompatible fluorescent thermometer. Donner *et al*.[57] reported the strong temperature dependence of polarization state of the GFP luminescence in the physiological range (20–60 °C). The hyperthermia effect induced by gold nanorods around in HeLa and U-87 MG cancer cells was monitored with a spatial resolution of 300 nm and a temperature accuracy of about 0.4 °C.

The development of luminescent nanothermometers for temperature sensing and mapping is a tool for studying biochemical processes that take place inside the cell (such as gene expression, metabolism, or cell division) with the capacity to change the intracellular temperature.[58–60] Gota *et al*.[61] demonstrated for the first time an intracellular thermometer with an organic dye as the temperature probe, which could determine intracellular temperatures within 0.5 °C. Vetrone *et al*.[62] has first demonstrated Ln^{3+} doped fluorescent nanomaterials ($NaYF_4$:Er^{3+}:Yb^{3+}) capable of accurately determining the temperature with high sensitivity and stability in HeLa cancer cells from 25 °C to their thermally induced death at 45 °C. Suzuki *et al*.[60] developed single-cell microscopic thermometry methods using glass capillaries filled with a Eu(III) complex. The thermal dependence of Eu^{3+} luminescence was used to detect the real-time thermogenesis induced by ionomycin, a chemical species that raises the intracellular level of Ca^{2+} influx from the extracellular space.[63] Itoh *et al*.[64] demonstrated subcellular-level quantitative imaging of Ca^{2+}-induced heat production in myotubes. The organelle thermometry, using the fluorescent protein mCherry and an endoplasmic reticulum-targeting molecule, was performed by means of fluorescence lifetime imaging microscopy. The first use of a photoluminescent thermometer for *in vivo* sensing was reported by Chen *et al*.[65] by using a dual-emissive phosphorescent polymeric thermometer *via* ratiometric imaging and time-resolved luminescence imaging. The water-soluble thermometer displayed good stability and biocompatibility.

2.6. Gold nanoparticles for bioapplications

Metal nanostructures are good candidates to be used as heaters in PTT. The light-matter interaction in metal nanostructures relies on the collective oscillation of the free electrons confined within a given dimension, constituting the localized SPR. Surface plasmon excitation is followed by a nonradiative relaxation and a subsequent energy transfer to the lattice in the form of heat. Silver offers advantages over gold, such as higher extinction coefficients and extremely high field enhancements. However, Ag nanoparticles present lower chemical stability and it is toxic. Therefore, gold is more appropriate for biological applications due to it is inertness and biocompatibility.[66,67]

Figure 2.4 presents the extinction spectra of aqueous solutions containing dispersed gold nanoparticles in different shapes: spheres, rods and shells. The shape and size of metallic nanostructures contribute to the extinction bands, which are due to localized surface plasmon resonance. For gold spheres, the extinction peak shifts to the red as NP size is increased. Plasmon resonance may be shifted from the visible to the biological transparency window in the NIR region of the spectrum by using more complex geometries**,** such as rods, shells and cages.[68]

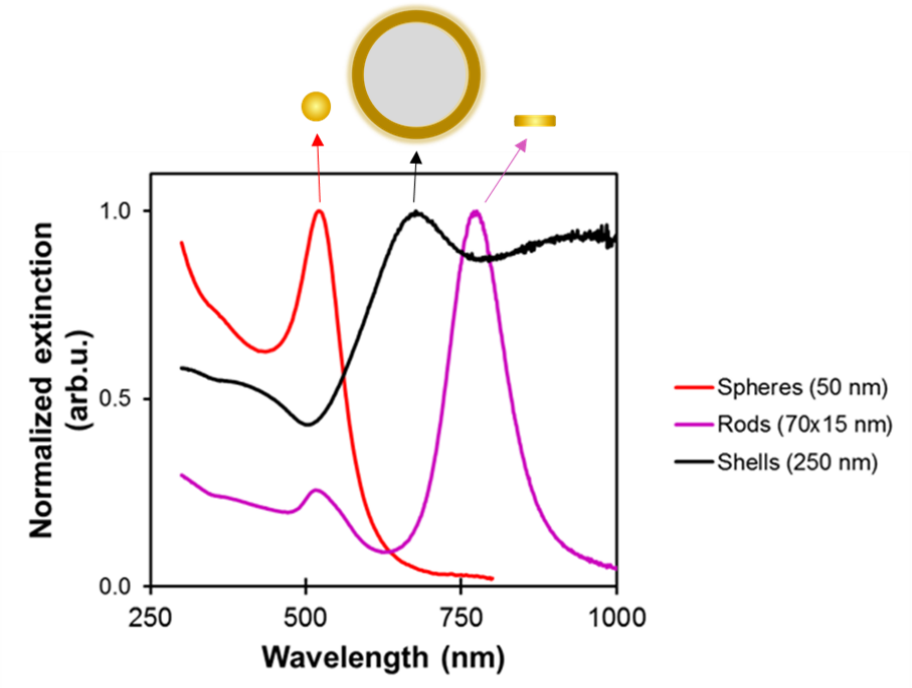

Figure 2.4. Extinction spectra of aqueous solutions of gold nanoparticles in different shapes: spheres, rods and shells.

In addition to the well-known application as an agent in PTT, Au nanoparticle-based systems offer a wide variety of possibilities for biomedical applications. The wavelength and intensity of the SPR band are highly sensitive to the nature of the local environment around the nanoparticles, leading to the development of biosensors based on the shift of the SPR band. Two mechanisms are involved in the SPR shift: (i) nanostructure aggregation and (ii) biomolecule-surface interactions.[69,70] Furthermore, the photothermal behaviour allows for the controlled delivery of molecules.[71–74] Functionalization of Au nanoparticle surface is typically performed through an Au-thiol bond. The application of these Au-based materials for light-induced release comprises two main strategies. First, by directly attaching molecules to be delivered onto the nanoparticle surface, a femtosecond laser pulse wag then reshapes the nanoparticles and break the Au-S bond. It should be noted that toxic effects are related to the formation of small particles caused by high energy of excitation laser.[75] Second, by attaching a host molecule onto the nanoparticle surface, the cargo molecule may be complexed to the host molecule through weaker, noncovalent interactions, allowing the use of relatively low laser power at the SPR wavelength for release

by reducing the attraction between host and cargo species.[76] The laser power density is an important factor to control the thermal release in order to generate mild hyperthermia in a temperature range (40−43 °C) that is sufficient for drug release with minimal damage to healthy tissue.[77]

Gold or silver nanoparticles may be combined with UCNPs to enhance the upconversion efficiency through the SPR effect. The water dispersion of UCNPs results in the contact of the particles' surface with efficient quenchers groups, such as OH, polyethylene glycols (PEG) or surfactants.[78] The strategy to enhance the upconversion luminescence is to place UCNPs in the proximity of a metallic nanostructure. The collective oscillations of the metal electrons induced by a local electromagnetic field can lead to greatly enhanced excitation and emission rates of neighboring luminophores. The enhancement of emission efficiency in UCNPs may be attributed to the coupling of the upconversion emission with the surface plasmon resonance.[79,80,81] Silver is known to be very efficient at promoting metal-enhanced fluorescence, though it is harmful for biological applications. Zhang *et al.*[82] have shown that growing gold nanoparticles on the surface of $NaYF_4$:Yb^{3+}:Tm^{3+} nanocrystals can more than double their upconversion intensity, while the growth of a continuous shell was found to quench the emission due to scattering of incident excitation radiation.

References

1 BLASSE, G.; GRABMAIER, B. C. A general introduction to luminescent materials. In: _____. **Luminescent Materials.** Heidelberg: Springer, 1994. chap. 1, p. 1–19.

2 SHINDE, K.N.; DHOBLE, S.J.; SWART, H.C.; PARK, K. Basic mechanisms of photoluminescence. In: _____. **Phosphate phosphors for solid-state lighting**. Heidelberg: Springer, 2012. v. 174, chap. 2, p. 41–59. (Springer series in materials science).

3 LAKOWICZ, J. R. Introduction to fluorescence. In: **Principles of fluorescence spectroscopy**. 3rd. ed. New York: Springer, 2006. chap. 1, p. 1–26.

4 BÜNZLI, J. C. G.; PIGUET, C. Taking advantage of luminescent lanthanide ions. **Chem. Soc. Rev.**, v. 34, p. 1048–1077, 2005.

5 BÜNZLI, J. C. G.; ELISEEVA, S. V. Intriguing aspects of lanthanide luminescence. **Chem. Sci.**, v. 4, p. 1939–1949, 2013.

6 CARLOS, L. D.; FERREIRA, R. A.; BERMUDEZ, V. D. Z.; RIBEIRO, S. J. Lanthanide-containing light-emitting organic–inorganic hybrids: A bet on the future. **Adv. Mater.**, v. 21, p. 509–534, 2009.

7 MUKHERJEE, P.; SHADE, C. M.; YINGLING, A. M.; LAMONT, D. N.; WALDECK, D. H.; PETOUD, S. Lanthanide sensitization in II–VI semiconductor materials: A case study with terbium (III) and europium (III) in zinc sulfide nanoparticles. **J. Phys. Chem. A.**, v. 115, p. 4031–4041, 2011.

8 LIU, Y.; TU, D.; ZHU, H.; MA, E.; CHEN, X. Lanthanide-doped luminescent nano-bioprobes: From fundamentals to biodetection. **Nanoscale**, v. 5, p. 1369–1384, 2013.

9 BINNEMANS, K.; JONES, P. T.; BLANPAIN, B.; VAN GERVEN, T.; YANG, Y.; WALTON, A.; BUCHERT, M. Recycling of rare earths: A critical review. **J. Clean. Prod.**, v. 51, p. 1–22, 2013.

10 RIBEIRO, S. J. L.; DOS SANTOS, M. V.; SILVA, R. R.; PECORARO, E.; GONÇALVES, R. R.; CAIUT, J. M. A. Optical properties of luminescent materials. In: LEVY, D., ZAYAT, M. (Eds.). **The sol-gel handobook, synthesis, characterization and applications**. Weinheim: Wiley-VCH Verlag GmbH & Co. KGaA, 2015. v. 2, p. 929–962.

11 BINNEMANS, K. Lanthanide-based luminescent hybrid materials. **Chem. Rev.**, v. 109, p. 4283-4374, 2009.

12 NIGOGHOSSIAN, K.; MESSADDEQ, Y.; BOUDREAU, D.; RIBEIRO, S. J. L. UV and temperature-sensing based on $NaGdF_4$:Yb^{3+}:Er^{3+}@SiO_2–$Eu(tta)_3$. **ACS Omega**, v. 2, p. 2065–2071, 2017.

13 NIGOGHOSSIAN, K.; PERES, M. F. S.; PRIMO, F. L.; TEDESCO, A.C.; PECORARO, E.; MESSADDEQ, Y.; RIBEIRO, S. J. L. Infrared to visible up-conversion in biocellulose-yttrium vanadate nanoparticles composite membranes. Demonstration of chloroaluminum phthalocyanine light emission under up-converted light excitation. **Colloid and Interface Science Communications**, v. 2, p. 6-10, 2014.

14 WEISSMAN, S. I. Intramolecular energy transfer the fluorescence of complexes of europium. **J. Chem. Phys.**, v. 10, p. 214–217, 1942.

15 HAN, S.; DENG, R.; XIE, X.; LIU, X. Enhancing luminescence in lanthanide-doped upconversion nanoparticles. **Angew. Chem. Int. Ed.**, v. 53, p. 11702–11715, 2014.

16 GAMELIN, D. R.; GÜDEL, H. U. Design of luminescent inorganic materials: New photophysical processes studied by optical spectroscopy. **Acc. Chem. Res.**, v. 33, p. 235–242, 2000.

17 ZHOU, J.; LIU, Q.; FENG, W.; SUN, Y.; LI, F. Upconversion luminescent materials: Advances and applications. **Chem. Rev.**, v. 115, p. 395–465, 2015.

18 ZHOU, J.; XU, S.; ZHANG, J.; QIU, J. Upconversion luminescence behavior of single nanoparticles. **Nanoscale**, v. 7, p. 15026–15036, 2015.

19 VENNERBERG, D.; LIN, Z. Upconversion nanocrystals: Synthesis, properties, assembly and applications. **Sci. Adv. Mater.**, v. 3, p. 26–40, 2011.

20 AUZEL, F. Upconversion and anti-stokes processes with f and d ions in solids. **Chem. Rev.**, v. 104, p. 139–173, 2004.

21 GRAND VIEW RESEARCH, INC. **Temperature sensors market analysis by application (automotive, consumer electronics, environmental, medical, process industries) and segment forecasts to 2020.** Report Code: 978-1-68038-495-6. San Francisco, 2015**.** 28 p.

22 CHILDS, P. R. N.; GREENWOOD, J. R.; LONG, C. A. Review of temperature measurement. **Rev. Sci. Instrum.**, v. 71, p. 2959–2978, 2000.

23 BRITES, C. D. S.; LIMA, P. P.; SILVA, N. J. O.; MILLÁN, A.; AMARAL, V. S.; PALACIO, F.; CARLOS, L. D. A luminescent molecular thermometer for long-term absolute temperature measurements at the nanoscale. **Adv. Mater.**, v. 22, p. 4499–4504, 2010.

24 MECKLENBURG, M.; HUBBARD, W. A.; WHITE, E. R.; DHALL, R.; CRONIN, S. B.; ALONI, S.; REGAN, B. C. Nanoscale temperature mapping in operating microelectronic devices. **Science**, v. 347, p. 629–632, 2015.

25 YARIMAGA, O.; LEE, S.; HAM, D. Y.; CHOI, J. M.; KWON, S. G.; IM, M., KIM, S.; KIM, J. M.; CHOI, Y. K. Thermofluorescent conjugated polymer sensors for nano- and microscale temperature monitoring. **Macromol. Chem. Phys.**, v. 212, p. 1211–1220, 2011.

26 CHILDS, P. R. N. Nanoscale thermometry and temperature measurement. In: CARLOS, L. D.; PALACIO, F. **Thermometry at the nanoscale: Techniques and selected applications.** The Royal Society of Chemistry, chap. 1, p. 3–22, 2016.

27 MAJUMDAR, A.; LAI, J.; CHANDRACHOOD, M.; NAKABEPPU, O.; WU, Y.; SHI, Z. Thermal imaging by atomic force microscopy using thermocouple cantilever probes. **Rev. Sci. Instrum.**, v. 66, p. 3584–3592, 1995.

28 SHI, L.; KWON, O.; MINER, A. C.; MAJUMDAR, A. Design and batch fabrication of probes for sub-100 nm scanning thermal microscopy. **J. Microelectromech. Syst.**, v. 10, p. 370–378, 2001.

29 KIM, K.; CHUNG, J.; WON, J.; KWON, O.; LEE, J. S.; PARK, S. H.; CHOI, Y. K. Quantitative scanning thermal microscopy using double scan technique. **Appl. Phys. Lett.**, v. 93, p. 203115, 2008.

30 MENGES, F.; MENSCH, P.; SCHMID, H.; RIEL, H.; STEMMER, A.; GOTSMANN, B. Temperature mapping of operating nanoscale devices by scanning probe thermometry. **Nat. Commun.**, v. 7, p. 10874, 2016.

31 YUE, Y.; WANG, X. Nanoscale thermal probing. **Nano Rev.**, v. 3, p. 11586, 2012.

32 CHRISTOFFERSON, J.; MAIZE, K.; EZZAHRI, Y.; SHABANI, J.; WANG, X.; SHAKOURI, A. Microscale and nanoscale thermal characterization techniques. **J. Electron. Packag.**, v. 130, p. 041101, 2008.

33 MAGNOTTI, G.; BARLOW, R. S. Dual-resolution Raman spectroscopy for measurements of temperature and twelve species in hydrocarbon–air flames. **Proc. Combust. Inst.**, v. 36, p. 4477–4485, 2017.

34 FERNANDES, D.; WINTER, R.; DA SILVA, J. C.; KAMIKAWACHI, R. C.; MACEDO, A. G. Influence of temperature on the refractive index sensitivities of fiber Bragg gratings refractometers. **J. Microw. Optoelectron. Electromagn. Appl.**, v. 16, p. 385–392, 2017.

35 JAQUE, D.; VETRONE, F. Luminescence nanothermometry. **Nanoscale**, v. 4, p. 4301–4326, 2012.

36 WANG, S.; WESTCOTT, S.; CHEN, W. Nanoparticle luminescence thermometry. **J. Phys. Chem. B**, v. 106, p. 11203–11209, 2002.

37 DEBASU, M. L.; ANANIAS, D.; PASTORIZA-SANTOS, I.; LIZ-MARZÁN, L. M.; ROCHA, J.; CARLOS, L. D. All-in-one optical heater-thermometer nanoplatform operative from 300 to 2000 K based on Er^{3+} emission and blackbody radiation. **Adv. Mater.**, v. 25, p. 4868–4874, 2013.

38 ETEHADTAVAKOL, M.; NG, E.Y.K. An overview of medical infrared imaging in breast abnormalities detection. In: _____. **Application of infrared to biomedical sciences.** Singapore: Springer, 2017. p. 45–57.

39 KANDLIKAR, S. G.; PEREZ-RAYA, I.; RAGHUPATHI, P. A.; GONZALEZ-HERNANDEZ, J. L.; DABYDEEN, D.; MEDEIROS, L.; PHATAK, P. Infrared imaging technology for breast cancer detection – Current status, protocols and new directions. **Int. J. Heat Mass Transf.**, v. 108, p. 2303–2320, 2017.

40 KENNEDY, D. A.; LEE, T.; SEELY, D. A comparative review of thermography as a breast cancer screening technique. **Integr. Cancer Ther.**, v. 8, p. 9–16, 2009.

41 BRITES, C. D. S.; LIMA, P. P.; SILVA, N. J. O.; MILLÁN, A.; AMARAL, V. S.; PALACIO, F.; CARLOS, L. D. Lanthanide-based luminescent molecular thermometers. **New J. Chem.**, v. 35, p. 1177–1183, 2011.

42 DAS, S.; SOM, S.; YANG, C. Y.; CHAVHAN, S.; LU, C. H. Structural evaluations and temperature dependent photoluminescence characterizations of Eu^{3+}-activated $SrZrO_3$ hollow spheres for luminescence thermometry applications. **Scientific reports**, v. 6, p. 25787, 2016.

43 CHAMBERS, M.D.; CLARKE, D.R. Doped oxides for high-temperature luminescence and lifetime thermometry. **Annu. Rev. Mater. Res.**, v. 39, p. 325–359, 2009.

44 HARO-GONZÁLEZ, P.; MARTÍNEZ-MAESTRO, L.; MARTÍN, I. R.; GARCÍA-SOLÉ, J.; JAQUE, D. High-sensitivity fluorescence lifetime thermal sensing based on CdTe quantum dots. **Small**, v. 8, p. 2652–2658, 2012.

45 WANG, X.; ZHENG, J.; XUAN, Y.; YAN, X. Optical temperature sensing of $NaYbF_4$:Tm^{3+} @SiO_2 core-shell micro-particles induced by infrared excitation. **Opt. Express**, v. 21, p. 21596–21606, 2013.

46 DONNER, J. S.; THOMPSON, S. A.; KREUZER, M. P.; BAFFOU, G.; QUIDANT, R. Mapping intracellular temperature using green fluorescent protein. **Nano Lett.**, v. 12, p. 2107–2111, 2012.

47 KUZKOVA, N.; POPENKO, O.; YAKUNOV, A. Application of temperature-dependent fluorescent dyes to the measurement of millimeter wave absorption in water applied to biomedical experiments. **Int J. Biomed Imaging.**, v. 2014, p. 243564, 2014.

48 PAVIOLO, C.; CLAYTON, A. H. A.; MCARTHUR, S. L.; STODDART, P. R. Temperature measurement in the microscopic regime: A comparison between fluorescence lifetime-and intensity-based methods. **J. Microsc.**, v. 250, p. 179–188, 2013.

49 LEE, J.; KOTOV, N. A. Thermometer design at the nanoscale. **Nano Today**, v. 2, p. 48–51, 2007.

50 MAESTRO, L. M.; JACINTO, C.; SILVA, U. R.; VETRONE, F.; CAPOBIANCO, J. A.; JAQUE, D.; SOLÉ, J. G. CdTe quantum dots as nanothermometers: Towards highly sensitive thermal imaging. **Small**, v. 7, p. 1774–1778, 2011.

51 WALKER, G.; SUNDAR, V.; RUDZINSKI, C.; WUN, A.; BAWENDI, M.; NOCERA, D. Quantum-dot optical temperature probes. **Appl. Phys. Lett.**, v. 83, p. 3555–3557, 2003.

52 YANG, J. M.; YANG, H.; LIN, L. Quantum Dot Nano Thermometers Reveal Heterogeneous Local Thermogenesis in Living Cells. **ACS Nano**, v. 5, p. 5067–5071, 2011.

53 RESCH-GENGER, U.; GRABOLLE, M.; CAVALIERE-JARICOT, S.; NITSCHKE, R.; NANN, T. Quantum dots versus organic dyes as fluorescent labels. **Nat. Methods**, v. 5, p. 763−775, 2008.

54 BRITES, C. D. S.; LIMA, P. P.; SILVA, N. J. O.; MILLÁN, A.; AMARAL, V. S.; PALACIO, F.; CARLOS, L. D. Thermometry at the nanoscale. **Nanoscale**, v. 4, p. 4799–4829, 2012.

55 GORYACHEVA, I. Y.; SAPELKIN, A. V.; SUKHORUKOV, G. B. Carbon nanodots: Mechanisms of photoluminescence and principles of application. **Trends Analyt. Chem.**, v. 90, p. 27−37, 2017.

56 KALYTCHUK, S.; POLÁKOVÁ, K.; WANG, Y.; FRONING, J. P.; CEPE, K.; ROGACH, A. L.; ZBORIL, R. Carbon dot nanothermometry: Intracellular photoluminescence lifetime thermal sensing. **ACS Nano**, v. 11, p. 1432−1442, 2017.

57 ZIMMER, M. GFP: from jellyfish to the Nobel prize and beyond. **Chem. Soc. Rev.**, v. 38, p. 2823−2832, 2009.

58 OKABE, K.; INADA, N.; GOTA, C.; HARADA, Y.; FUNATSU, T.; UCHIYAMA, S. Intracellular temperature mapping with a fluorescent polymeric thermometer and fluorescence lifetime imaging microscopy. **Nat. Commun.**, v. 3, p. 705, 2012.

59 MONTI, M.; BRANDT, L.; IKOMI-KUMM, J.; OLSSON, H. Microcalorimetric investigation of cell metabolism in tumour cells from patients with non-Hodgkin lymphoma (NHL). **Scand. J. Haematol.**, v. 36, p. 353–357, 1986.

60 SUZUKI, M.; TSEEB, V.; OYAMA, K.; ISHIWATA, S. Microscopic detection of thermogenesis in a single HeLa cell. **Biophys. J.**, v. 92, p. L46–L48, 2007.

61 GOTA, C.; OKABE, K.; FUNATSU, T.; HARADA, Y.; UCHIYAMA, S. Hydrophilic fluorescent nanogel thermometer for intracellular thermometry. **J. Am. Chem. Soc.**, v. 131, p. 2766–2767, 2009.

62 VETRONE, F.; NACCACHE, R.; ZAMARRÓN, A.; DE LA FUENTE, A. J.; SANZ-RODRÍGUEZ, F.; MAESTRO, L. M.; RODRIGUEZ, E. M.; JAQUE, D.; SOLÉ, J. G.; CAPOBIANCO, J. A. Temperature sensing using fluorescent nanothermometers. **ACS Nano**, v. 4, p. 3254–3258, 2010.

63 STEGE, G. J. J.; WIERENGA, P. K.; KAMPINGA, H. H.; KONINGS, A. W. T. Hyperthermia, Intracellular free calcium and calcium ionophores. **Int. J. Radiat. Biol.**, v. 64, p. 459–468, 1993.

64 ITOH, H.; ARAI, S.; SUDHAHARAN, T.; LEE, S. C.; CHANG, Y. T.; ISHIWATA, S. I.; SUZUKI, M.; LANE, E. B. Direct organelle thermometry with fluorescence lifetime imaging microscopy in single myotubes. **Chem. Commun.**, v. 52, p. 4458–4461, 2016.

65 CHEN, Z.; ZHANG, K. Y.; TONG, X.; LIU, Y.; HU, C.; LIU, S.; YU, Q.; ZHAO, Q.; HUANG, W. Phosphorescent polymeric thermometers for *in vitro* and *in vivo* temperature sensing with minimized background interference. **Adv. Funct. Mater.**, v. 26, p. 4386–4396, 2016.

66 QIU, Y.; LIU, Y.; WANG, L.; XU, L.; BAI, R.; JI, Y.; WU, X.; ZHAO, Y.; LI, Y.; CHEN, C. Surface chemistry and aspect ratio mediated cellular uptake of Au nanorods. **Biomaterials**, v. 31, p. 7606–7619, 2010.

67 ALKILANY, A. M.; MURPHY, C. J. Toxicity and cellular uptake of gold nanoparticles: What we have learned so far? **Nanopar. Res.**, v. 12, p. 2313–2333, 2010.

68 LINK, S.; EL-SAYED, M. A. Shape and size dependence of radiative, non-radiative and photothermal properties of gold nanocrystals. **Int. Rev. Phys. Chem.**, v. 19, p. 409–453, 2000.

69 TAURAN, Y.; BRIOUDE, A.; COLEMAN, A. W.; RHIMI, M.; KIM, B. Molecular recognition by gold, silver and copper nanoparticle. **World J. Biol. Chem.**, v. 4, p. 35–63, 2013.

70 PETRYAYEVA, E.; KRULL, U. J. Localized surface plasmon resonance: Nanostructures, bioassays and biosensing—A review. **Anal. Chim. Acta**, v. 706, p. 8–24, 2011.

71 HUSCHKA, R; ZULOAGA, J.; KNIGHT, M. W.; BROWN, L. V.; NORDLANDER, P.; HALAS, N. J. Light-induced release of DNA from gold nanoparticles: Nanoshells and nanorods. **J. Am. Chem. Soc.**, 133, p. 12247–12255, 2011.

72 OU, Y. C.; WEBB, J. A.; FALEY, S.; SHAE, D.; TALBERT, E. M.; LIN, S.; CUTRIGHT, C. C.; WILSON, J. T.; BELLAN, L. M.; BARDHAN, R. Gold nanoantenna-mediated photothermal drug delivery from thermosensitive liposomes in breast cancer. **ACS omega**, v. 1, p. 234–243, 2016.

73 YAMASHITA, S. FUKUSHIMA, H.; NIIDOME, Y.; MORI, T.; KATAYAMA, Y.; NIIDOME, T. Controlled-release system mediated by a retro Diels–Alder reaction induced by the photothermal effect of gold nanorods. **Langmuir**, v. 27, p. 14621–14626, 2011.

74 SHEN, S.; TANG, H.; ZHANG, X.; REN, J.; PANG, Z.; WANG, D.; GAO, H.; QIAN, Y.; JIANG, X.; YANG, W. Targeting mesoporous silica-encapsulated gold nanorods for chemo-photothermal therapy with near-infrared radiation. **Biomaterials**, v. 34, p. 3150–3158, 2013.

75 CHEN, C. C.; LIN, Y. P.; WANG, C. W.; TZENG, H. C.; WU, C. H.; CHEN, Y. C.; CHEN, C. P.; CHEN, L. C.; WU, Y. C. DNA− gold nanorod conjugates for remote control of localized gene expression by near infrared irradiation. **J. Am. Chem. Soc.**, v. 128, p. 3709–3715, 2006.

76 YAMASHITA, S.; FUKUSHIMA, H.; AKIYAMA, Y.; NIIDOME, Y.; MORI, T.; KATAYAMA, Y.; NIIDOME, T. Controlled-release system of single-stranded DNA triggered by the photothermal effect of gold nanorods and its in vivo application. **Bioorganic Med. Chem.**, v. 19, p. 2130−2135, 2011.

77 LI, L.; TEN HAGEN, T. L. M.; HOSSANN, M.; SUSS, R.; VAN RHOON, G. C.; EGGERMONT, A. M. M.; HAEMMERICH, D.; KONING, G. A. Mild hyperthermia triggered doxorubicin release from optimized stealth thermosensitive liposomes improves intratumoral drug delivery and efficacy. **J. Controlled Release**, v. 168, p. 142−150, 2013.

78 MIALON, G.; TÜRKCAN, S.; DANTELLE, G.; COLLINS, D. P.; HADJIPANAYI, M.; TAYLOR, R. A.; GACOIN, T.; ALEXANDROU, A.; BOILOT, J. P. High up-conversion efficiency of YVO_4:Yb,Er nanoparticles in water down to the single-particle level. **J. Phys. Chem. C**, v. 114, p. 22449–22454, 2010.

79 MESSINGER, B. J.; VON RABEN, K. U.; CHANG, R. K.; BARBER, P.W. Local fields at the surface of noble-metal microspheres. **Phys. Rev. B**, v. 24, p. 649–657, 1981.

80 LU, D.; CHO, S. K.; AHN, S.; BRUN, L.; SUMMERS, C. J.; PARK, W. Plasmon enhancement mechanism for the upconversion processes in $NaYF_4:Yb^{3+},Er^{3+}$ nanoparticles: Maxwell versus Förster. **ACS Nano**, v. 8, p. 7780–7792, 2014.

81 QIAN, H.-S.; ZHANG, Y. Synthesis of hexagonal-phase core-shell $NaYF_4$ nanocrystals with tunable upconversion fluorescence. **Langmuir**, v. 24, p. 12123–12125, 2008.

82 ZHANG, H.; LI, Y.; IVANOV, I. A.; QU, Y.; HUANG, Y.; DUAN, X. Plasmonic modulation of the upconversion fluorescence in $NaYF_4$:Yb/Tm hexaplate nanocrystals using gold nanoparticles or nanoshells. **Angew. Chem. Int. Ed.**, v. 49, p. 2865–2868, 2010.

Chapter 3.

Objectives

3.1. General objective

Taking into account the state of the art presented in literature, the main goal of this thesis was to design a nanotheranostic system made of a composite nanoparticle combining an upconversion-based nanothermometer with a local nanoheater. Such particles were studied with regards to their potential to induce an increase in temperature and, consequently, to cause cell death. Furthermore, its ability to measure the local temperature should help improve the outcome PTT procedures.

To these ends, the combination of independent luminescent probes based on lanthanide ions was envisioned to obtain multiple functionalities in a single nanoplatform. Therefore, the main objective of this project was to study multifunctional materials based on lanthanide luminescence for applications in nanomedicine for sensing temperature and UV light dose.

3.2. Specific objectives

To achieve the main goal, the specific objectives include:

(i) Synthesis of Yb^{3+}:Er^{3+} co-doped $NaGdF_4$ nanocrystals

Synthesis temperature was investigated as this reaction parameter may influence the crystalline phase and size distribution. Structural characterizations were performed in order to establish the optimal synthesis conditions to obtain monodisperse particles in the hexagonal phase (well known for its higher upconversion efficiency *vs*. the cubic phase). Optical characterizations sought the highest yield of infrared-visible conversion.

(ii) Silica coating of $NaGdF_4$:Yb^{3+}:Er^3 UCNPs

The surface modification of hydrophobic UCNPs to obtain water-soluble particles allowed further coupling with metallic nanoparticles in a polar solvent. The silica coating was performed through a modified Stöber process by a reverse micro-emulsion method. The protocol was optimized by testing

different relative concentrations of surfactant, tetraethylorthosilicate (TEOS) and UCNPs, in order to obtain uniform coatings on the surface of UCNPs.

(iii) Synthesis of AuNSs@SiO_2@UCNPs

The intended nanoprobes were composed of $NaGdF_4$:Yb^{3+}:Er^3 UCNPs decorating the surface of gold nanoshells (AuNSs) with SiO_2 as an intermediate silica shell. Gold nanoshells were prepared in such that their plasmon band coincided with the excitation or emission bands of the UCNPs. This strategy was based on the facility with which the SiO_2 with surface can be functionalized with amine groups, thus facilitating their attachment to the metal nanoparticle.

(iv) Development of the temperature sensor and heating elements

The influence of temperature on visible luminescence of Er^{3+} in $NaGdF_4$:Yb^{3+}:Er^{3+} under 980-nm excitation were studied. The thermal sensitivity of the different systems obtained were calculated to estimate their ability to detect temperature. Specific properties of the nanocomposites made from upconverting nanoparticles and metal colloids, such as colloidal stability in aqueous media, luminescence intensity, and sensitivity to temperature changes, were investigated. Their potential as photothermal therapeutic agents was investigated based on the heating effect.

(v) Synthesis of $NaGdF_4$:Yb^{3+}:Er^{3+}@SiO_2-$Eu(tta)_3$

To obtain a dual-modal temperature sensor, a second active center with a different temperature-sensitive luminescence feature was added to the obtained UCNPs. The europium (III) complex $Eu(tta)_3$ (tta-thenoyltrifluoroacetonate) was prepared *in situ* on the silica shell of $NaGdF_4$:Yb^{3+}:Er^{3+} UCNPs.

(vi) Development of the dual-mode thermometer and UV light sensor

The synthesized $NaGdF_4$:Yb^{3+}:Er^{3+}@SiO_2-$Eu(tta)_3$ nanosystem was investigated to be used as a multifunctional sensor of UV light and temperature. The dual-modal temperature sensor was obtained by combining the temperature-dependent luminescence from the NIR to visible upconversion signal of Er^{3+} ions together with the UV excited downshifting emission from Eu^{3+} complex. The luminescence behavior was investigated under UV and NIR excitation at different temperatures. The effect of UV light exposure on the upconversion and downshifting emissions has also been studied. The emission spectra were measured after being exposed at different periods of UV light.

Chapter 4.

Methods

4.1. Synthesis procedures

4.1.1. Thermal decomposition synthesis

The choice of the fluoride host ($NaGdF_4$) was mainly based on its high upconversion efficiency because of low phonon energies, as mentioned before. The synthetic routes for fluoride UCNPs aim to achieve monodisperse nanocrystals with precise control over nanocrystal phase, shape, size and stoichiometric composition.[1] A variety of methodologies are reported in literature, such as thermal decomposition[2], hydro(solvo)thermal synthesis[3], sol-gel process[4], co-precipitation[5], synthesis by microemulsion[6] and ionic liquid-based synthesis[7]. Nanocrystals of high quality with sizes smaller than 20 nm may be synthesized in a non-aqueous media through a thermal decomposition process with control over size and shape.

The synthesis of colloidal $NaGdF_4$ upconverting nanoparticles doped with the ions Yb^{3+}:Er^{3+} was performed via thermal decomposition of fluoride precursors of lanthanide ions at high temperatures (>300 °C) in the presence of a coordinating ligand (oleic acid) in a non-coordinating solvent with a high-boiling point (1-octadecene). In this method, the functional group of oleic acid coordinates to the metal and the long hydrocarbon chain controls the growth of the particles and subsequently stabilizes the resulting nanoparticles against agglomeration. The method that was used, described in Hemmer *et al.*[2], is a two-pot synthesis, thereby allowing the addition of the precursors to the reaction flask over a prolonged period of ~10 min, which results in a separation of nucleation and growth processes and in narrow size distributions.

4.1.1.1. Synthesis of Gd^{3+}:Yb^{3+}:Er^{3+} trifluoroacetate precursor. In the first step of the synthesis, the lanthanide trifluoroacetate precursor was prepared through the reaction of the oxides of lanthanides, in a defined molar ratio (Gd:Yb:Er = 78:20:2), with trifluoroacetic acid at 80 °C under reflux until the solution becomes clear. The temperature was then lowered to 60 °C, and the flask was opened to evaporate the precursor to dryness for several hours.

4.1.1.2. Synthesis of Yb^{3+}:Er^{3+} co-doped $NaGdF_4$ UCNPs. In the second step, sodium trifluoroacetate and the precursor lanthanide trifluoroacetate were added to oleic acid and 1-octadecene in

a first flask (flask #1). In a second flask (flask #2), only the solvents, oleic acid and 1-octadecene, were mixed. Both flasks were connected to a Schlenk line under vacuum to remove moisture and oxygen. Subsequently, flask #2 was heated to temperatures between 310 and 320 °C under argon flow. The precursor solution present in flask #1 was then injected to flask #2. Heating was kept for 60 min. Variations of synthetic temperature of the thermal decomposition synthesis was studied to obtain the hexagonal phase.

4.1.2. Silica coating of $NaGdF_4:Yb^{3+}:Er^{3+}$ UCNPs

The synthetic strategies for the preparation of high-quality lanthanide-doped β-phase $NaY(Gd)F_4$ UCNPs are based on oil-phase methods, yielding hydrophobic UCNPs.[1] The surface modification of the obtained hydrophobic oleate-capped UCNPs was necessary to render them water dispersible, considering the intended biological applications. The two main surface modification approaches for phase transfer of nanoparticles are based on organic polymers or silica coating.[8] Silica is an inorganic polymer that presents many advantages as it is highly biocompatible, highly stable and optically transparent, and it presents abundant Si–OH active bonds available for further functionalization, such as the attachment of biological molecules.[9,10] Additionally, molecules may be stored in mesoporous silica because of its high pore volume, by electrostatic interactions or H-bonds to use as a carrier for drug delivery.[11,12]

The UCNPs were coated with a silica shell by a reverse microemulsion route.[13] Firstly, the UCNPs were dispersed in cyclohexane, and then the surfactant Igepal CO-520 was added. Tetraethylorthosilicate (TEOS) was then added and the solution was stirred for 48 h in the presence of ammonium hydroxide as a catalyst of the hydrolysis and condensation reactions. The optimization of the silica coating procedure was performed by fixing UCNPs weight and varying the amounts of TEOS or surfactant in a fixed volume of cyclohexane.

4.1.3. Synthesis of UCNP-metal nanocomposites

The fabrication of UCNP-metal nanocomposites has been generally based on three strategies[14]: (i) deposition of UCNPs on metallic films[15]; (ii) attachment or self-assembly of metallic nanoparticles onto the surface of UCNPs[16]; (iii) metallic/UCNPs or UCNPs/metallic core-shell structures, in which an intermediate silica shell with controlled thickness allows the precise control of the distance between metallic nanoparticles and UCNPs[17].

The core-shell design allows for facile particle dispersion, which is essential for biological applications. It is important to note that the metal-shell design may cause a decrease in light absorption by the UCNP core because of scattering and absorption losses caused by plasmonic nanoparticles. The UCNP shell design was chosen here for maximum light absorption by the UCNP and flexible control over the size of the metal core. UCNPs are quite small and size variations do not change drastically the optical properties as is typically the case for metal NPs.

In this work, the UCNP core-silica shell (UCNPs@SiO_2) particles were grafted onto the surface of silica core-gold nanoshell particles. The metallic nanostructures were composed of gold because of its high biocompatibility. AuNSs were our choice to study the photothermal effect as it present a plasmon resonance that overlaps the excitation of UCNPs at 980 nm. The methodology to couple the nanocomponents was based on the facility to functionalize the surface of SiO_2 with diverse groups, such as amines or thiols, thus facilitating their attachment to the metal nanoparticle.[18] In a first step, the silica surface of UCNP@SiO_2 was derivatized with an aminosilane, (3-aminopropyl)triethoxysilane (APTES). Following the functionalization, these particles will be mixed with the gold nanostructures under stirring.

4.1.4. In situ preparation of the complex $Eu(tta)_3$ at the silica shell of UCNPs

A single nanoplatform displaying multi-emissions through different processes, Er^{3+} upconversion emission and UV-excited Eu^{3+} downshifting emission, was prepared. As mentioned before, the upconversion process requires a low phonon energy host, whereas the host-activator combination is not ideal for downshifting process. In this case, the UV-excited emission demands an organic ligand to improve the absorption cross-section.[19] In this context, hybrid nanoparticles were considered to design an efficient dual-mode system composed of an inorganic core ($NaGdF_4$:Yb^{3+}:Er^{3+}) and an organic europium complex present in the silica shell. The β-diketones is the most known and used class of antenna molecules, because of their high energy transfer efficiency to Eu^{3+} and the facile β-diketonate complex synthesis.[20,21]

The Eu^{3+} complex with the β-diketone organic ligand tta (thenoyltrifluoroacetonate) was prepared *in situ* in the silica shell of UCNPs. First, europium was incorporated in the silica shell by adding europium(III) chloride hexahydrate solution in ethanol to UCNP@SiO_2. During this step, europium is adsorbed on the silica surface via an exchange between ions and water molecules.[22] Afterward, an ethanolic tta solution was added in a 3:1 molar ratio tta/Eu^{3+}. Ammonia was used to catalyse tta coordination to europium ions.

4.2. Characterizations

4.2.1. Structural characterization

The particle size of the obtained nanoparticles was firstly determined by dynamic light scattering (DLS) analysis using a Malvern Zetasizer Nano ZS instrument equipped with a 633 nm He-Ne laser, from the *Centre de recherche sur les matériaux avancés* (CERMA), Chemistry Department of Université Laval. DLS measures the hydrodynamic diameter, which includes the physical size of the particle and the solvent layer associated with the particle. Zeta potential measurements of the particles dispersed in 1 mM MES buffer solution (pH = 6.1) were performed with the same instrument to investigate the surface charge and agglomeration state of nanoparticle dispersions.

Transmission electron microscopy (TEM) was used to determine the physical size and structural morphology of the particles. The Tecnai G2 Spirit BioTwin (120 KV) transmission electron microscope at the Bioimaging platform of the Infectious Disease Research Centre of Université Laval was used.

The crystal phase of the UCNPs was investigated by X-ray Diffraction (XRD) using a Siemens D5000 Kristalloflex diffractometer using nickel-filtered and Cu Kα radiation, of the *Laboratoire de microanalyse - Diffraction-X, Département de géologie et de génie géologique* of Université Laval. The spectral processing software was JADE version 2.1 coupled with the JCPDS (Joint Committee on Powder Diffraction Standards) database of ICDD (International Centre for Diffraction Data) 2001 version.

4.2.2. Optical characterization

Upconversion luminescence spectra were measured using a FluoroLog 3 spectrofluorometer (Model 322) from Horiba Jobin-Yvon attached to an external 980 nm continuous wave diode laser (JDS Uniphase, Model S26-7602-340). A Xenon lamp was used for UV-excited visible photoluminescence. The excitation power densities at the sample position were estimated by using a power meter (Newport 2935-C). UV-visible absorption spectroscopy was used to measure the plasmon resonance of metallic nanoparticles using a Varian Cary 50 spectrophotometer. All the instruments to perform the optical characterization were available in the laboratory of Prof. Boudreau.

4.2.3. Temperature sensing

To obtain the calibration curves, the emission spectra were measured at different temperatures in a Peltier-based temperature-controlled cuvette holder coupled to the fluorometer. The spectra were registered in the proximity to the physiological range and the photothermal therapy effect (20-70 °C). A period of 10 min was given to allow the temperature to stabilize.

4.2.3.1. Er^{3+} emission-based thermometer. The Er^{3+} transitions were used to measure the temperature in the luminescent thermometer based on the Yb^{3+}:Er^{3+} systems. The emission spectra of $NaGdF_4$:Yb^{3+}:Er^{3+} (in oleate-coated UCNPs, in silica-coated UCNPs or in hybrid nanostructures UCNP-metal nanoparticles) were measured under excitation at 980 nm. The luminescent thermometers work by exploiting the drop of emission intensity with increasing temperature, due to thermal activation of nonradiative deactivation pathways. The measurement is performed by comparing the relative integrated intensity of two fluorescence lines that have a well-defined temperature dependence. The intensity of each transition is proportional to the total number of atoms (population) in a given excited state at temperature *T*:

$$I \alpha g A_{ji} h\nu \exp\left(-\frac{E}{k_B T}\right), \quad (4.1)$$

where g is the degeneracy of the state, A_{ji} is the spontaneous emission rate, ν is the frequency, h and k_B are the Planck and the Boltzmann constants, respectively, E is the energy of the level and T is the absolute temperature. Usually, two transitions assigned to the same phosphor are used and the ratio between their fluorescent intensities is taken as a measurement of absolute temperature.[23] In the case of erbium/ytterbium co-doped particles, after being excited in the near-infrared, two emission peaks located around 525 and 550 nm were measured. They correspond to transitions between the excited energy levels $^2H_{11/2}$ and $^4S_{3/2}$, respectively, and the ground level $^4I_{15/2}$, as shown in the energy level diagram bellow (Figure 4.1).

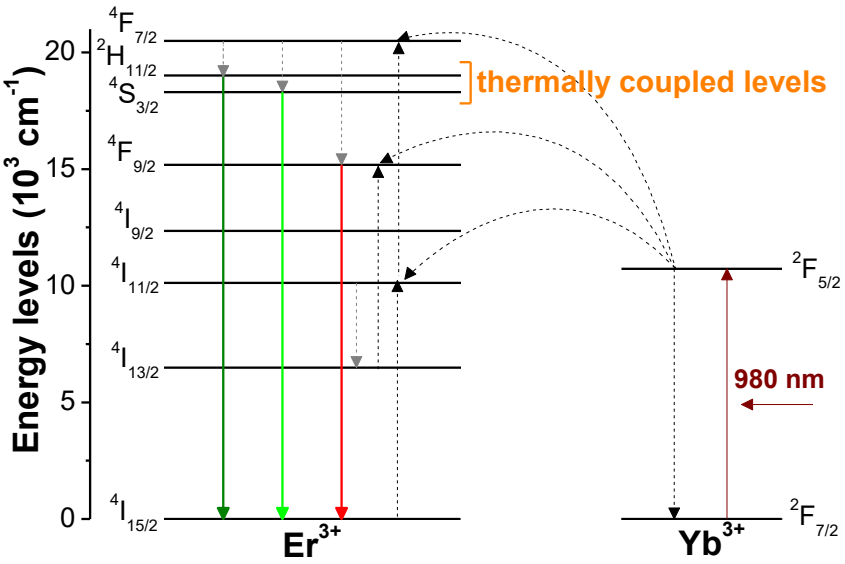

Figure 4.1. Schematic energy-level diagram of Yb^{3+} and Er^{3+} and mechanism of upconversion emissions under 980 nm laser excitation.

The $^2H_{11/2}$ and $^4S_{3/2}$ levels are in a thermal equilibrium[24] governed by the Boltzmann factor:

$$FIR = \frac{I_{525}}{I_{550}} = C\ exp\left(-\frac{\Delta E}{k_B T}\right), \tag{4.2}$$

where FIR is the fluorescence intensity ratio between the integrated intensities of the emissions at 525 and 550 nm, represented by I_{525} and I_{550}, respectively; C is a constant that depends on the degeneracy, spontaneous emission rate, and photon energies of the emitting states in the host materials; and ΔE is the energy gap separating the two excited states.[25]

4.2.3.2. Eu^{3+} emission-based thermometer. The second temperature probe investigated was based on the UV-excited downshifting emission of the $Eu(tta)_3$ complex. The ligand tta presents a strong

UV absorption cross-section allowing for the indirect excitation of Eu^{3+}, a process known as the antenna effect. The energy state diagram illustrating schematically the mechanism of ligand-sensitized Eu^{3+} emission is presented in Figure 4.2. Upon UV irradiation, the tta molecule is promoted to its first singlet excited state (S_1) and subsequent intersystem crossing (ISC) leads to its triplet excited state (T_1). A transfer of energy occurs from the T_1 state to the ^5D_J manifold of europium ion, and then nonradiative processes lead to the population of $^5D_0$ state (indicated by the dashed grey arrows). The resulting Eu^{3+} luminescence is due to the transition from $^5D_0$ level to ^7F_J manifold (J = 0, 1, 2, 3, 4), with the $^5D_0 \rightarrow {}^7F_2$ transition at 615 nm dominating the spectrum.[20,26] The Eu^{3+}-based thermometer works exploiting the relation between the red emission integrated intensity and temperature. The highly temperature-dependent emission is related to the thermal deactivation of the $^5D_0$ excited state.

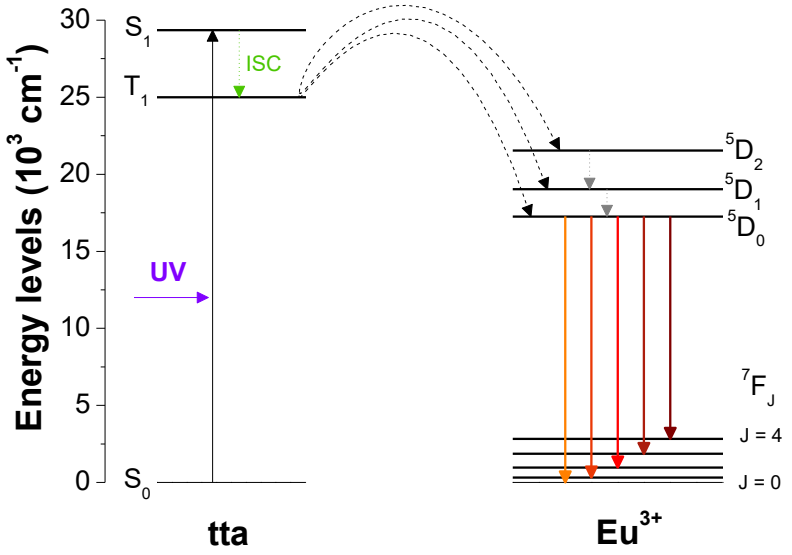

Figure 4.2. Schematic energy-level diagram showing the mechanism of energy transfer from tta to Eu^{3+} and downshifting emission under UV excitation.

4.2.3.3 Thermal sensitivity. The absolute thermal sensitivity (S) is the parameter that describe the quality of the obtained nanothermometers. It is defined as the rate at which the ratio of fluorescence intensities changes with the temperature and can be expressed as:[27]

$$S = \frac{\partial(FIR)}{\partial T} = FIR\left(\frac{\Delta E}{k_B T^2}\right), \tag{4.3}$$

in which $\Delta E/k_B$ is given by the slope of the Boltzmann's plot (Ln[FIR] *vs.* 1/T).

The relative thermal sensitivity (S_r) allows the comparison of different types of thermometers independently of their nature.[28] S_r gives the variation of the experimental parameter (Q) per degree of

temperature, which corresponds to (i) the FIR, for the ratiometric Er^{3+}-based thermometer and (ii) the integrated intensity for the nonratiometric Eu^{3+}-based thermometer. S_r can be expressed as eq. (4.4):

$$S_r = \frac{(\partial Q / \partial T)}{Q} \quad . \tag{4.4}$$

4.2.4. Photothermal effect

The temperature increase of the colloidal solutions containing UCNPs and metal nanostructures was measured under 980 nm excitation. The upconversion emission spectra were acquired at different laser power levels. The calibration curve obtained for the ratiometric upconversion luminescence temperature sensing method was used to measure the heat propagation.

4.2.5. UV light sensing

To investigate the luminescence behavior of $NaGdF_4:Yb^{3+}:Er^{3+}@SiO_2–Eu(tta)_3$ nanoparticles under UV light exposure, the calibration measurements for the UV light sensor were recorded at room temperature with a power density of 1.35 mW/cm^2 (λ = 352 nm) and 980 nm after different periods of exposure to UV light.

References

1 ZHANG, F. **Photon upconversion nanomaterials**. 1st ed. Heidelberg: Springer, 2015. 416 p. (Nanostructure science and technology).

2 HEMMER, E.; QUINTANILLA, M.; LÉGARÉ, F.; VETRONE, F. Temperature-induced energy transfer in dye-conjugated upconverting nanoparticles: A new candidate for nanothermometry. **Chem. Mater.**, v. 27, p. 235−244, 2015.

3 LIU, Q.; FENG, W.; YANG, T.; YI, T.; LI, F. Upconversion luminescence imaging of cells and small animals. **Nature Protocols**, v.8, p. 2033−2044, 2013.

4 YANG, K.; ZHENG, F.; WU, R.; LI, H.; ZHANG, X. Upconversion luminescent properties of YVO_4: Yb^{3+}, Er^{3+} nano-powder by sol-gel method. **J. Rare Earths**, v. 24, p. 162−166, 2006.

5 NIGOGHOSSIAN, K.; PERES, M. F. S.; PRIMO, F. L.; TEDESCO, A.C.; PECORARO, E.; MESSADDEQ, Y.; RIBEIRO, S. J. L. Infrared to visible up-conversion in biocellulose-yttrium vanadate nanoparticles composite membranes. Demonstration of chloroaluminum phthalocyanine light emission under up-converted light excitation. **Colloid and Interface Science Communications**, v. 2, p. 6−10, 2014.

6 LEMYRE, J.-L.; RITCEY, A. M. Synthesis of lanthanide fluoride nanoparticles of varying shape and size. **Chem. Mater.**, v. 17, p. 3040−3043, 2005.

7 LIU, X. M.; ZHAO, J. W.; SUN, Y. J.; SONG, K.; YU, Y.; DU, C.; KONG, X. G.; ZHANG, H. Ionothermal synthesis of hexagonal-phase $NaYF_4$:Yb^{3+}, Er^{3+}/Tm^{3+} upconversion nanophosphors. **Chem. Commun.**, v. 43, p. 6628−6630, 2009.

8 SPERLING, R. A; PARAK, W. J. Surface modification, functionalization and bioconjugation of colloidal inorganic nanoparticles. **Philos. Trans. A Math. Phys. Eng. Sci.**, v. 368, p. 1333–1383, 2010.

9 FADEEL, B.; GARCIA-BENNETT, A. E. Better safe than sorry: understanding the toxicological properties of inorganic nanoparticles manufactured for biomedical applications. **Adv. Drug Deliv. Rev.**, v. 62, p. 362–374, 2010.

10 HUANG, X.; LI, L.; LIU, T.; HAO, N.; LIU, H.; CHEN, D.; TANG, F. The shape effect of mesoporous silica nanoparticles on biodistribution, clearance, and biocompatibility in vivo. **ACS Nano**, v. 5, p. 5390–5399, 2011.

11 ZHANG, Z.; ZHANG, X.; NIU, D.; LI, Y.; SHI, J. Large-pore, silica particles with antibody-like, biorecognition sites for efficient protein separation. **J. Mater. Chem. B**, v. 5, p. 4214–4220, 2017.

12 ZOU, Z.; HE, D.; CAI, L.; HE, X.; WANG, K.; YANG, X.; LI, L.; LI, S.; SU, X. Alizarin complexone functionalized mesoporous silica nanoparticles: A smart system integrating glucose-responsive double-drugs release and real-time monitoring capabilities. **ACS Appl. Mater. Interfaces**, v. 8, p. 8358–8366, 2016.

13 LI, Z.; ZHANG, Y.; JIANG, S. Multicolor core/shell-structured upconversion fluorescent nanoparticles. **Adv. Mater.**, v. 20, p. 4765–4769, 2008.

14 CHEN, G.; QIU, H.; PRASAD, P. N.; CHEN, X. Upconversion nanoparticles: Design, nanochemistry, and applications in Theranostics. **Chem. Rev.**, v. 114, p. 5161–5214, 2014.

15 ZHANG, H.; XU, D.; HUANG, Y.; DUAN, X. Highly spectral dependent enhancement of upconversion emission with sputtered gold island films. **Chem. Commun.**, v. 47, p. 979–981, 2011.

16 LIU, N.; QIN, W.; QIN, G.; JIANG, T.; ZHAO, D. Highly plasmon-enhanced upconversion emissions from Au@β-$NaYF_4$:Yb,Tm hybrid nanostructures. **Chem. Commun.**, v. 47, n. 27, p. 7671–7673, 2011.

17 ZHANG, F.; BRAUN, G. B.; SHI, Y.; ZHANG, Y.; SUN, X.; REICH, N. O.; ZHAO, D.; STUCKY, G. Fabrication of Ag@SiO_2@Y_2O_3:Er nanostructures for bioimaging: Tuning of the upconversion fluorescence with silver nanoparticles. **J. Am. Chem. Soc.**, v. 132, p. 2850–2851, 2010.

18 RYU, J. H.; Han, S. S.; Kim, D. H.; Henkelman, G.; Lee, H. M. Ligand-induced structural evolution of Pt55 nanoparticles: amine versus thiol. **ACS Nano**, v. 5, p. 8515–8522, 2011.

19 SINGH, P.; SHAHI, P. K.; SINGH, S. K.; SINGH, A. K.; SINGH, M. K.; PRAKASH, R.; RAI, S. B. Lanthanide doped ultrafine hybrid nanostructures: multicolour luminescence, upconversion based energy transfer and luminescent solar collector applications. **Nanoscale**, v. 9, p. 696–705, 2017.

20 REDDY, M. L. P.; DIVYA, V.; PAVITHRAN, R. Visible-light sensitized luminescent europium (III)-β-diketonate complexes: bioprobes for cellular imaging. **Dalton Trans.**, v. 42, p. 15249–15262, 2013.

21 BINNEMANS, K. Lanthanide-based luminescent hybrid materials. **Chem. Rev.**, v. 109, p. 4283-4374, 2009.

22 NASSAR, E. J.; CIUFFI, K. J.; RIBEIRO, S. J. L.; MESSADDEQ, Y. Europium incorporated in silica matrix obtained by sol-gel: luminescent materials. **Mat. Res.**, v. 6, p. 557–562, 2003.

23 BRITES, C. D. S.; LIMA, P. P.; SILVA, N. J. O.; MILLÁN, A.; AMARAL, V. S.; PALACIO, F.; CARLOS, L. D. Lanthanide-based luminescent molecular thermometers. **New J. Chem.**, v. 35, p. 1177–1183, 2011.

24 ALENCAR, M. A. R. C.; MACIEL, G. S.; de ARAÚJO, C. B.; PATRA, A. Er^{3+}-doped $BaTiO_3$ nanocrystals for thermometry: influence of nanoenvironment on the sensitivity of a fluorescence based temperature sensor. **Appl. Phys. Lett.**, v. 84, p. 4753–4755, 2004.

25 VETRONE, F.; NACCACHE, R.; ZAMARRÓN, A.; DE LA FUENTE, A. J.; SANZ-RODRÍGUEZ, F.; MAESTRO, L. M.; RODRIGUEZ, E. M.; JAQUE, D.; SOLÉ, J. G.; CAPOBIANCO, J. A. Temperature sensing using fluorescent nanothermometers. **ACS Nano**, v. 4, p. 3254–3258, 2010.

26 BINNEMANS, K. Interpretation of europium (III) spectra. **Coord. Chem. Rev.**, v. 295, p. 1-45, 2015.

27 QUINTANILLA, M.; CANTELAR, E.; CUSSÓ, F.; VILLEGAS, M.; CABALLERO, A. C. Temperature sensing with up-converting submicron-sized $LiNbO_3$:Er^{3+}/Yb^{3+} particles. **Appl. Phys. Express**, v. 4, p. 022601-1–022601-3, 2011.

28 CARLOS, L. D.; PALACIO, F. (Eds.). **Thermometry at the nanoscale: Technique and selected applications.** Oxfordshire: Royal Society of Chemistry, 2016. 522 p.

Chapter 5.

Upconversion nanoparticle-decorated gold nanoshells for near-infrared induced heating and thermometry

Résumé

Le présent travail implique le développement d'un système multifonctionnel, basé sur des nanocoquilles d'or (AuNSs) décorées avec des nanoparticules à conversion ascendante d'energie (UCNPs), destiné à être un chauffant optique et une sonde de température à l'échelle nanométrique. La synthèse des UCNPs de $NaGdF_4$ dopées avec les ions Yb^{3+} et Er^{3+} a été réalisée par décomposition thermique de précurseurs de fluorures de lanthanide à température elevée (> 300 °C) en présence d'un ligand de coordination (l'acide oléique). Les UCNPs ont été synthétisées à trois températures différentes (310, 315 et 320 °C) et caractérisées en termes des propriétés morphologiques, de structure et d'émission. Compte tenu des applications biologiques prévues, la surface hydrophobe des UCNPs recouvert d'oléate a été modifiée par un revêtement de silice afin d'obtenir une bonne dispersabilité dans l'eau, au moyen d'un processus Stöber adapté au moyen d'une méthode de microémulsion inverse. Des nanocristaux monodisperses de $NaGdF_4$:Yb^{3+}:Er^{3+} à conversion ascendante (~ 25 nm de diamètre) ont été obtenus en phases cubique (à 310, 315 °C) et hexagonale (à 320 °C). Les UCNPs dans la phase hexagonale étaient plus appropriées en tant que capteurs de température en raison du rapport faible entre les émissions rouge/vert et une plus grande sensibilité thermique. Le spectre d'émission des UCNP (recouvertes de silice ou d'oléate) a été enregistré à des températures différentes à proximité de la plage physiologique (20–70 °C) et a révélé des propriétés appropriées pour leur application comme capteur de température, comme une excellente linéarité (R^2 > 0,99) et une bonne sensibilité (>3 × 10^{-3} K^{-1}). La capacité de chauffage des AuNSs@UCNPs a été vérifiée par le suivi de l'émission de l'Er^{3+}, ce qui démontre son potentiel d'application comme agent d'hyperthermie contrôlée par l'utilisation de la fonction de nanothermomètre.

Resumo

O presente trabalho envolve o desenvolvimento de um sistema multifuncional, a base de nanocascas de ouro (AuNSs) decoradas com nanopartículas para conversão ascendente de energia (UCNPs), destinado a ser um aquecedor óptico e uma sonda de temperatura em escala nanométrica. A síntese das UCNPs de $NaGdF_4$ dopadas com os íons Yb^{3+} e Er^{3+} foi realizada *via* decomposição térmica de precursores de fluoreto de lantanídeo a alta temperatura (> 300 °C) na presença de um ligante coordenante (o ácido oleico). As UCNPs foram sintetizadas a três diferentes temperaturas (310, 315 e 320 °C) e caracterizadas em termos das propriedades morfológicas, estruturais e de emissão. Levando-se em conta as aplicações biológicas pretendidas, a superfície hidrofóbica recoberta por oleato das UCNPs foi modificada utilizando um revestimento de sílica para obter uma boa dispersão em água, por meio de um processo Stöber adaptado por um método de microemulsão reversa. Nanocristais monodispersos de $NaGdF_4$:Yb^{3+}:Er^{3+} para conversão ascendente (~ 25 nm de diâmetro) foram obtidos nas fases cúbica (a 310, 315 °C) e hexagonal (a 320 °C). As UCNPs na fase hexagonal mostraram-se mais apropriadas como sensores de

temperatura, devido a menor razão entre as emissões vermelho/verde e maior sensibilidade térmica. O espectro de emissão das UCNPs (recobertas por sílica ou por oleato) foi registrado a diferentes temperaturas na proximidade do intervalo fisiológico (20–70 °C) e apresentou as propriedades adequadas para sua aplicação como sensor de temperatura, como uma excelente linearidade (R^2 > 0,99) e uma boa sensibilidade (>3 × 10^{-3} K^{-1}). A capacidade de aquecimento das AuNSs@UCNPs foi verificada pelo monitoramento da emissão do Er^{3+}, a qual demonstra seu potencial para aplicação como um agente em hipertermia controlada pela utilização da função de nanotermômetro.

Abstract

The present work involves the design of a multifunctional system based on gold nanoshells (AuNSs) decorated with lanthanide-based upconversion nanoparticles (UCNPs) intended as an optical heater and a temperature probe at the nanoscale. The synthesis of $NaGdF_4$ UCNPs doped with ions Yb^{3+}:Er^{3+} was performed *via* thermal decomposition of lanthanide fluoride precursors at high temperatures (>300 °C) in the presence of a coordinating ligand (oleic acid). UCNPs were synthesized at three different temperatures (310, 315 and 320 °C) and characterized in terms of morphological, structural and emission properties. In view of the intended biological applications, the surface of hydrophobic oleate-capped UCNPs was modified using a silica coating to achieve sufficient water dispersibility, through a modified Stöber process using a reverse microemulsion method. Monodisperse $NaGdF_4$:Yb^{3+}:Er^{3+} upconversion nanocrystals (~25 nm dia.) were obtained in cubic (at 310, 315 °C) and hexagonal (at 320 °C) phases. The UCNPs in the hexagonal phase were shown to be more suitable as temperature sensors, because of their lower red-to-green emission ratios and higher thermal sensitivities. The emission spectrum of $NaGdF_4$:Yb^{3+}:Er^{3+} (oleate- or silica-coated) UCNPs was recorded at different temperatures in the vicinity of the physiological range (20–70 °C) and presented suitable properties for application as temperature sensors, such as excellent linearity (R^2 > 0.99) and sensitivity (>3 × 10^{-3} K^{-1}). The heating capacity of AuNSs@UCNPs was verified by monitoring the Er^{3+} emission, showing their potential for application as a hyperthermia agent controlled using a nanothermometer function.

5.1. Introduction

Temperature is an essential parameter that governs dynamics in the life cycle of biological cells. Biochemical reactions and cell activities, such as cell division and gene expression, lead to constant variations in intracellular temperature.[1–3] Pathological cells (*e.g.* cancer cells) display higher temperatures in comparison to healthy ones, because of an increase in metabolic activity.[4] Thus, measuring the cell temperature at the cellular level allows the diagnosis of pathologies and optimization of therapeutic processes.

External heating of a tumor tissue above its normal temperature may be useful to induce the damage and death of cancer cells. Hyperthermia is a thermal therapy modality that applies moderate localized heating up to a cytotoxic level (in the temperature range between 41 and 45 °C) with minimal damage to surrounding noncancerous tissues.[5] Although it is a much less invasive technique compared to most conventional antitumor treatments (surgery, radiotherapy and chemotherapy), the selectivity of hyperthermia is still limited by the lack of control on the heating rate[6] and is thus administered in combination with other treatment techniques.[7]

Nanotechnology has provided the means for the development of well-localized heating techniques.[8,9] Gold nanoparticles are efficient sources for heating when illuminated within their surface plasmon resonance (SPR) band because of the enhancement of light absorption. This light-induced hyperthermia behavior allows the application of these materials to induce localized thermal damage of a diseased tissue in a process known as photothermal therapy (PTT).[10] More complex geometries (including nanocages, nanorods and nanoshells) lead to plasmons in the near infrared (NIR) wavelengths, which allows deeper tissue penetration than visible light as it matches the biological transparency window.[11]

A temperature detector in a PTT procedure is important for better control of the NIR irradiation and to regulate the heat released into the surrounding medium, thereby permitting therapy guidance.[12] Such an application requires a noninvasive technique for a remote measurement of temperature with high spatial resolution.[13] A noncontact thermometer at the nanoscale may be obtained from the fluorescence signal of lanthanide ions.[14] This technique is based on measuring the fluorescence intensity ratio (FIR) between two luminescence bands that originate from thermally coupled energy levels. The relative populations of these levels follow a Boltzmann type distribution. The most commonly used dopant ion in lanthanide-based thermometers is erbium (Er^{3+}) because of the strong temperature dependence of the relative intensity of its two green emission lines, associated with the effect of thermal equilibrium in the population of excited states ($^2H_{11/2}$; $^4S_{3/2}$).[15]

Moreover, lanthanide-based upconversion nanoparticles (UCNPs) have been proposed as an ideal bio-probe for biological labeling and imaging because of their unique advantages.[15–17] One of the interesting features of trivalent lanthanide ions (Ln^{3+}) concerns the possibility of obtaining materials presenting upconversion properties, *e.g.* visible emission obtained by excitation in the NIR region.[18] Compared to conventional luminescent materials, such as organic dyes and quantum dots, the upconversion anti-Stokes emission allows sensitive detection without the usual interference from autofluorescence background and lessened photo-damage because of low-energy excitation photons.[19] Fluorides such as $NaGdF_4$ present low phonon energies (~ 350 cm^{-1}), thus making them ideal hosts.[20] UCNPs are typically doped with ytterbium (Yb^{3+}) sensitizer ions, which absorb infrared radiation (usually at 980 nm) and non-radiatively transfer their excitation to activator ions such as Er^{3+}.[21] Vetrone *et al.*[22] first demonstrated Ln^{3+} doped fluorescent nanomaterials ($NaYF_4$:Yb^{3+}:Er^{3+}) capable of accurately determining the temperature in HeLa cancer cells from 25 °C to its thermally induced death at 45 °C.

As UCNPs are one of the most important luminescent nanomaterials, the development of multifunctional nanosystems based on lanthanides could have a great impact in nanomedicine. During recent years, researchers have been proposing dual-particle approaches that combine nanoheaters and nanothermometers in a single platform to monitor the local temperature increase around and thus help regulate hyperthermia.[23–26] The systems were improved by shifting SPR from visible[23,24] to NIR[25,26] to match the excitation wavelength of Yb^{3+} and hence allow simultaneous excitation of both nanocomponents using a single laser operating at 980 nm. However, the dispersibility of heater/thermometer nanoparticles is still a challenge, and materials described in most recent works are in the form of films[25] and powders.[26]

In the present work, a multifunctional heater/thermometer system based on the combination of $NaGdF_4$:Yb^{3+}:Er^{3+} UCNPs and gold nanoshells (AuNSs) was prepared. The core–shell design facilitates the particle dispersion, which is essential for biological applications. This system was studied in the context of its application as a photothermal agent, guided by the thermal capacity of UCNPs.

5.2. Experimental details

5.2.1 Materials

Lanthanide oxides 99.9% (gadolinium oxide, ytterbium oxide and erbium oxide), trifluoroacetic acid (99%), sodium trifluoroacetate (98%), oleic acid (90%), 1-octadecene (90%), Igepal® CO-520, ammonium hydroxide (28.0–30.0%), tetraethyl orthosilicate (TEOS, 98%), (3-aminopropyl)triethoxysilane (APTES, 99%), tetrakis(hydroxymethyl)phosphonium chloride solution (80%), sodium hydroxide (>97%), gold(III) chloride trihydrate (>99.9%), potassium carbonate (99.0%), formaldehyde solution (37%), polyvinylpyrrolidone (average mol wt 10 000), and acetic acid (99.7%) were purchased from Sigma-Aldrich, St. Louis, USA and used without further purification.

5.2.2. Synthesis of Yb^{3+}:Er^{3+} co-doped $NaGdF_4$ UCNPs

The synthesis of colloidal $NaGdF_4$ upconversion nanoparticles doped with Yb^{3+}:Er^{3+} ions was performed *via* thermal decomposition of fluoride precursors of lanthanide ions. The method described previously by Hemmer *et al.*[27] is a two-pot synthesis. In the first step of the synthesis, the lanthanide trifluoroacetate precursor was prepared. A 10 mL mixture of trifluoroacetic acid and water (1 : 1) was added to a 50 mL three-neck round bottom flask containing gadolinium oxide (353.4mg, 0.975mmol), ytterbium oxide (98.5mg, 0.250 mmol) and erbium oxide (9.6 mg, 0.025 mmol) to obtain a molar ratio Gd:Yb: Er = 78 : 20 : 2. The solution was refluxed at 80 °C for 12 h until the solution becomes clear. The temperature was then lowered to 60 °C, and the flask was opened to let water and trifluoroacetic acid evaporate to dryness for 5 h. In the second step, 340 mg of sodium trifluoroacetate was added to the flask in which the precursor lanthanide trifluoroacetate was previously prepared, followed by the addition of 7.5 mL of each oleic acid and 1-octadecene. In a separate reaction vessel (a three-neck round bottom flask of 100 mL), 12.5 mL of each oleic acid and 1-octadecene were mixed. Both flasks were connected to a Schlenk line to remove moisture and oxygen for 30 min at 125 °C under vacuum and magnetic stirring. Subsequently, the reaction flask containing only oleic acid and 1-octadecene was heated to 310 °C under argon flow at a heating rate of 10 °Cmin^{-1} and a few minutes after reaching this temperature, the precursor solution was heated to 125 °C, collected with a glass syringe and injected dropwise into the reaction vessel using a syringe pump at an injection rate of 1.5 mL min^{-1}. The solution was maintained at 310 °C for an additional 60 min under stirring and argon flow. After this period, the heating source was removed. When the solution reached room temperature, the resulting nanoparticles were precipitated by

addition of ethanol and centrifuged at 5500 RCF for 10 min. The nanoparticles were washed twice by dispersing in hexane, followed by precipitation with ethanol (1 : 5 v/v), and recovery by centrifugation. The resulting oleate-capped $NaGdF_4$:Er^{3+}:Yb^{3+} nanoparticles were finally redispersed in hexane for further characterization.

5.2.3. Silica coating of $NaGdF_4$:Yb^{3+}:Er^{3+} UCNPs

The obtained UCNPs were coated with a silica shell by a reverse microemulsion method.[28] Firstly, 32 mg of UCNPs was dispersed in 10 mL of cyclohexane, and 0.4 g of Igepal CO-520 surfactant was added to form a water-in-oil microemulsion. After 10 min of stirring, an additional 1.6 g of Igepal CO-520 and 80 mL of ammonium hydroxide were added. The emulsion was sonicated for 30 min to ensure a uniform distribution of nanocrystals within the micelles. 40 mL of TEOS was then added and the solution was stirred at 300 rpm for 48 h. The nanoparticles were precipitated by adding acetone, washed twice with ethanol/water (1 : 1) and recovered by centrifugation at 1590 RCF for 20 min. The UCNPs core–silica shell (UCNPs@SiO_2) particles were finally stored in 50 mL of water until further use.

5.2.4. Synthesis of SiO_2@Au nanoshells

5.2.4.1. Silica cores. The gold nanoshells were prepared using a multistep synthesis process adapted from Halas *et al*.[29] First, the silica cores were obtained by a modified Stöber protocol.[30] In a 125 mL flask, 50 mL of ethanol/deionized water mixture (9 : 1) was maintained under vigorous stirring and 1.5 mL of TEOS was added. Once the solution became homogenous, 3 mL of ammonium hydroxide was added. The mixture was allowed to react overnight before being purified by centrifugation (5000 RCF, 15 min, 3 times) and redispersed in the same amount of anhydrous ethanol.

5.2.4.2. SiO_2@NH_2. Due to the non-vitreophilic nature of gold, the surface of silica cores must be primed by amino silane moieties. The silica NPs obtained as described above were mixed with 5 equivalents of APTES (assuming a surface coverage of 0.6 nm^2 per molecule).[31] To do so, 775 mL of a 1% APTES solution was added to 50 mL of the silica NP solution. To allow the condensation of the organosilane on the surface of the silica cores, 1.5 mL of ammonium hydroxide was added and allowed to react overnight. The suspension was washed several times with anhydrous ethanol followed by centrifugation (1500 RCF, 15 min), and the NPs were redispersed in ethanol (50 mL).

5.2.4.3. Gold seeds. Even with amine functionalization, the silica surface is not very conducive to the deposition of a gold layer. To facilitate the formation of the gold shell, the amine-terminated silica cores were decorated by gold seeds acting as anchor points for gold deposition. The gold seeds were prepared following the Duff method.[32] In a 100 mL round bottomed flask, 45.5 mL of deionized water was mixed with 1.5 mL of 0.2 M sodium hydroxide and 1 mL of 7×10^{6} M THPC solution. After stirring for 2 minutes, 2 mL

of 25 mM $HAuCl_4$ solution was quickly added. The fast reaction is completed within 5 min. The reacted solution has a dark brown appearance, which is characteristic of 1.5 nm diameter gold seeds.

5.2.4.4. SiO_2@seeds. A 10 mL aliquot of the seeds (as prepared above) was mixed with a 500 mL aliquot of the silica core suspension, and adhesion of the seeds on the amine-modified surface was aided by lowering the pH below 4 with the addition of 1.6 mL of 1 M acetic acid. At this pH, the primary amines are protonated, thus allowing a higher yield and more homogenous seed coverage.[33] The excess of seeds was removed by centrifugation (1500 RCF, 15 min, 3 times) and the compound nanoparticles were redispersed in 5 mL of deionized water.

5.2.4.5 Shell growth. The gold plating solution, referred to as K-gold, was obtained by dissolving 25 mg of K_2CO_3 in 100 mL of deionized water in a 125 mL flask, followed by the addition of 1.5 mL of 25 mM $HAuCl_4$. The K-gold solution was allowed to mature under mild stirring and protected from ambient light for 12 h. Then, 8 mL of this matured K-gold solution was mixed with 0.4 mL of the SiO_2@seed NP solution in a 20 mL vial. 500 mL of an aqueous solution of 1.48 mM PVP was added to the mixture under vigorous stirring as a stabilizing agent for the resulting nanoshells, followed by 10 mL of formaldehyde to reduce the unreacted gold ions. The NPs were allowed to react overnight before washing with ethanol and centrifugation (1500 RCF, 15 min, 3 times), and finally redispersed in 5 mL of anhydrous ethanol.

5.2.5. Synthesis of nanocomposite AuNSs@UCNPs

The synthetic route to attach UCNPs@SiO_2 to the AuNS surface was based on silica shell modification with amine groups, thus facilitating their attachment to the SiO_2@Au nanoshells.

5.2.5.1. UCNPs@SiO_2–NH_2. The synthesis of amino functionalized silica shell on UCNPs was performed following a modified protocol described in Section 5.2.3. After 48 h of TEOS reaction for silica coating on UCNPs, 100 mL of APTES was directly added to the microemulsion system and stirring was continued for an additional 4 h. Precipitation with acetone and washing with ethanol/water (1 : 1) followed by centrifugation at 1590 RCF for 20 min were performed twice. The UCNPs@SiO_2–NH_2 nanoparticles were finally redispersed in 50 mL of anhydrous ethanol.

5.2.5.2. UCNP attachment on AuNSs. The obtained colloidal solutions of AuNSs and UCNPs@SiO_2–NH_2 were mixed in a 1 : 1 volume mixture (0.75 mL of each solution) and placed on a thermomixer (Eppendorf) overnight at 800 rpm and 25 °C. The particles were centrifuged at 1500 RCF for 12 minutes, washed twice with anhydrous ethanol and redispersed in 1.5 mL of water.

5.2.6. Morphological and structural characterization

A Tecnai G2 Spirit BioTwin (120 kV) transmission electron microscope (TEM) was used to determine the physical size and structural morphology of the particles. The crystal phase of the UCNPs was investigated using X-ray diffraction (XRD) on a Siemens D5000 Kristalloflex diffractometer with nickel-filtered Cu Kα radiation. The spectral processing software used is JADE version 2.1 coupled with the JCPDS (Joint Committee on Powder Diffraction Standards) database of ICDD (International Centre for Diffraction Data) 2001 version. Zeta potential measurements of the particles dispersed in 1 mM MES buffer solution (pH = 6.1) were performed with a Malvern Zetasizer Nano ZS.

5.2.7. Optical characterization

The nanoparticles' upconversion luminescence spectra were recorded using a FluoroLog 3 spectrofluorometer (Model 322) from Horiba Jobin-Yvon attached to an external 980 nm continuous wave diode laser (JDS Uniphase, Model S26-7602-340). UV-visible absorption spectroscopy was performed on a Varian Cary 5000 spectrophotometer.

5.2.8. Temperature sensing

The luminescent thermometer was based on the Yb^{3+}:Er^{3+} system and the Er^{3+} transitions were used to measure the temperature. The emission spectra of $NaGdF_4$:Yb^{3+}:Er^{3+} (in oleate-coated UCNPs, in silica-coated UCNPs or in hybrid UCNP–gold nanostructures) were recorded at different temperatures in a Peltier-based temperature-controlled cuvette holder (F3004, Jobin-Yvon, Horiba) coupled to a fluorometer. The spectra were registered in a temperature range relevant to the physiological range and the photothermal therapy effect (20–70 °C). A period of 10 min was observed between measurements to allow for the temperature to stabilize.

5.2.9. Photothermal effect

The temperature increase of the colloidal solutions containing UCNPs and metal nanostructures was measured under 980 nm excitation. The upconversion emission spectra were acquired for different laser power levels. The obtained thermal calibration curves were used to measure the heat propagation.

5.3. Results and discussion

5.3.1. Oleate-capped $NaGdF_4$:Yb^{3+}:Er^{3+} UCNPs

The synthesis of colloidal $NaGdF_4$ upconversion nanoparticles doped with Yb^{3+}:Er^{3+} ions was performed *via* thermal decomposition of fluoride precursors of lanthanide ions at high temperatures (>310 °C), in the presence of a coordinating ligand (oleic acid) and a non-coordinating reaction solvent with a high-boiling point (1-octadecene). The reaction temperature is an important parameter in thermal

decomposition synthesis of $NaGdF_4$:Yb^{3+}:Er^{3+}, which influences nanoparticle size and shape, in addition to their crystal phase and optical properties. Therefore, the UCNPs were produced at three different reaction temperatures (310, 315 and 320 °C) and characterized in terms of morphological, structural and emission properties.

TEM images of oleate-capped particles (Figure 5.1a) present a hexagon-shaped morphology exhibited by UCNPs. At 310 °C, the particle size was 23.0 ± 3.1 nm with a broad size distribution (Figure 5.1b) spanning 15–30 nm. At 315 and 320 °C, the size distribution (Figure 5.1b) became narrower, ranging from 13 to 21 nm and 24 to 33 nm, with particle sizes of 17.4 ± 1.4 nm and 26.2 ± 1.7 nm, respectively. According to the La Mer model, the separation of nucleation and growth processes leads to narrow size distributions and the wider size distribution observed at the lower reaction temperature (310 °C) may be due to nucleation and growth processes occurring concomitantly. At more elevated temperatures (315–320 °C), nucleus formation occurs rapidly because of the fast decomposition of precursors, resulting in a homogeneous growth process. The particle size increase observed from 315 to 320 °C is due to the preferential growth mechanism.[34]

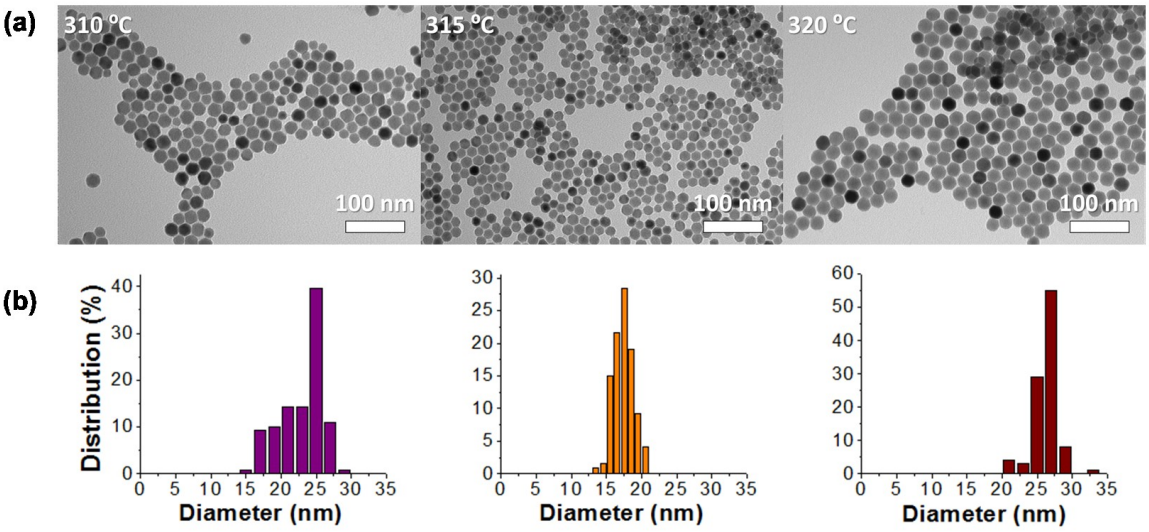

Figure 5.1. (a) TEM images of $NaGdF_4$:Yb^{3+}:Er^{3+} nanoparticles prepared at 310, 315 and 320 °C and (b) their respective particle size distributions.

X-ray diffraction patterns and phase references of $NaGdF_4$ are presented in Figure 5.2. At 310 and 315 °C, the patterns were in accordance with a cubic phase (JCPDS file 27-0698). A phase transformation from cubic (α) to hexagonal (β) occurred at 320 °C, as the reflections could be exclusively attributed to the hexagonal phase (JCPDS file 27-0699).

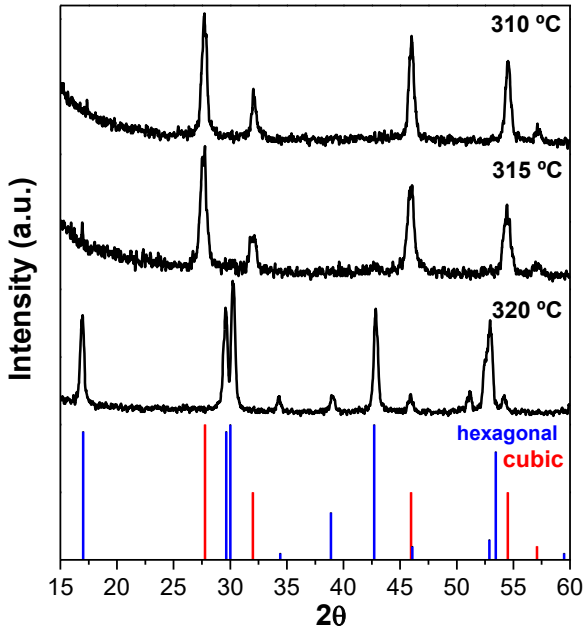

Figure 5.2. XRD patterns of $NaGdF_4:Yb^{3+}:Er^{3+}$ UCNPs prepared at different temperatures. Reference diffraction peaks corresponding to cubic and hexagonal $NaGdF_4$.

The effect of reaction temperature (from 280-320 °C) on particle size, morphology, and phase was investigated by Naccache[35] for the synthesis of $NaGdF_4:Yb^{3+}:Er^{3+}$ by the same methodology used in the present work (injection rate of 1.5 mL min^{-1} and reaction time of 60 min). The lower reaction temperature (280 °C) rendered highly polydisperse and irregularly shaped nanoparticles. At 290 °C, polydispersity is reduced, particles assume rounded morphology and self-assembly behaviour is observed. Hexagonal shape is first observed at 300 °C. More elevated temperatures favor homogeneous growth process, rendering monodispese particles at 310 °C with 15.4 ± 1.9 nm average size. At very high temperatures (320 °C) preferential growth mechanism to the detriment of nucleation results in significant increase in average size (80.7 ± 7.2 nm). The X-ray powder diffraction analysis combined with Rietveld fitting showed that at 280 °C cubic and hexagonal phases are equivalently present, and at 290 °C pattern is predominantly cubic (~90%) with some hexagonal contribution. For synthesis at 300-320 °C, the hexagonal phase is grater than 95%. In the structure of cubic phase, sodium and rare earth ions are randomly distributed in the cationic sublattice, while cation sites have three types in the hexagonal structure, thus being the more thermodynamically stable phase. The reaction temperature increase favors overcome the energy barrier for the cubic to hexagonal transition.[36]

Figures 5.3a,c shows the effect of laser excitation power at 980 nm on the upconversion emission of α -UCNPs and β-UCNPs (prepared at 315 and 320 °C). The observed bands in the spectral regions of 510–536 nm, 536–575 nm and 625–700 nm correspond to Er^{3+} transitions $^4S_{3/2} \rightarrow {}^4I_{15/2}$, $^4F_{9/2} \rightarrow {}^4I_{15/2}$ and $^2H_{11/2} \rightarrow {}^4I_{15/2}$, respectively. The red-to-green emission ratio of α-UCNPs is higher than β-UCNPs, as expected from the literature, as well as the higher upconversion efficiency of the hexagonal phase.[37–39]

The number of infrared photons (n) that are sequentially absorbed by Yb^{3+} and transferred to Er^{3+} ions leading to the emission of one visible photon may be taken as the slope of the plot of the intensity of emission (I_{em}) *vs*.pumping intensity (I_{ex}), expressed as the non-linear relation $I_{em} \propto (I_{ex})^n$. The values of n obtained suggest two-photon processes for the excitation of green and red emissions in both samples analysed (Figures 5.3b,d).

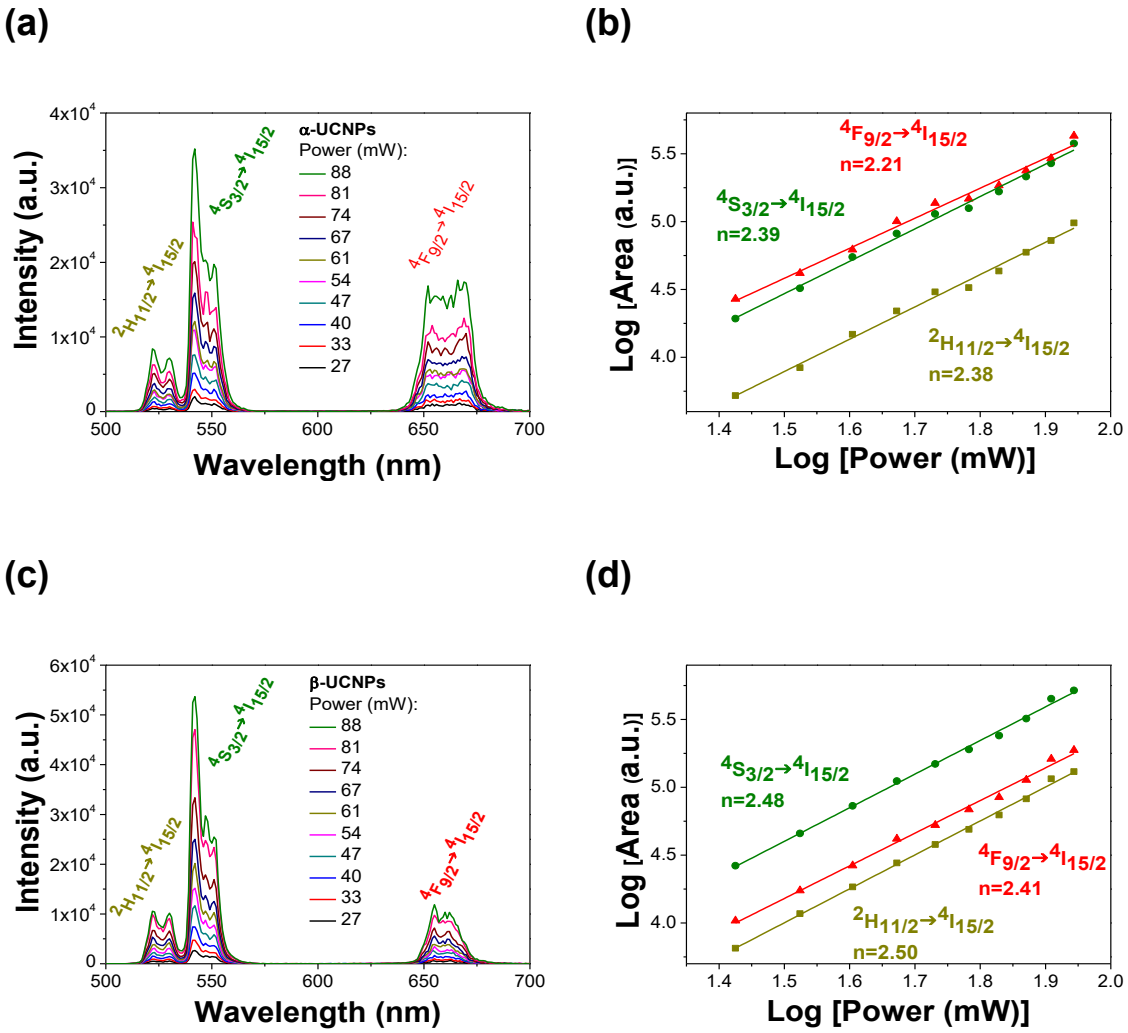

Figure 5.3. Upconversion emission spectra obtained using 980 nm laser pumping at different powers for α-UCNPs (a) and β-UCNPs (c). Integrated intensity (areas) *vs*. pumping intensity for α-UCNPs (b) and β-UCNPs (d).

5.3.2. Silica-coated $NaGdF_4$:Yb^{3+}:Er^{3+} UCNPs

The multifunctionalization of UCNPs for biological applications requires water dispersibility, biocompatibility and the possibility of subsequent surface (bio)functionalization. The post-synthetic procedures applied to hydrophobic UCNPs may involve one of two strategies: (i) the deposition of either an additional amphiphilic or silica coating onto the original hydrophobic ligands, or (ii) the complete

exchange of the original hydrophobic capping using a hydrophilic ligand.[40] Silica coating is the most common technique for nanoparticle surface modification because of its high biocompatibility. Additionally, silica is known to be highly stable and optically transparent, to present abundant Si–OH active bonds available for surface functionalization, and to have high pore volumes where drug molecules may be stored.[41] The hydrophobic surface of the obtained UCNPs was modified to make them water soluble, thereby allowing further coupling with gold nanoshells in a polar solvent. The TEM image of silica-coated UCNPs (Figure 5.4a) showed a uniform silica shell on the nanocrystal surface. The particle-size distribution (Figure 5.4b) indicated that the thickness of the silica shell was about 7 nm.

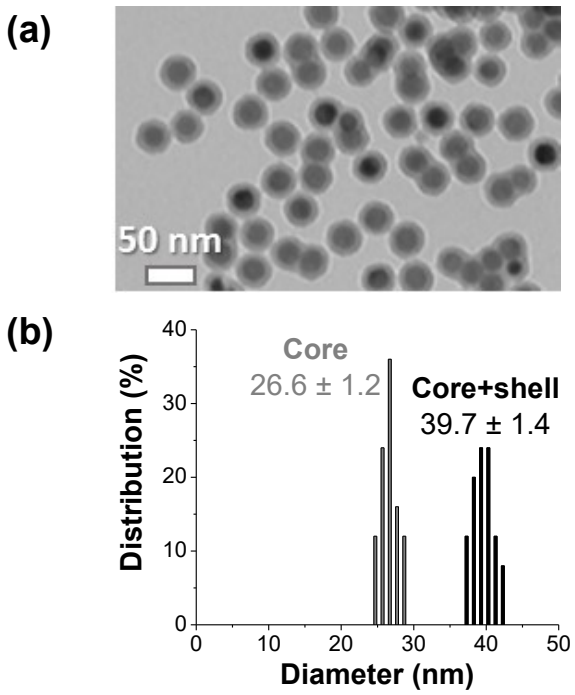

Figure 5.4. (a) TEM image and (b) particle-size distribution of silica-coated UCNPs.

5.3.3. Temperature sensing

The luminescent thermometers based on Yb^{3+}:Er^{3+} co-doped particles work by measuring the relative integrated intensity of two fluorescence lines that have a well-defined temperature dependence. They correspond to the two emission peaks observed around 525 and 550 nm that originate from the transitions between the thermal coupled excited levels $^2H_{11/2}$ and $^4S_{3/2}$, respectively, and the ground level $^4I_{15/2}$, as shown in the energy level diagram (Figure 5.5). Thus, the ratio of their fluorescence intensities is taken as a measurement of absolute temperature.[42] The $^2H_{11/2}$ and $^4S_{3/2}$ levels are in a thermal equilibrium[43] governed by the Boltzmann factor:

$$\mathrm{FIR} = \frac{I_{525}}{I_{550}} = C \exp\left(-\frac{\Delta E}{k_B T}\right), \tag{5.1}$$

where FIR is the fluorescence intensity ratio between the integrated intensities of the emissions at 525 and 550 nm, represented by I_{525} and I_{550}, respectively; C is a constant that depends on the degeneracy, spontaneous emission rate, and photon energies of the emitting states in the host materials; and ΔE is the energy gap separating the two excited states. The intensity of each transition is proportional to the total number of atoms (population) in a given excited state at temperature T.[40]

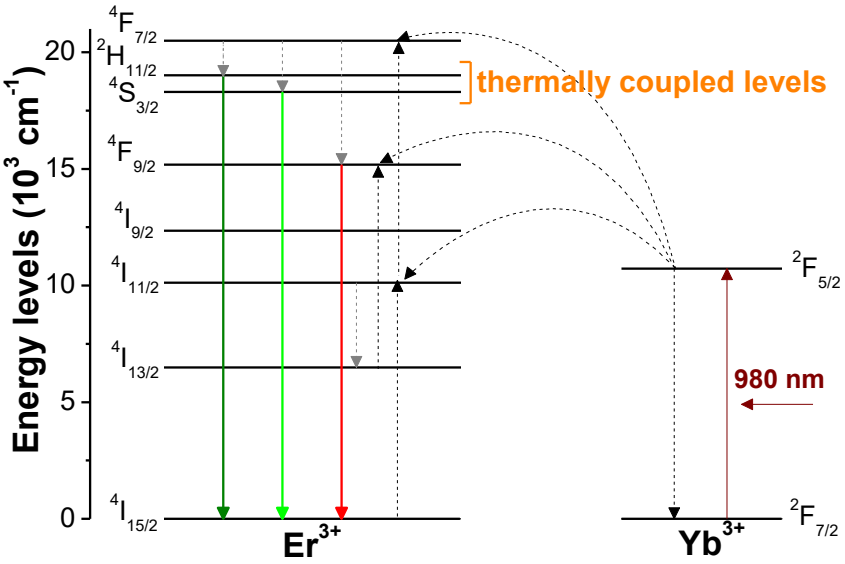

Figure 5.5. Schematic energy level diagram of Yb^{3+} and Er^{3+} and the mechanism of upconversion emissions under 980 nm laser excitation.

The upconversion emission spectra ($\lambda_{exc.}$ 980 nm) measured as a function of temperature (20–70 °C) for α-UCNPs, β-UCNPs (in hexane) and β-UCNPs@SiO_2 (in water) are presented in Figure 5.6. As the temperature increases, the emission intensity at around 525 nm was observed to increase with respect to the emission at 550 nm, due to a thermally-driven population increase of the higher energy level ($^2H_{11/2}$), to the detriment of the lower-energy level ($^4S_{3/2}$), according to the Boltzmann's distribution (eq. (5.1)).

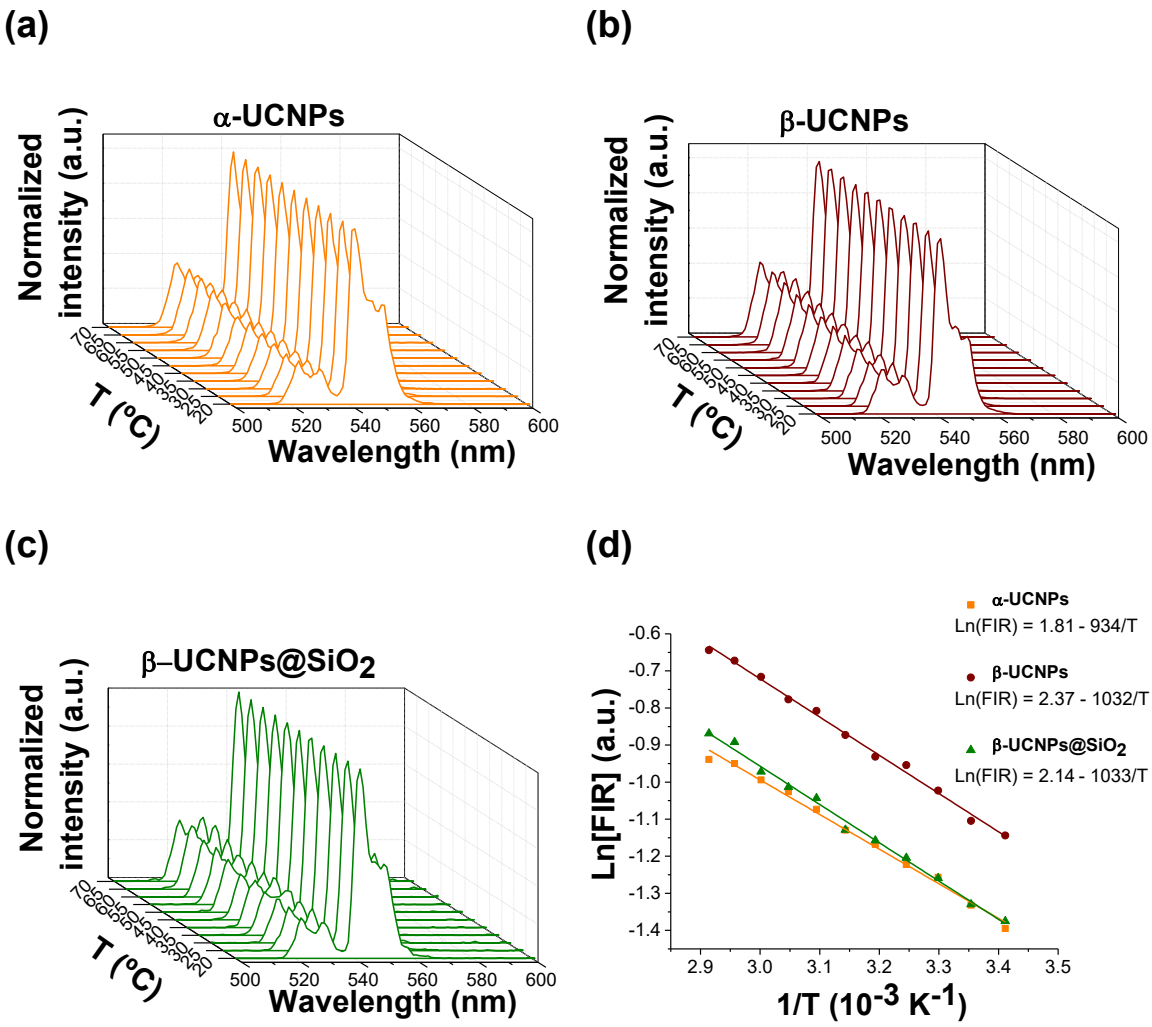

Figure 5.6. Upconversion emission spectra (λ_{exc}. 980 nm) at different temperatures (20–70 °C) of α-UCNPs (a), β-UCNPs (b), and β -UCNPs@SiO_2 (c). Boltzmann's plots (d).

The absolute thermal sensitivity (*S*) is the parameter that describes the quality of the obtained nanothermometers. *S* is defined as the rate at which the ratio of fluorescence intensities changes with the temperature and can be expressed as:

$$S = \frac{\partial(\mathrm{FIR})}{\partial T} = \mathrm{FIR}\left(\frac{\Delta E}{k_B T^2}\right), \tag{5.2}$$

in which $\Delta E/k_B$ is given by the slope of the Boltzmann's plot (Ln[FIR] *vs.* 1/*T*).[27] Figure 5.7 presents the thermal sensitivity at different temperatures for the obtained systems. *S* values increase with temperature,

ranging between 2.7 and 3.2, 3.8 and 4.6, and 3.0 and 3.7 × 10^{-3} K^{-1} for α-UCNPs, β-UCNPs and β-UCNPs@SiO_2, respectively. Those values are similar in range to those found in the literature for Yb^{3+}:Er^{3+} co-doped nanoparticles around the physiological temperature, *i.e.*, 2–4 × 10^{-3} K^{-1}.[22,27,44,45] The calculated thermal sensitivities suggest that the hexagonal phase $NaGdF_4$ is a better matrix for temperature sensing. Vetrone *et al.*[22] have found a *S* value of 2.2 × 10^{-3} K^{-1}.at 37 °C for the cubic phase $NaYF_4$:Yb^{3+}:Er^{3+} (18 nm particle size), which is lower than the *S* value of 3.6 × 10^{-3} K^{-1}.obtained for hexagonal phase $NaGdF_4$:Yb^{3+}:Er^{3+} at 35 °C (26 nm particle diameter) reported by Hemmer *et al.*[27] The temperature dependent upconversion luminescence of $NaYF_4$:Yb^{3+}:Er^{3+} UCNPs with different crystalline phases was studied by Yu *et al.*[46] For the β-phase, the FIR increased solely with temperature, but they indicated that for the α-phase the FIR demonstrated a complex and obscure temperature dependence. A temperature increase may not only induce an increase in the population of the $^2H_{11/2}$ energy level, but also a thermal quenching effect, which may be more pronounced for the cubic phase. The upconversion emission intensity is lower in an aqueous environment (in the case of β-UCNPs@SiO_2), due to the high energy vibrational modes of water molecules that increase multiphonon relaxation. However, surface modification *via* silanization offers partial protection against OH vibrations.[47] The quenching of luminescence related to the crystalline phase or to the presence of OH groups could lead to the deactivation of energy levels, and to the quenching of the upconversion emission intensity. These relaxation pathways could favor the population of the $^4S_{3/2}$ state at the expense of $^2H_{11/2}$ and thus negatively impact the thermal sensitivity.

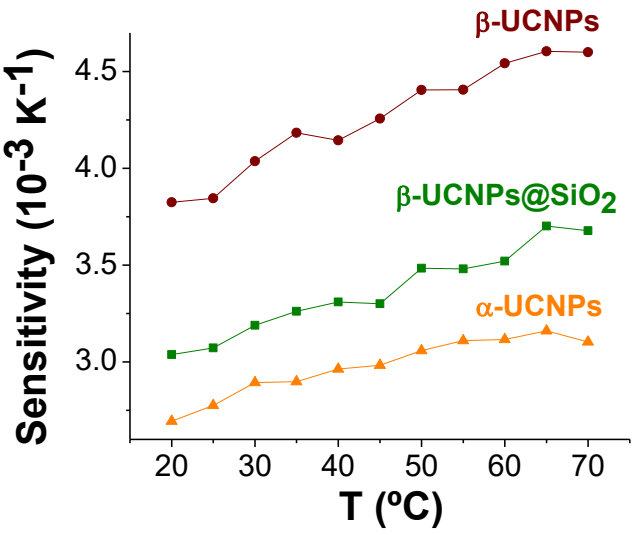

Figure 5.7. Thermal sensitivities of α-UCNPs, β-UCNPs and silica-coated β -UCNPs.

5.3.4. Photothermal effect

The surface of UCNPs@SiO_2 was functionalized with amine groups for further preparation of the multifunctional heater/thermometer system, AuNSs@UCNPs. Positive zeta potentials (+23.8 ± 0.6 mV)

were measured for UCNPs@SiO_2 after amino functionalization. These particles were assembled on the gold nanoshells with negative zeta potentials (–19.9 ± 0.6 mV) through electrostatic attraction. Figure 5.8a shows a TEM image of a gold nanoshell (average size of 282.9 ± 9.2 nm) with UCNPs@SiO_2 well distributed on its surface. The extinction spectrum presented in Figure 5.8b shows the SPR of AuNSs covering the red and NIR regions and matching the excitation wavelength of upconversion luminescence, allowing the use of a single laser for the excitation of AuNSs@UCNPs.

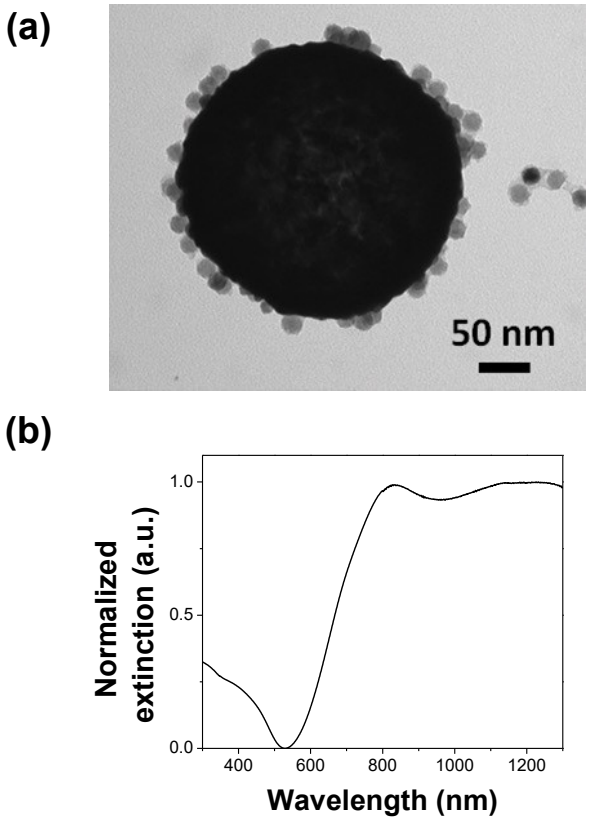

Figure 5.8. (a) TEM image and (b) extinction spectrum of AuNSs@UCNPs.

To study the photothermal properties of the obtained nanocomposites, a colloidal solution of AuNSs@UCNPs was irradiated with different laser powers to excite the SPR of Au and measure the upconversion emission spectra (Figure 5.9a). The measurements were also performed for UCNPs@SiO_2 without Au (Figure 5.9b). The thermal calibration curve obtained from the Boltzmann plot was used to estimate the temperature as a function of laser power (Figure 5.9c). In the absence of AuNSs, the temperature remains around 25 °C in accord with previous studies.[23,25,26] The calculated temperature values are around 40 °C for AuNSs@UCNPs in the temperature range of hyperthermia.[8] In previous studies on dual-nanoparticle systems for heating and thermometry, the local generation of heat was verified in a similar approach by monitoring Er^{3+} emission. Rohani *et al*.[25] showed a temperature increase with laser power for a glass substrate spin-coated with $NaGdF_4$:Yb^{3+}:Er^{3+} UCNPs and Au nanorods.

Debasu *et al*.[26] measured the temperature increase for powdered samples of $(Gd,Yb,Er)_2O_3$ nanorods and Au nanorods with 850 and 980 nm longitudinal SPR bands. Local heating was more efficient for SPR at 980 nm in resonance with laser excitation.

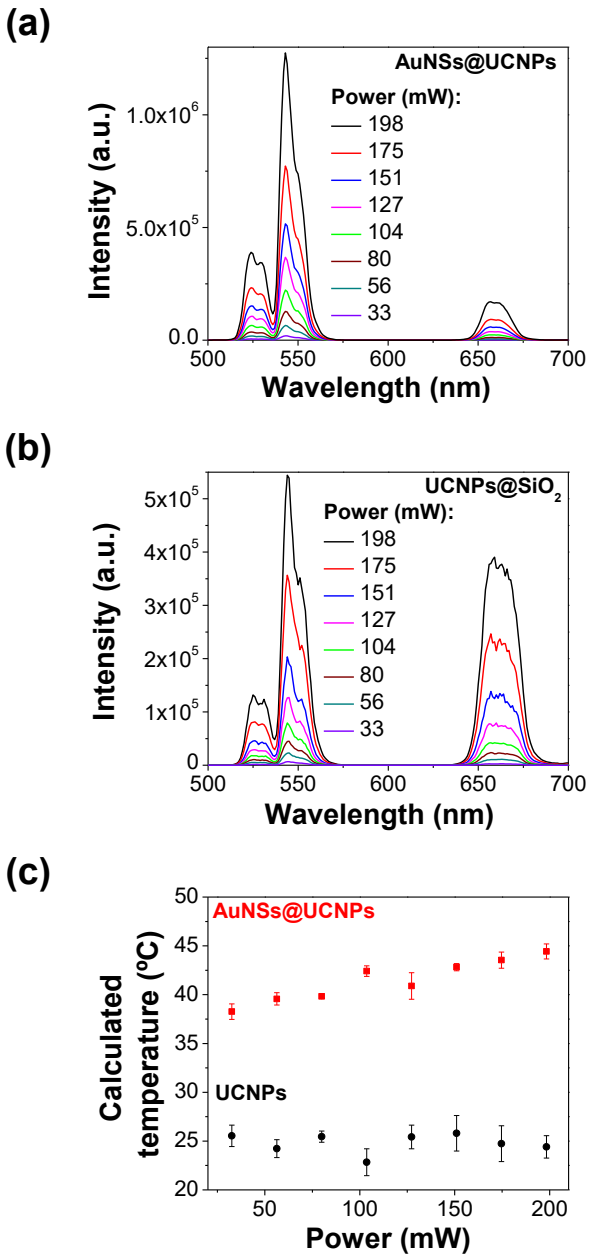

Figure 5.9. Upconversion emission spectra ($\lambda_{exc.}$ 980 nm) for different laser powers of AuNSs@UCNPs (a) and UCNPs@SiO_2 (b). Calculated temperature values (c).

The photothermal conversion efficiency (η) can be determined using the equation:

$$\eta = \frac{Q_{\text{output}}}{Q_{\text{input}}} \tag{5.3}$$

considering Q_{output} as the maximum temperature increase of 19.4 °C (from environmental temperature) for the laser pump power of 198.3 mW (Q_{input}). Thus, according to this, the efficiency is deduced to be 10.2 mW °C^{-1}. The present multifunctional system behaves as a heater and a temperature sensor under NIR excitation.

5.4. Conclusions

Monodisperse $NaGdF_4:Yb^{3+}:Er^{3+}$ upconversion nanocrystals were obtained in the hexagonal phase using a thermal decomposition method. The UCNPs in the hexagonal phase were shown to be more suitable for application as a temperature sensor than those in the cubic phase, due to their lower red-to-green emission ratio and higher thermal sensitivity. The hydrophobic oleate-capped nanocrystals were coated with a thin silica shell through a reverse microemulsion route to achieve water dispersibility. The core–shell UCNPs presented suitable properties for application as a temperature sensor operating in the vicinity of the physiological range revealing excellent linearity (R^2 > 0.99). We verified the heating capability of the nanocomposite containing the UCNPs and AuNSs by exciting the surface plasmon resonance and the emission of UCNPs was used as a means to measure the temperature in these nanocomposites. This investigation proposed a new system with potential to perform a controlled hyperthermia procedure.

References

1 GOTA, C.; OKABE, K.; FUNATSU, T.; HARADA, Y.; UCHIYAMA, S. Hydrophilic fluorescent nanogel thermometer for intracellular thermometry. **J. Am. Chem. Soc.**, v. 131, p. 2766–2767, 2009.

2 OKABE, K.; INADA, N.; GOTA, C.; HARADA, Y.; FUNATSU, T.; UCHIYAMA, S. Intracellular temperature mapping with a fluorescent polymeric thermometer and fluorescence lifetime imaging microscopy. **Nat. Commun.**, v. 3, p. 705, 2012.

3 ZOHAR, O.; IKEDA, M.; SHINAGAWA, H.; INOUE, H.; NAKAMURA, H.; ELBAUM, D.; ALKON, D. L.; YOSHIOKA, T. Thermal imaging of receptor-activated heat production in single cells. **Biophys. J.**, v. 74, p. 82–89, 1998.

4 MONTI, M.; BRANDT, L.; IKOMI-KUMM, J.; OLSSON, H. Microcalorimetric investigation of cell metabolism in tumour cells from patients with non-Hodgkin lymphoma (NHL). **Scand. J. Haematol.**, v. 36, p. 353–357, 1986.

5 OLESON, J. R.; DEWHIRST, M. W. Hyperthermia: an overview of current progress and problems. **Curr. Prob. Cancer**, v. 8, p. 1–62, 1983.

6 HAND, J. W. Physical techniques for delivering microwave energy to tissues. **Br. J. Cancer**, v. 5, p. 9–15, 1982.

7 WUST, P.; HILDEBRANDT, B.; SREENIVASA, G.; RAU, B.; GELLERMANN, J.; RIESS, H.; FELIX, R.; SCHLAG, P. M. Hyperthermia in combined treatment of cancer. **Lancet Oncol.**, v. 3, p. 487–497, 2002.

8 JAQUE, D.; MARTÍNEZ MAESTRO, L.; ROSAL, B. DEL; HARO-GONZALEZ, P.; BENAYAS, A.; PLAZA, J. L.; MARTÍN RODRÍGUEZ, E.; GARCÍA SOLÉ, J. Nanoparticles for photothermal therapies. **Nanoscale**, v. 6, p. 9494–9530, 2014.

9 PANKHURST, Q. A.; CONNOLLY, J.; K, J. S.; DOBSON, J. Applications of magnetic nanoparticles in biomedicine. **J. Phys. D: Appl. Phys.**, v. 36, p. R167–R181, 2003.

10 HUANG, X.; JAIN, P. K.; EL-SAYED, I. H.; EL-SAYED, M. A. Plasmonic photothermal therapy (PPTT) using gold nanoparticles. **Laser Med. Sci.**, v. 23, p. 217–228, 2008.

11 CHOI, J.; YANG, J.; JANG, E.; SUH, J.-S.; HUH, Y.-M.; LEE, K.; HAAM, S. Gold nanostructures as photothermal therapy agent for cancer. **Adv. Anticancer Agents Med. Chem.**, v. 11, p. 953–964, 2011.

12 MAESTRO, L. M.; HARO-GONZÁLEZ, P.; IGLESIAS-DE LA CRUZ, M. C.; SANZ-RODRÍGUEZ, F.; JUARRANZ, Á.; SOLÉ, J. G.; JAQUE, D. Fluorescent nanothermometers provide controlled plasmonic-mediated intracellular hyperthermia. **Nanomedicine**, v. 8, p. 379–88, 2013.

13 BRITES, C. D. S.; LIMA, P. P.; SILVA, N. J. O.; MILLÁN, A.; AMARAL, V. S.; PALACIO, F.; CARLOS, L. D. Thermometry at the nanoscale. **Nanoscale**, v. 4, p. 4799–4829, 2012.

14 NIGOGHOSSIAN, K.; MESSADDEQ, Y.; BOUDREAU, D.; RIBEIRO, S. J. L. UV and temperature-sensing based on $NaGdF_4$:Yb^{3+}:Er^{3+}@SiO_2–$Eu(tta)_3$. **ACS Omega**, v. 2, p. 2065–2071, 2017.

15 MENEZES, L. D. S.; de ARAÚJO, C. B. Optically detected thermal effects in rare-earth doped materials for host characterization, thermometric devices, nanothermometry and biothermometry. **J. Braz. Chem. Soc.**, v. 26, p. 2405–2417, 2015.

16 LIU, Q.; FENG, W.; LI, F. Water-soluble lanthanide upconversion nanophosphors: Synthesis and bioimaging applications in vivo. **Coord. Chem. Rev.**, v. 273–274, p. 100–110, 2014.

17 TU, D.; ZHENG, W.; LIU, Y.; ZHU, H.; CHEN, X. Luminescent biodetection based on lanthanide-doped inorganic nanoprobes. **Coord. Chem. Rev.**, v. 273–274, p. 13–29, 2014.

18 AUZEL, F. Upconversion and anti-stokes processes with f and d ions in solids. **Chem. Rev.**, v. 104, p. 139–173, 2004.

19 BARRETO, J. A.; O´MALLEY, W.; KUBEIL, M.; GRAHAM, B.; STEPHAN, H.; SPICCIA, L. Nanomaterials: applications in cancer imaging and therapy. **Adv. Mater.**, v. 23, p. H18-H40, 2011.

20 XU, C. T.; ZHAN, Q.; LIU, H.; SOMESFALEAN, G.; QIAN, J.; HE, S.; ANDERSSON-ENGELS, S. Upconverting nanoparticles for pre-clinical diffuse optical imaging, microscopy and sensing: Current trends and future challenges. **Laser Photonics Rev.**, v. 7, p. 663–697, 2013.

21 ZHAO, J.; JIN, D.; SCHARTNER, E. P.; LU, Y.; LIU, Y.; ZVYAGIN, A. V.; ZHANG, L.; DAWES, J. M.; XI, P.; PIPER, J. A.; GOLDYS, E. M.; MONRO, T. M. Single-nanocrystal sensitivity achieved by enhanced upconversion luminescence. **Nat. Nanotechnol.**, v. 8, p. 729–34, 2013.

22 VETRONE, F.; NACCACHE, R.; ZAMARRON, A.; SANZ-RODRIGUEZ, F.; MAESTRO, L. M.; RODRIGUEZ, E. M.; JAQUE, D.; SOLE, J. G.; CAPOBIANCO, J. A. Temperature sensing using fluorescent nanothermometers. **ACS Nano**, v. 4, n. 6, p. 3254–3258, 2010.

23 DEBASU, M. L.; ANANIAS, D.; PASTORIZA-SANTOS, I.; LIZ-MARZÁN, L. M.; ROCHA, J.; CARLOS, L. D. All-in-one optical heater-thermometer nanoplatform operative from 300 to 2000 K based on Er^{3+} emission and blackbody radiation. **Adv. Mater.**, v. 25, p. 4868–4874, 2013.

24 HUANG, Y.; ROSEI, F.; VETRONE, F. A single multifunctional nanoplatform based on upconversion luminescence and gold nanorods. **Nanoscale**, v. 7, p. 5178–5185, 2015.

25 ROHANI, S.; QUINTANILLA, M.; TUCCIO, S.; DE ANGELIS, F.; CANTELAR, E.; GOVOROV, A. O.; RAZZARI, L.; VETRONE, F. Enhanced luminescence, collective heating, and nanothermometry in an ensemble system composed of lanthanide-doped upconverting nanoparticles and gold nanorods**. Adv. Opt. Mater.**, v. 3, p. 1606–1613, 2015.

26 DEBASU, M. L.; BRITES, C. D.; BALABHADRA, S.; OLIVEIRA, H.; ROCHA, J.; CARLOS, L. D. Nanoplatforms for plasmon-induced heating and thermometry. **ChemNanoMat**, v. 2, p. 520–527, 2016.

27 HEMMER, E.; QUINTANILLA, M.; LÉGARÉ, F.; VETRONE, F. Temperature-induced energy transfer in dye-conjugated upconverting nanoparticles: a new candidate for nanothermometry. **Chem. Mater.**, v. 27, p. 235–244, 2015.

28 LI, Z.; ZHANG, Y.; JIANG, S. Multicolor core/shell-structured upconversion fluorescent nanoparticles. **Adv. Mater.**, v. 20, p. 4765–4769, 2008.

29 PHAM, TAN; JACKSON, JOSEPH B.; HALAS, NAOMI J.; LEE, T. R. Preparation and characterization of gold nanoshells coated with self-assembled monolayers. **Langmuir**, v. 18, p. 4915–4920, 2002.

30 STÖBER, W.; FINK, A.; BOHN, E. Controlled growth of monodisperse silica spheres in the micron size range. **J. Colloid Interface Sci.**, v. 26, p. 62–69, 1968.

31 WESTCOTT, S. L.; OLDENBURG, S. J.; LEE, T. R.; HALAS, N. J. Formation and adsorption of clusters of gold nanoparticles onto functionalized silica nanoparticle surfaces. **Langmuir**, v. 7463, p. 5396–5401, 1998.

32 DUFF, D. G.; BAIKER, A.; EDWARDS, P. P. A new hydrosol of gold clusters . 1 . Formation and particle size variation. **Langmuir**, v. 9, p. 2301-2309, 1993.

33 PARK, S. E.; PARK, M. Y.; HAN, P. K.; LEE, S. W. The effect of pH-adjusted gold colloids on the formation of gold clusters over APTMS-coated silica cores. **Bull. Korean Chem. Soc.**, v. 27, p. 1341–1345, 2006.

34 VISWANATHA, R.; SARMA, D. D. Growth of nanocrystals in solution. In: RAO, C. N. R.; MÜLLER, A.; CHEETHAM, A. K. (Eds.). **Nanomaterials chemistry: Recent developments and new directions.** Weinheim: John Wiley & Sons, 2007. chap. 4, p. 139–170.

35 NACCACHE, R. **Colloidal upconverting nanoparticle systems for integration in targeting, therapeutics and imaging applications**. 2012. Doctoral dissertation, Concordia University.

36 MAI, H. X.; ZHANG, Y. W.; SI, R.; YAN, Z. G.; SUN, L. D.; YOU, L. P.; YAN, C. H. High-quality sodium rare-earth fluoride nanocrystals: Controlled synthesis and optical properties. **J. Am. Chem. Soc.**, v. 128, p. 6426–6436, 2006.

37 ZENG, S.; REN, G.; XU, C.; YANG, Q. Modifying crystal phase, shape, size, optical and magnetic properties of monodispersed multifunctional NaYbF4 nanocrystals through lanthanide doping. **CrystEngComm**, v. 13, p. 4276-4281, 2011.

38 HU, Y.; SUN, Y.; LI, Y.; SUN, S.; HUO, J.; ZHAO, X. A facile synthesis of $NaYF_4$:Yb^{3+}/Er^{3+} nanoparticles with tunable multicolor upconversion luminescence properties for cell imaging. **RSC Adv.**, v. 4, p. 43653–43660, 2014.

39 LEE, J. S.; KIM, Y. J. The effects of preparation conditions on the structural and up-conversion properties of $NaYF_4$:Yb^{3+}, Er^{3+} nano powders. **Opt. Mater.**, v. 33, p. 1111–1115, 2011.

40 WILHELM, S.; KAISER, M.; WÜRTH, C.; HEILAND, J.; CARRILLO-CARRION, C.; MUHR, V.; WOLFBEIS, O. S.; PARAK, W. J.; RESCH-GENGER, U.; HIRSCH, T. Water dispersible upconverting nanoparticles: effects of surface modification on their luminescence and colloidal stability. **Nanoscale**, v. 7, p. 1403–1410, 2015.

41 LI, C.; HOU, Z.; DAI, Y.; YANG, D.; CHENG, Z.; MA, P;. LIN, J. A facile fabrication of upconversion luminescent and mesoporous core–shell structured β-$NaYF_4$:Yb^{3+},Er^{3+}@$mSiO_2$ nanocomposite spheres for anti-cancer drug delivery and cell imaging. **Biomater. Sci.**, v. 1, p. 213–223, 2013.

42 BRITES, C. D. S.; LIMA, P. P.; SILVA, N. J. O.; MILLÁN, A.; AMARAL, V. S.; PALACIO, F.; CARLOS, L. D. Lanthanide-based luminescent molecular thermometers. **New J. Chem.**, v. 35, p. 1177–1183, 2011.

43 ALENCAR, M. A. R. C.; MACIEL, G. S.; de ARAÚJO, C. B.; PATRA, A. Er^{3+}-doped $BaTiO_3$ nanocrystals for thermometry: Influence of nanoenvironment on the sensitivity of a fluorescence based temperature sensor. **Appl. Phys. Lett.**, v. 84, p. 4753–4755, 2004.

44 SINGH, S. K.; KUMAR, K.; RAI, S. B. Er^{3+}/Yb^{3+} codoped Gd_2O_3 nano-phosphor for optical thermometry. **Sens. Actuators, A**, v. 149, p. 16–20, 2009.

45 LI, D.; SHAO, Q.; DONG, Y.; JIANG, J. Thermal sensitivity and stability of $NaYF_4$:Yb^{3+},Er^{3+} upconversion nanowires, nanorods and nanoplates. **Mater. Lett.**, v. 110, p. 233–236, 2013.

46 YU, W.; XU, W.; SONG, H.; ZHANG, S. Temperature-dependent upconversion luminescence and dynamics of $NaYF_4$:Yb^{3+}/Er^{3+} nanocrystals: Influence of particle size and crystalline phase. **Dalton Trans.**, v. 43, p. 6139–6147, 2014.

47 ARPPE, R.; HYPPÄNEN, I.; PERÄLÄ, N.; PELTOMAA, R.; KAISER, M.; WÜRTH, C.; CHRIST, S.; RESCH-GENGER, U.; SCHÄFERLING, M.; SOUKKA, T. Quenching of the upconversion luminescence of $NaYF_4$:Yb^{3+},Er^{3+} and $NaYF_4$:Yb^{3+},Tm^{3+} nanophosphors by water: The role of the sensitizer Yb^{3+} in non-radiative relaxation. **Nanoscale**, v. 7, p. 11746–11757, 2015.

Chapter 6.

UV and temperature-sensing based on $NaGdF_4:Yb^{3+}:Er^{3+}@SiO_2–Eu(tta)_3$

Résumé

Un système multifonctionnel a été synthétisé pour être utilisé comme double capteur de lumière UV et de température. Des nanoparticules de $NaGdF_4:Yb^{3+}:Er^{3+}$ à conversion ascendante d'energie (UCNPs) ont été synthétisées et recouvertes avec une coquille de silice à laquelle un complexe d'europium(III) a été incorporé. La sythèse des UCNPs de $NaGdF_4:Yb^{3+}:Er^{3+}$ a été réalisé par décomposition thermique des précurseurs d'ions lanthanide en présence d'acide oléique. Afin d'obtenir une bonne dispersabilité dans l'eau, la surface hydrophobe recouvert d'oléate des UCNPs dans la phase hexagonale a été modifiée par un revêtement de silice au moyen d'un processus Stöber adapté pour une méthode de microémulsion inverse. Le complexe $Eu(tta)_3$ (tta-thénoyltrifluoreacetonate) a été préparé *in situ* dans la coquille de silice. Un nanothermomètre à double mode a été obtenu à partir du signal de fluorescence par la conversion ascendante du proche infrarouge au visible des ions Er^{3+} ainsi que l'émission par la conversion descendante excitée dans l'UV des ions Eu^{3+}. Les mesures ont été prises près de la plage de température physiologique (293–323 K) et montrent une excellente linéarité ($R^2 > 0,99$) et une sensibilité thermique relativement élevée ($\geq 1,5\% \cdot K^{-1}$). Le complexe $Eu(tta)_3$ présent dans la coquille de silice a été testé comme un capteur de lumière UV en raison de la dépendance de la luminescence de l'ion Eu^{3+} du temps d'exposition à la lumière UV.

Resumo

Um sistema multifuncional foi sintetizado para ser utilizado como um sensor duplo de luz UV e temperatura. Nanopartículas de $NaGdF_4:Yb^{3+}:Er^{3+}$ para conversão ascendente de energia (UCNPs) foram sintetizadas e recobertas com uma casca de sílica à qual um complexo de európio(III) foi incorporado. A síntese das UCNPs de $NaGdF_4:Yb^{3+}:Er^{3+}$ foi realizada por meio da decomposição térmica de precursores de íons lantanídeos na presença de ácido oleico. A fim de atingir uma boa dispersão em água, a superfície hidrofóbica recoberta por oleato das UCNPs na fase hexagonal foi modificada por um recobrimento de sílica por meio de um processo Stöber adaptado por um método de microemulsão reversa. O complexo $Eu(tta)_3$ (tta-tenoiltrifluoroacetonato) foi preparado *in situ* na casca de sílica. Um nanotermômetro de modo duplo foi obtido a partir do sinal de fluorescência de conversão ascendente do infravermelho próximo ao visível dos íons Er^{3+} juntamente com a emissão por conversão descendente excitada no UV do complexo de Eu^{3+}. As medidas foram realizadas próximo à faixa de temperatura fisiológica (293–323 K) revelando uma excelente linearidade ($R^2 > 0,99$) e uma sensibilidade térmica relativamente alta ($\geq 1,5\% \cdot K^{-1}$). O complexo de $Eu(tta)_3$ presente na casca de sílica foi testado como um sensor de luz UV pelo fato da sua luminescência depender do tempo de exposição à luz UV.

Abstract

A multifunctional nanosystem was synthesized to be used as a dual sensor of UV light and temperature. $NaGdF_4$:Yb^{3+}:Er^{3+} upconverting nanoparticles (UCNPs) were synthesized and coated with a silica shell to which a europium(III) complex was incorporated. The synthesis of $NaGdF_4$ UCNPs was performed *via* thermal decomposition of lanthanide ion fluoride precursors in the presence of oleic acid. To achieve sufficient water dispersibility, the surface of the hydrophobic oleate-capped UCNPs in the hexagonal phase was modified by a silica coating through a modified Stöber process through a reverse microemulsion method. An $Eu(tta)_3$ (tta-thenoyltrifluoroacetonate) complex was prepared in situ at the silica shell. A dual-mode nanothermometer was obtained from a near infrared to visible upconversion fluorescence signal of Er^{3+} ions together with UV-excited downshifting emission from the Eu^{3+} complex. Measurements were recorded near the physiological temperature range (293–323 K), revealing excellent linearity (R^2 > 0.99) and relatively high thermal sensitivities (≥1.5%·K^{-1}). The $Eu(tta)_3$ complex present in the silica shell was tested as the UV sensor because of the Eu^{3+} luminescence dependence on UV-light exposure time.

6.1. Introduction

The rapid advance in nanotechnology has enabled the development of materials that integrate multiple functions, each one related to their components that act synergistically. A large number of composite nanomaterials have been created, which exhibit excellent chemical, physical, and biological properties with strong potential in biomedicine,[1] catalysis,[2] sensors,[3] energy conversion,[4] and so forth. Incorporation of luminescent species in such materials gives rise to additional applications in photonics, medicine, sensing, and imaging as well. In fact, lanthanide-based materials possess special luminescence properties such as narrow photoluminescence peaks, tunable photostability, relatively high emission quantum yields and emission lines spanning the electromagnetic spectrum from the ultraviolet to the infrared region, allowing high technology applications.[5–8]

One interesting application of the luminescent properties of lanthanide ions consists of thermometry on the nanoscale because of a strongly temperature-dependent effect.[9–11] Temperature is a fundamental variable that governs diverse intracellular chemical and physical interactions in the life cycle of biological cells.[12] Measuring the temperature of cancer cells at the cellular level, for example, allows the optimization of therapeutic processes (*e.g.*, hyperthermal tumor treatment).[13,14] Another current interest in nanothermometry is monitoring temperature in micro- or nanoelectronics "hot spots".[15,16] Fundamental properties such as the instantaneous ballistic velocity of suspended Brownian nanocrystals have been measured with nanothermometers as well.[17] Temperature variations may induce different effects on the luminescence of lanthanides, including (i) redistribution of the electronic state population because of Boltzmann statistics, (ii) quenching mechanisms that result in decreasing emission intensity, and (iii) nonradiative transition because of electron-phonon interactions.[18]

Several dopant ions have been used in lanthanide-based thermometers. Er^{3+}- containing materials present a strong temperature dependence on the relative intensity of its two green luminescence bands. This effect is associated with the thermal equilibrium in the population of excited states $^2H_{11/2}$ and

$^4S_{3/2}$.[19] An interesting point relates to the fact that the green emission can be observed with excitation either in the UV or in the infrared region. In the latter case, the so-called upconversion emission is treated. It is a well-known feature observed for many different lanthanide ions, being used in several different fields.[20–22] Concerning the UV-excited downshifting emission of Eu^{3+} complexes with organic ligands, a temperature probe with a highly temperature-dependent emission is related to the thermal deactivation of the $^5D_0$ excited state.[23–26] Eu^{3+} complexes may also present an additional issue that is related to their reduced photostability under UV irradiation. Because UV light detection is of great interest in environmental and biological fields, among others, the low photostability may be well explored for UV dose sensing.[27–34] Therefore, dual-modal temperature sensors may be obtained from two active centers with different temperature-sensitive luminescence features. Such thermometers may combine two lanthanide ions.[35–37] The second probe may be an organic dye,[38] a quantum dot,[39] or a transition metal ion.[40–46]

Lanthanide-based upconversion nanoparticles (UCNPs) are a promising solution for biological systems as they can be excited in the near infrared (NIR) region within the biological transparency window and emit NIR photons or higher energy (visible) photons. High penetration depths and low autofluorescence are some of the unique advantages related to the use of low-energy NIR excitation photons compared with conventional luminescent nanomaterials, such as organic dyes and quantum dots, which require an excitation source in the UV–visible region.[47]

This work proposes a multifunctional nanoplatform that combines two independent luminescent probes. $NaGdF_4:Yb^{3+}:Er^{3+}@SiO_2–Eu(tta)_3$ nanoparticles were prepared as a temperature sensor in the vicinity of the biological range (293–323 K) and a UV-light detector.

6.2. Materials and methods

6.2.1. Materials

Lanthanide oxides (gadolinium oxide, ytterbium oxide and erbium oxide), europium(III) chloride hexahydrate, trifluoroacetic acid, sodium trifluoroacetate, oleic acid, 1-octadecene, IGEPAL CO-520, ammonium hydroxide (28–30%), tetraethyl orthosilicate (TEOS), and 2-thenoyltrifluoroacetone (tta) were all purchased from Sigma (Sigma-Aldrich Co., St. Louis, MO, USA).

6.2.2. Synthesis of $Yb^{3+}:Er^{3+}$ co-doped $NaGdF_4$ UCNPs

The synthesis of colloidal $NaGdF_4$ upconverting nanoparticles doped with the ions $Yb^{3+}:Er^{3+}$ was performed *via* thermal decomposition of fluoride precursors of lanthanide ions. The method described previously by Hemmer *et al.*[48] is a two-pot synthesis. In the first step of the synthesis, the lanthanide trifluoroacetate precursor was prepared. A 10 mL mixture of trifluoroacetic acid and water (1:1) was added to a 50 mL three-neck round bottom flask containing gadolinium oxide (353.4 mg, 0.975 mmol), ytterbium oxide (98.5 mg, 0.250 mmol), and erbium oxide (9.6 mg, 0.025 mmol) to obtain a molar ratio of Gd:Yb:Er =

78:20:2. The solution was refluxed at 353 K for 12 h until a clear solution was obtained. The temperature was then lowered to 333 K, and the flask was opened to let water and trifluoroacetic acid evaporate to dryness for 5 h. In the second step, 340 mg of sodium trifluoroacetate was added to the flask in which the precursor lanthanide trifluoroacetate was previously prepared, followed by the addition of 7.5 mL each of oleic acid and 1-octadecene. In a second flask (a three-neck round bottom flask of 100 mL), 12.5 mL each of oleic acid and 1-octadecene were added. The flasks were connected to a Schlenk line to remove moisture and oxygen for 30 min at 398 K under vacuum and magnetic stirring. Subsequently, the flask containing oleic acid and 1-octadecene was heated to 583 K under argon flow at a heating rate of 283 K/min. A few minutes after reaching this temperature, the precursor solution at 398 K was collected with a glass syringe and injected dropwise to the reaction vessel. A pump system was used at an injection rate of 1.5 mL min^{-1}. The solution was maintained at 583 K for a further 60 min under stirring and argon flow. After this period, the heating source was removed. When the solution reached room temperature, the obtained nanoparticles were precipitated by the addition of ethanol and centrifuged at 5350 RCF for 10 min. The nanoparticles were washed twice by dispersing in hexane, followed by precipitation with ethanol (1:5 v/v), and then recovered using centrifugation. The resultant oleate-capped $NaGdF_4:Yb^{3+}:Er^{3+}$ nanoparticles were finally redispersed in hexane for further characterizations.

6.2.3. Silica coating of $NaGdF_4:Yb^{3+}:Er^{3+}$ UCNPs

The obtained UCNPs were coated with a silica shell using a reverse microemulsion method.[49] First, 32 mg of UCNPs were dispersed in 10 mL of cyclohexane, and then 0.4 g of the surfactant IGEPAL CO-520 was added. After 10 min of stirring, 1.6 g of IGEPAL CO-520 and 80 µL of ammonium hydroxide were added to form a water-in-oil microemulsion. The emulsion was sonicated for 30 min. TEOS (40 µL) was then added and the solution was stirred at 300 rpm for 48 h. The nanoparticles were precipitated by adding acetone and washed twice with ethanol/water (1:1). Centrifugation was performed to recover the particles at 1590 RCF for 20 min. The UCNP core–silica shell ($UCNPs@SiO_2$) was finally stored in water.

6.2.4. Preparation of $NaGdF_4:Yb^{3+}:Er^{3+}@SiO_2–Eu(tta)_3$

First, europium was incorporated in the silica shell by adding europium(III) chloride hexahydrate solution in ethanol (1.5 mL, 20 mM) to $UCNPs@SiO_2$ (10 mg). The mixture was placed in an ultrasonic bath for 1 h and then 24 h under stirring in a vortex mixer. The nanoparticles were separated using centrifugation (1590 RCF/20 min). Afterward, the ligand tta was added in a 3:1 molar ratio tta/Eu. An ethanolic tta solution (1.5 mL, 60 mM) was added to the recovered particles and then dispersed using ultrasound followed by the addition of ammonia solution (75 µL). Stirring was continued for 24 h in a thermomixer (Eppendorf) at 800 rpm and 281 K. The particles were centrifuged (1590 RCF/20 min) and washed once with ethanol and once with hexane and finally suspended in ethanol (1.5 mL).

6.2.5. Characterization

A Tecnai G2 Spirit BioTwin (120 kV) transmission electron microscope (TEM) was used to analyze the particle size and structural morphology. The crystal phase of the UCNPs was investigated by X-ray diffraction (XRD) using a Siemens D5000 Kristalloflex diffractometer using nickel-filtered Cu Kα radiation. The processing software was JADE version 2.1 coupled with the JCPDS (Joint Committee on Powder Diffraction Standards) database of ICDD (International Centre for Diffraction Data) 2001 version. UV-excited visible photoluminescence and NIR-excited upconversion emission spectra were measured using a FluoroLog-3 spectrofluorimeter (model 322) from HORIBA Jobin Yvon. A Xenon lamp and an external 980 nm continuous wave diode laser JDS Uniphase (model S26-7602-340) were used as excitation sources. The excitation power densities at the sample position were estimated by using a power meter (Newport 2935-C). To obtain the thermal calibration curves, the emission spectra were measured at different temperatures in a Peltier-based temperature-controlled cuvette holder coupled to the fluorometer. A period of 10 min was given to allow the temperature to stabilize. For upconversion emission spectra measured at different temperatures, the laser power at the sample position was 81 mW. The calibration measurements for the UV light sensor were recorded at room temperature with a power density of 1.35 mW/cm^2.

6.3. Results and discussion

UCNPs were obtained as oleate-capped $NaGdF_4$:Yb^{3+}:Er^{3+} *via* thermal decomposition of lanthanide trifluoroacetate. TEM images of $NaGdF_4$:Yb^{3+}:Er^{3+} (Figure 6.1a) show that monodisperse nanocrystals (size 26.2 ± 1.7 nm) with hexagon-shaped morphology were obtained. The oleate-capped UCNPs are dispersible only in nonpolar solvents, such as hexane. The surface modification by a silica coating rendered the particles dispersible in water, which is important for biological applications. Additionally, silica is known to be highly stable, biocompatible, and optically transparent and to present abundant Si–OH active bonds available for surface functionalization; moreover, depending on the preparation method, high pore volumes may be obtained where different species may be stored.[50] TEM images of silica-coated UCNPs (Figure 6.1b) show a thin (approximately 7 nm thick) and uniform silica shell at the nanocrystal surface. An XRD pattern of oleate-capped $NaGdF_4$:Yb^{3+}:Er^{3+} and their corresponding phase reference graph of $NaGdF_4$ are presented in Figure 6.1c. The pattern is in accordance with the hexagonal phase (JCPDS file 27-0699), which is well known for its higher upconversion efficiency versus the cubic phase.[51] Figure 6.1d shows the upconversion emission spectrum (λ_{exc} 980 nm) of silica coated UCNPs in water at two different temperatures (293 and 323 K). The bands observed in the spectral regions of 510–536 and 536–575 nm correspond to the Er^{3+} transitions $^2H_{11/2} \rightarrow {}^4I_{15/2}$ and $^4S_{3/2} \rightarrow {}^4I_{15/2}$, respectively. As the temperature increases, the relative emission intensity at approximately 523 nm was observed to increase with respect to the emission at 543 nm because of a

thermally driven population increase in the higher energy level ($^2H_{11/2}$), to the detriment of the lower energy level ($^4S_{3/2}$). This effect is in accordance with the Boltzmann distribution as defined by eq. (6.1):

$$\mathrm{FIR} = \frac{I_{523}}{I_{543}} = C\exp\left(-\frac{\Delta E}{k_B T}\right) \tag{6.1}$$

where FIR is the fluorescence intensity ratio between the integrated intensities of the emission bands at 523 and 543 nm, represented by I_{523} and I_{543}, respectively; C is a constant that depends on the degeneracies and spontaneous emission rates of the emitting states and photon energies; and ΔE is the energy gap between the two excited states.

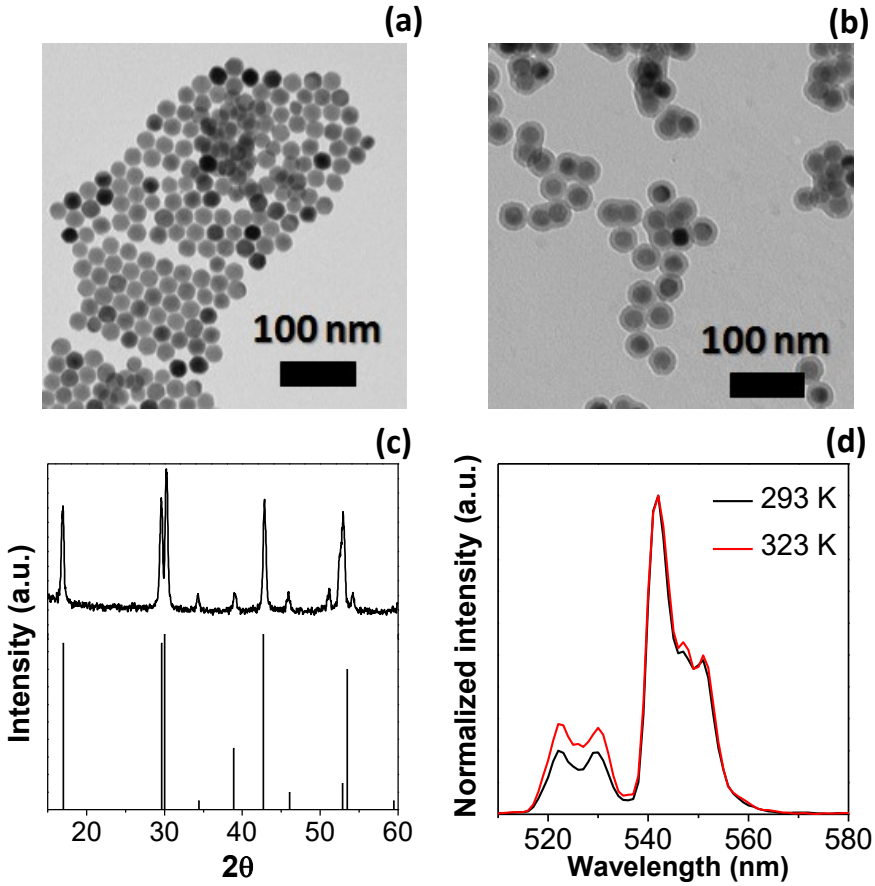

Figure 6.1. TEM images of (a) UCNPs and (b) UCNPs@SiO_2. (c) X-ray diffraction pattern and reference diffraction peaks corresponding to hexagonal $NaGdF_4$ (JCPDS file 27-0699). (d) Upconversion emission spectra (λ_{exc} 980 nm) at different temperatures (293 and 323 K) of UCNPs@SiO_2.

Figure 6.2 shows the photoluminescence excitation spectrum (PLE- Figure 6.2a) and photoluminescence emission spectrum (PL- Figure 6.2b) obtained for $NaGdF_4$:Yb^{3+}:Er^{3+}@SiO_2–$Eu(tta)_3$ nanoparticles. Two spectra of the well-known complex $[Eu(tta)_3(H_2O)_2]$ and the compound $[Eu(tta)_3$-U] (U

stands for an ureasil organic-inorganic hybrid host) adapted from Molina *et al.*[52] are also shown for comparison purposes. The broad excitation band (with maximum at 352 nm) covering the region of the UV-A (400–315 nm) and UV-B (315–280 nm) in PLE spectra accounts for the antenna effect because of the presence of tta ligands. Similarities in spectra allow us to propose that the $Eu(tta)_3$ compound is formed at the silica nanoshell of the new nanoparticles. As already mentioned, the strong UV absorption cross-section and efficient energy transfer make these Eu^{3+} complexes strong red light emitters. The well-known PL spectrum obtained for $[Eu(tta)_3(H_2O)_2]$ shows emission arising mainly from the Eu^{3+} $^5D_0$ to the ^7F_J manifold (J = 0, 1, 2, 3, 4), with the $^5D_0 \rightarrow {}^7F_2$ dominating the general intensity. When incorporated either in the organic–inorganic hybrid studied before or in the silica nanoshell of the present nanoparticles, broadening is observed because of the inhomogeneous distribution of sites in the two hosts.

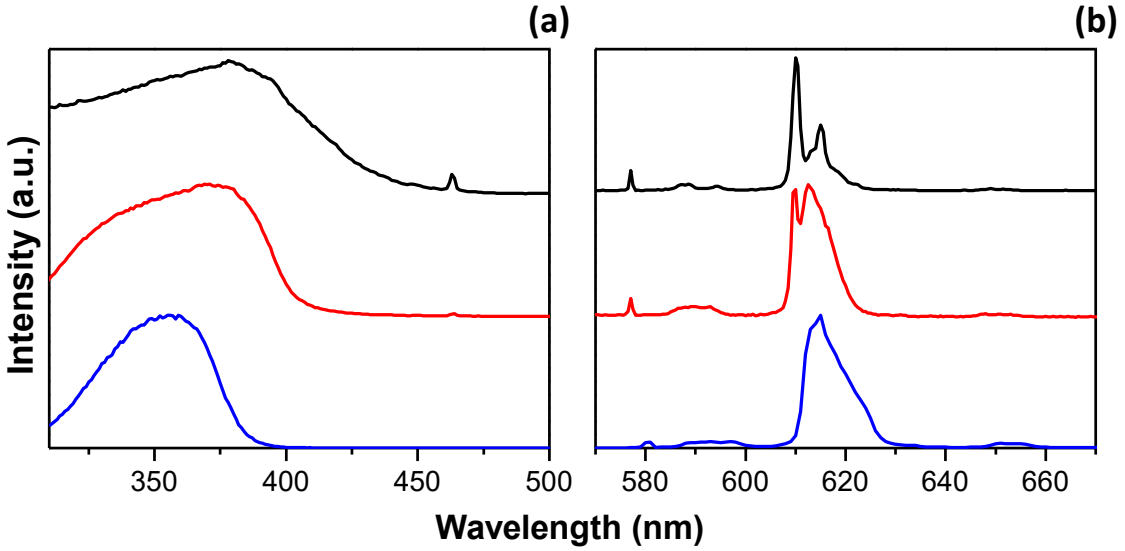

Figure 6.2. (a) Excitation (λ_{em} 615 nm) and (b) emission spectra for the complex $[Eu(tta)_3(H_2O)_2]$ (black), the compound [$Eu(tta)_3$–host] (red), and UCNPs@SiO_2-$Eu(tta)_3$ (blue). Spectra of $[Eu(tta)_3(H_2O)_2]$ and [$Eu(tta)_3$–host] were adapted from Molina *et al.*[52]

The drawback that could hinder the practical application of these luminophores refers to low photostability of the β-diketonates under UV light.[27] However, one can take in advantage that property that can be useful for application as a UV sensor after exposure to sunlight.

Figure 6.3a shows nanoparticle emission spectra obtained in the temperature range of 293–323 K under UV irradiation. The inset shows a photograph of the cuvette under UV illumination. A decrease in the Eu^{3+} emission intensity is observed with the increase in temperature because of a competition between emission and nonradiative energy transfer from the Eu^{3+} ion to the ligand (Figure 6.3a). As mentioned in the Introduction of this chapter (section 5.1) the utilization of the Eu^{3+}/tta species in temperature measurements based on intensity changes is well known.[23–26] Figure 6.3b shows the upconversion spectra in the same temperature range. The inset shows a photograph of the cuvette under 980 nm illumination. Here, again, the temperature-dependent variation of the emission lines can clearly be

observed. Figures 6.3c,d show the linear correlations that can be obtained for both Eu^{3+} (λ_{exc} 352 nm, R^2 = 0.99965) and Er^{3+} (λ_{exc} 980 nm, R^2 = 0.99776) emission bands upon temperature variations. The integration ranges used to compute the integrated areas are: 510–536 and 536–565 nm for Er^{3+} emissions and 603–643 nm for Eu^{3+} emission. For each temperature, the average of five measurements were calculated; error bars in the plots represent standard deviation. A dual-mode temperature sensor is therefore proposed here. The energy gap between the $^2H_{11/2}$ and $^4S_{3/2}$ states of Er^{3+} was estimated from the slope of Boltzmann plot (Figure 6.3d), which gives the parameter $\Delta E/k_B$ (eq. (6.1)). The value calculated from the slope (724 cm^{-1}) is similar to the energy difference between the barycenters of the emission bands (694 cm^{-1}) within the experimental resolution used in obtaining the spectra (1 nm). This ΔE value for Er^{3+} in different host materials ranges from 700 to 800 cm^{-1}.[14,53]

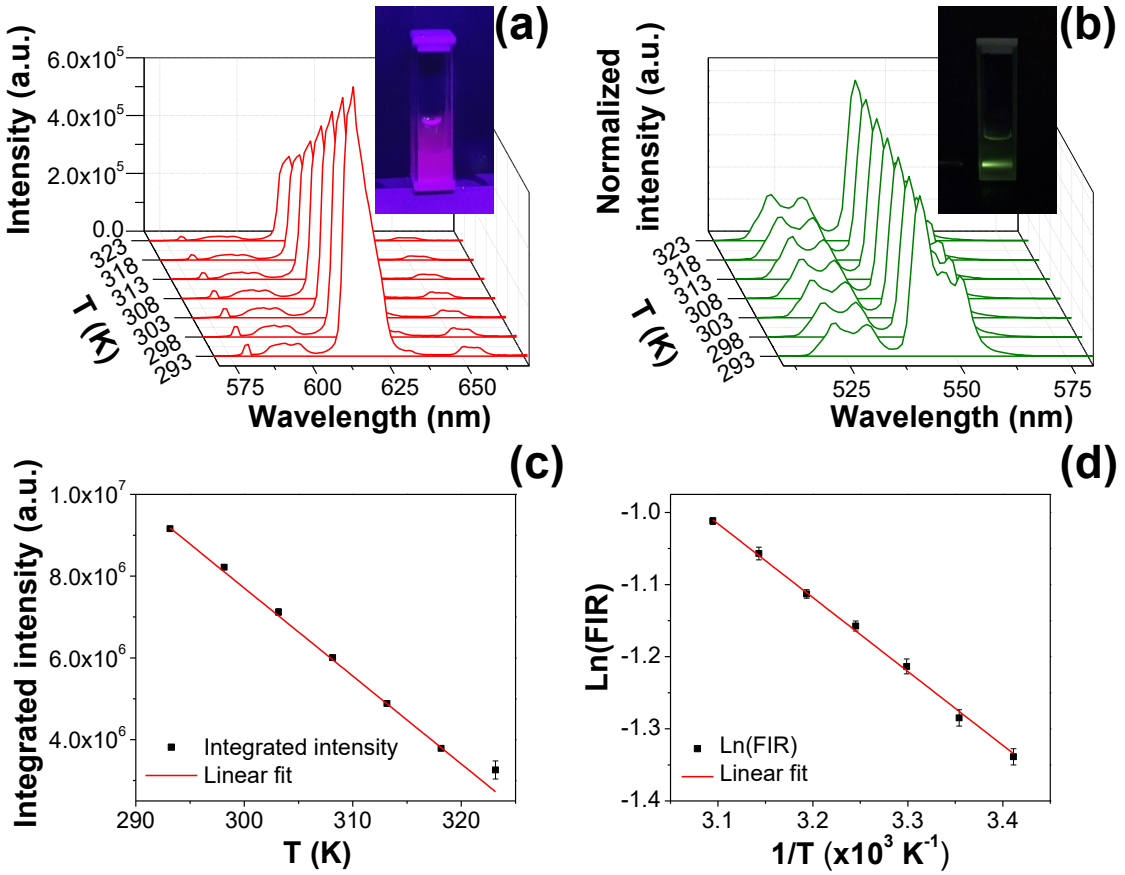

Figure. 6.3. Emission spectra of UCNPs@SiO_2–$Eu(tta)_3$ at different temperatures (293–323 K): under (a) UV and (b) NIR excitation. Insets: Corresponding luminescent photographs. Thermal calibration curves: (c) fluorescence intensity (integrated area) vs temperature (λ_{exc} 352 nm) and (d) ln(FIR) vs inverse temperature (λ_{exc} 980 nm).

The thermometric performance in the calibration temperature range was evaluated by analyzing several metric parameters. Table 6.1 presents the calibration parameters of the dual-mode thermometer under UV and NIR excitation. The calibration linearity was evaluated using the regression coefficient (R^2),

which was larger than 0.99. Temperature uncertainty (∂T), the smallest temperature change that can be detected in a given measurement, was determined from temperature readouts performed at different reference temperatures (displayed by the Peltier-based temperature controller). Temperature values were calculated from the calibration curves. The standard deviation of the resultant temperature is the experimental ∂T of the luminescent thermometer. Repeatability refers to the variability between measurements. High repeatability was observed for both probes, as the relative standard deviations (RSD) among measurements values were found to be lower than 0.3%.

In addition, the accuracy was estimated to evaluate the performance of the proposed nanothermometer. For each temperature, the average value for five replicate measurements was calculated and then compared with the reference temperature. The linear function between the real and the calculated temperature revealed excellent linearity (R^2 > 0.99), indicating the closeness between the measured value and the true value as shown in the Figure 6.4.

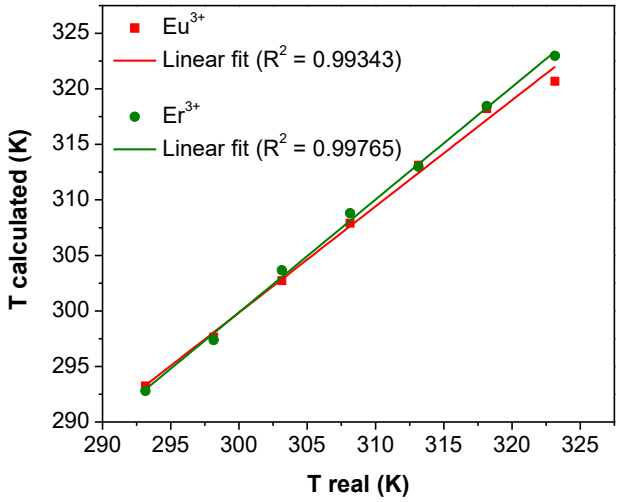

Figure 6.4. Linear function between real and calculated temperature for Er^{3+}- and Eu^{3+}-based thermometers.

The relative thermal sensitivity (S_r) is the parameter that describes the performance of a luminescent thermometer and allows the comparison of different types of thermometers.[9] S_r gives the variation of the experimental parameter (Q) per degree of temperature, which corresponds to (i) the FIR, for the ratiometric thermometer and (ii) the integrated intensity for the nonratiometric thermometer. S_r can be expressed as eq. (6.2):

$$S_r = \frac{(\partial Q / \partial T)}{Q} \qquad (6.2)$$

S_r values were estimated from the calibration data (Figures 6.3c,d). The relative sensitivity at 303 K was 2.67%·K^{-1} for the Eu^{3+} emission and 1.48%·K^{-1} for the Er^{3+} emission. Therefore, both techniques present high relative thermal sensitivities (> 1%·K^{-1}).[54]

Table 6.1. Calibration parameters of the dual-mode thermometer under UV and NIR excitations.

parameter	λ_{exc} 352 nm	λ_{exc} 980
slope	-2.15×10^5 ($\pm 1.65 \times 10^3$)	2.16 (±0.06)
intercept	7.23×10^7 ($\pm 5.04 \times 10^5$)	−1023.83 (±19.80)
regression coefficient (R^2)	0.99965	0.99776
uncertainty (∂T)	0.06 K	0.47 K
repeatability (RSD)	0.32%	0.33%
relative sensitivity (S_r) at 303 K	2.67%·K^{-1}	1.48%·K^{-1}

The dependence of S_r on temperature is presented in Figure 6.5. The variation is larger for the Eu^{3+} system. The sensors are considered to be better when the variation of sensitivity in all the range is low. The plot also shows that the Yb^{3+}/Er^{3+} system is less subject to variations in the temperature range considered.

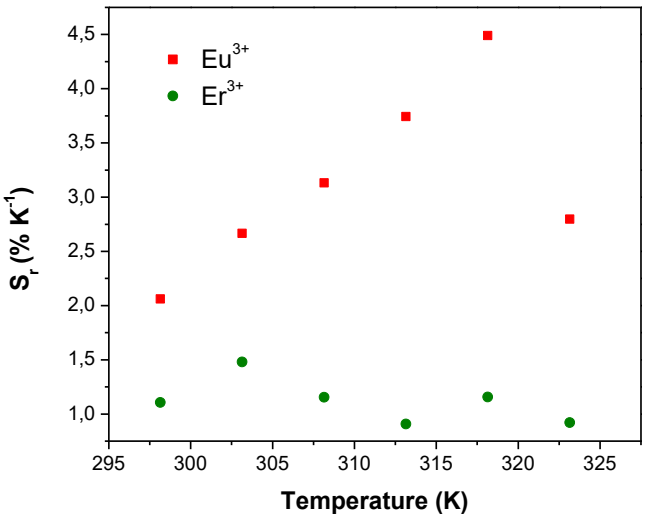

Figure 6.5. Relative thermal sensitivity (S_r) as a function of temperature for Er^{3+}/Yb^{3+} system (green) and for Eu(tta) system (red).

Tables 6.2 and 6.3 display the maximum values of relative sensitivities at around room temperature for the obtained thermometers and systems found in the literature. The S_r of the two sensors (Er^{3+}- and Eu^{3+}-based) is of the order of results from literature. The fluoride host and the β-diketonates are well known materials and no important difference should be expected.

Table 6.2. Maximum relative thermal sensitivity of Yb^{3+}:Er^{3+} doped UCNPs.

material	S_r (%·K^{-1})	reference
$NaGdF_4$:Yb^{3+}:Er^{3+}	1.48	this work
$NaYF_4$:Yb^{3+}:Er^{3+}	1.14	Vetrone *et al*. 2010[55]
Gd_2O_3:Yb^{3+}:Er^{3+}	1.00	Debasu *et al*., 2013[53]
Gd_2O_3:Yb^{3+}:Er^{3+}	0.80	Singh *et al*., 2009[56]

Table 6.3. Maximum relative thermal sensitivity of Eu^{3+}-based thermometers.

material	S_r (%·K^{-1})	reference
UCNPs@SiO_2-Eu(tta)$_3$	4.49	this work
Eu(tta)$_3$ in an acridone–polystyrene conjugate	0.80	Borisov *et al*., 2012[57]
Eu complexes with tta and other β-diketonate ligands in a poly(vinyl methyl ketone) film and in poly- (tert-butyl styrene) microparticles	0.97	Borisov *et al*., 2006[58]
Eu(TTA)$_3$Phen complex	3.67	Shahi *et al*., 2015[27]

A possible heating effect was investigated by measuring emission as a function of laser power (as shown in Figure 6.6). The calculated temperature 298.0 ± 1.0 K (which refers to the localized temperature on the UCNPs surface) and reference temperature 297.1 ± 0.4 K (displayed by the Peltier-based temperature controller) was close to room temperature and remained constant with pumping power increment.

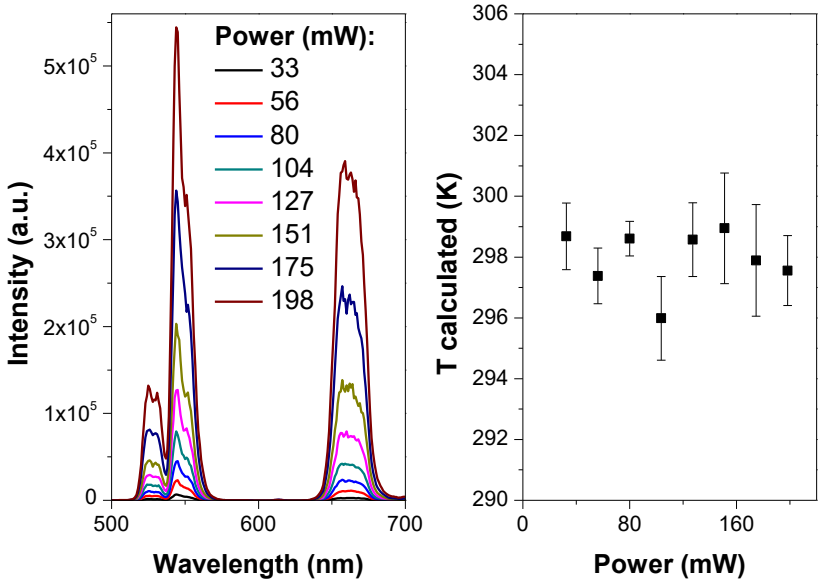

Figure 6.6. Upconversion emission spectra ($\lambda_{exc.}$ 980 nm) and calculated temperature values at different laser powers.

To further investigate the behavior of $NaGdF_4:Yb^{3+}:Er^{3+}@SiO_2–Eu(tta)_3$ nanoparticles under UV-light exposure (λ = 352 nm, with a power density of 1.35 mW/cm^2), emission spectra were measured at room temperature (Figure 6.7a) and 980 nm after different periods of exposure to UV light. The Eu^{3+} emission intensity at 615 nm (integrated area) decay with exposure time is presented in Figure 6.7b. Er^{3+}emission intensities at approximately 523 and 543 nm are also represented in Figure 6.7b. They remained constant, showing that the upconversion thermometer was not affected by UV-light irradiation. The ratio between the Eu^{3+} and Er^{3+} emission intensities presents an exponential decay (Figure 6.7b) with exposure time (R^2 = 0.98294). The ratio of the Eu^{3+} downshifting emission intensity to the upconverted emission intensity is therefore sensitive to the UV exposure dose.

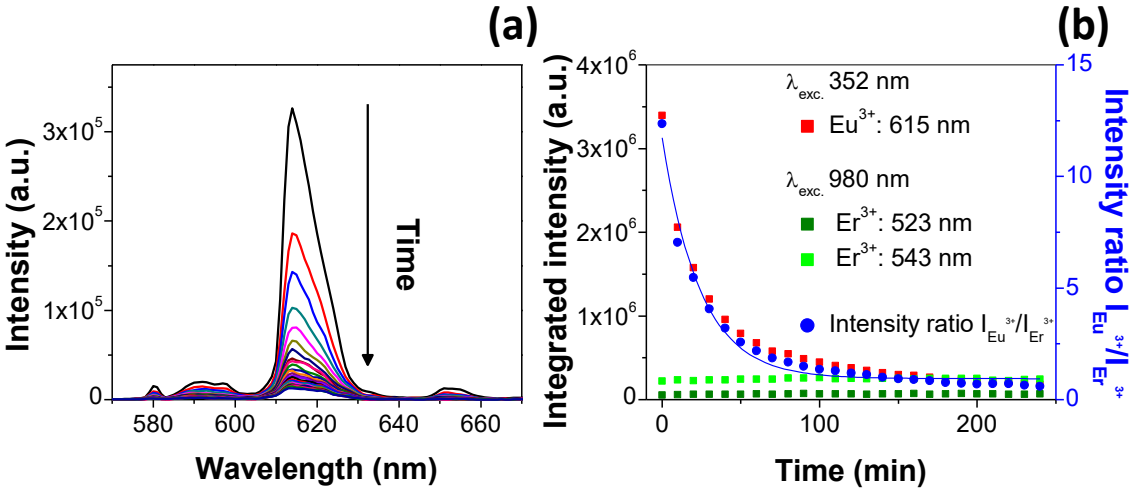

Figure 6.7. (a) Emission spectra (λ_{exc} 352 nm) of $UCNPs@SiO_2–Eu(tta)_3$ after different periods of exposure to UV light. (b) Fluorescence intensity (integrated area) under UV (352 nm) and NIR (980 nm) excitation and fluorescence intensity ratio between Eu^{3+} and Er^{3+} emissions vs time (the solid line represents the exponential fit curve).

6.4. Conclusions

$NaGdF_4:Yb^{3+}:Er^{3+}$ upconverting nanocrystals were obtained in the hexagonal phase by using the thermal decomposition method. The hydrophobic oleate-capped nanocrystals were coated with a thin silica shell through a reverse microemulsion route to achieve water dispersibility. The silica shell was also useful as a matrix for the incorporation of the europium(III)–tta complex. Thermal dependences of the Eu^{3+} and Er^{3+} luminescence were investigated under ultraviolet and infrared excitations. The optical thermometers so obtained presented suitable properties for use as a temperature sensor close to the physiological range (293–323 K) with excellent linearity (R^2 > 0.99). The ability to detect temperature was estimated by the calculation of thermal sensitivity. Both systems presented high thermal sensitivities

(>1.5%·K^{-1}). In addition, the europium(III) complex incorporated in the silica shell of UCNPs was found to be sensitive to ultraviolet light, which leads to its application as a UV-light sensor with no influence on the thermometer operation based on the upconversion emission. The results presented in this work stimulate the study of multifunctional materials for sensing applications based on lanthanide luminescence. The material shows potential for application in light activated therapies, such as photodynamic therapy (PDT) and photothermal therapy (PTT). These therapies typically require UV or blue light for excitation. The control of light dose released to the tissue is of great importance in these therapeutic procedures to avoid photodamage to the surroundings. Moreover, as temperature is a fundamental parameter in events that occur in cells, the thermometer function is useful to guide such therapeutic processes (PDT and PTT) synergistically with the UV dosimeter.

References

1 YIU, H. H. P.; NIU, H.-J.; BIERMANS, E.; VAN TENDELOO, G.; ROSSEINSKY, M. J. Designed multifunctional nanocomposites for biomedical applications. **Adv. Funct. Mater.**, v. 20, p. 1599–1609, 2010.

2 DENG, Y.; CAI, Y.; SUN, Z.; LIU, J.; LIU, C.; WEI, J.; LI, W.; LIU, C.; WANG, Y.; ZHAO, D. Multifunctional mesoporous composite microspheres with well-designed nanostructure: a highly integrated catalyst system. **J. Am. Chem. Soc.**, v. 132, p. 8466–8473, 2010.

3 GUO, S.; DONG, S. Metal nanomaterial-based self-assembly: development, electrochemical sensing and SERS applications. **J. Mater. Chem.**, v. 21, p. 16704–16716, 2011.

4 ROLISON, D. R.; LONG, J. W.; LYTLE, J. C.; FISCHER, A. E.; RHODES, C, P.; MCEVOY, T. M.; BOURG, M. E.; LUBERS, A. M. Multifunctional 3D nanoarchitectures for energy storage and conversion. **Chem. Soc. Rev.**, v. 38, p. 226–252, 2009.

5 RIBEIRO, S. J. L.; DOS SANTOS, M. V.; SILVA, R. R.; PECORARO, E.; GONÇALVES, R. R.; CAIUT, J. M. A. Optical properties of luminescent materials. In: LEVY, D., ZAYAT, M. (Eds.). **The sol-gel handobook, synthesis, characterization and applications**. Weinheim: Wiley-VCH Verlag GmbH & Co. KGaA, 2015. v. 2, p. 929–962.

6 BÜNZLI, J. C. G.; PIGUET, C. Taking advantage of luminescent lanthanide ions. **Chem. Soc. Rev.**, v. 34, p. 1048–1077, 2005.

7 BÜNZLI, J. C. G.; ELISEEVA, S. V. Intriguing aspects of lanthanide luminescence. **Chem. Sci.**, v. 4, p. 1939–1949, 2013.

8 CARLOS, L. D.; FERREIRA, R. A.; BERMUDEZ, V. D. Z.; RIBEIRO, S. J. Lanthanide-containing light-emitting organic–inorganic hybrids: A bet on the future. **Adv. Mater.**, v. 21, p. 509–534, 2009.

9 CARLOS, L. D.; PALACIO, F. (Eds.). **Thermometry at the nanoscale: Technique and selected applications.** Oxfordshire: Royal Society of Chemistry, 2016. 522 p.

10 BRITES, C. D. S.; LIMA, P. P.; SILVA, N. J. O.; MILLÁN, A.; AMARAL, V. S.; PALACIO, F.; CARLOS, L. D. Thermometry at the nanoscale. **Nanoscale**, v. 4, p. 4799–4829, 2012.

11 JAQUE, D.; VETRONE, F. Luminescence nanothermometry. **Nanoscale**, v. 4, p. 4301–4326, 2012.

12 ZOHAR, O.; IKEDA, M.; SHINAGAWA, H.; INOUE, H.; NAKAMURA, H.; ELBAUM, D.; ALKON, D. L.; YOSHIOKA, T. Thermal imaging of receptor-activated heat production in single cells**. Biophys. J.**, v. 74, p. 82–89, 1998.

13 ROHANI, S.; QUINTANILLA, M.; TUCCIO, S.; DE ANGELIS, F.; CANTELAR, E.; GOVOROV, A. O.; RAZZARI, L.; VETRONE, F. Enhanced luminescence, collective heating, and nanothermometry in an ensemble system composed of lanthanide-doped upconverting nanoparticles and gold nanorods**. Adv. Opt. Mater.**, v. 3, p. 1606–1613, 2015.

14 DEBASU, M. L.; BRITES, C. D.; BALABHADRA, S.; OLIVEIRA, H.; ROCHA, J.; CARLOS, L. D. Nanoplatforms for plasmon-induced heating and thermometry. **ChemNanoMat**, v. 2, p. 520–527, 2016.

15 MECKLENBURG, M.; HUBBARD, W. A.; WHITE, E. R.; DHALL, R.; CRONIN, S. B.; ALONI, S.; REGAN, B. C. Nanoscale temperature mapping in operating microelectronic devices. **Science**, v. 347, p. 629–632, 2015.

16 YARIMAGA, O.; LEE, S.; HAM, D. Y.; CHOI, J. M.; KWON, S. G.; IM, M.; KIM, S.; KIM, J.-M.; CHOI, Y. K. Thermofluorescent conjugated polymer sensors for nano- and microscale temperature monitoring. **Macromol. Chem. Phys.**, v. 212, p. 1211–1220, 2011.

17 BRITES, C. D. S.; XIE, X.; DEBASU, M. L.; QIN, X.; CHEN, R.; HUANG, W.; ROCHA, J.; LIU, X.; CARLOS, L. D. Instantaneous ballistic velocity of suspended Brownian nanocrystals measured by upconversion nanothermometry. **Nat. Nanotechnol**., v. 11, p. 851–856, 2016.

18 ZHANG, F. Upconversion nanoparticles for thermal sensing. In: _____. **Photon Upconversion Nanomaterials.** Berlin: Springer-Verlag, 2015. chap. 10, p. 343–374.

19 MENEZES, L. D. S.; de ARAÚJO, C. B.; Optically detected thermal effects in rare-earth doped materials for host characterization, thermometric devices, nanothermometry and biothermometry. **J. Braz. Chem. Soc.**, v. 26, p. 2405–2417, 2015.

20 LIU, R.-S. (Ed.). **Phosphors, up conversion nano particles, quantum dots and their applications.** Singapore: Springer, 2016. v. 2, 882 p.

21 ROCHA, U.; JACINTO, C.; KUMAR, K.; LOPEZ, F. J.; BRAVO, D.; SOLE, J. G.; JAQUE, D. Real-time deep-tissue thermal sensing with sub-degree resolution by thermally improved Nd^{3+}:LaF_3 multifunctional nanoparticles. **J. Lumin.**, v. 175, p. 149–157, 2016.

22 NUNES, L. A. O.; SOUZA, A. S.; CARLOS, L. D.; MALTA, O. L. Neodymium doped fluoroindogallate glasses as highly-sensitive luminescent non-contact thermometers, **Opt. Mater**., v. 63, p. 42–45, 2016.

23 PENG, H.; STICH, M. I.; YU, J.; SUN, L. N.; FISCHER, L. H.; WOLFBEIS, O. S. Luminescent europium(III) nanoparticles for sensing and imaging of temperature in the physiological range. **Adv. Mater.**, v. 22, p. 716–719, 2010.

24 SUZUKI, M.; TSEEB, V.; OYAMA, K.; ISHIWATA, S. Microscopic detection of thermogenesis in a single HeLa cell. **Biophys. J.**, v. 92, p. L46–L48, 2007.

25 OYAMA, K.; TAKABAYASHI, M.; TAKEI, Y.; ARAI, S.; TAKEOKA, S.; ISHIWATA, S.; SUZUKI, M. Walking nanothermometers: spatiotemporal temperature measurement of transported acidic organelles in single living cells. **Lab Chip**, v. 12, p. 1591–1593, 2012.

26 TAKEI, Y.; ARAI, S.; MURATA, A.; TAKABAYASHI, M.; OYAMA, K.; ISHIWATA, S.; TAKEOKA, S.; SUZUKI, M. A nanoparticle-based ratiometric and self-calibrated fluorescent thermometer for single living cells. **ACS Nano**, v. 8, p. 198–206, 2014.

27 SHAHI, P. K.; SINGH, A. K.; SINGH, S. K.; RAI, S. B.; ULLRICH, B. Revelation of the technological versatility of the $Eu(TTA)_3Phen$ complex by demonstrating energy harvesting, ultraviolet light detection, temperature sensing, and laser applications. **ACS Appl. Mater. Interfaces**, v. 7, p. 18231–18239, 2015.

28 SHAHI, P. K.; SINGH, A. K.; RAI, S. B.; ULLRICH, B. Lanthanide complexes for temperature sensing, UV light detection, and laser applications. **Sens. Actuators, A**, v. 222, p. 255–261, 2015.

29 NOCKEMANN, P.; BEURER, E.; DRIESEN, K.; VAN DEUN, R.; VAN HECKE, K.; VAN MEERVELT, L.; BINNEMANS, K. Photostability of a highly luminescent europium β-diketonate complex in imidazolium ionic liquids. **Chem. Commun.**, v. 0, p. 4354–4356, 2005.

30 PAGNOT, T.; AUDEBERT, P.; TRIBILLON, G. Photostability study of europium dibenzolymethide embedded in polystyrene this filmes with high concentration. **Chem. Phys. Lett.**, v. 322, p. 572–578, 2000.

31 KAI, J.; FELINTO, M. C. F. C.; NUNES, L. A. O.; MALTA, O. L.; BRITO, H. F. Intermolecular energy transfer and photostability of luminescence-tuneable multicolour PMMA films doped with lanthanide-β-diketonate complexes. **J. Mater. Chem.**, v. 21, p. 3796–3802, 2011.

32 QUIRINO, W.; REYES, R.; LEGNANI, C.; NÓBREGA, P. C.; SANTA-CRUZ, P. A.; CREMONA, M. Eu-β-diketonate complex OLED as UV portable dosimeter. Synth. Met., v. 161, p. 964–968, 2011.

33 SOUSA, F. L. N.; MOJICA-SÁNCHEZ, L. C.; GAVAZZA, S.; FLORENCIO, L.; VAZ, E. C. R.; SANTA-CRUZ, P. A. Printable UV personal dosimeter: sensitivity as a function of DoD parameters and number of layers of a functional photonic ink. **Mater. Res. Express**, v. 3, p. 045701, 2016.

34 WEI, C.; WEI, H.; YAN, W.; ZHAO, Z.; CAI, Z.; SUN, B.; MENG, Z.; LIU, Z.; BIAN, Z.; HUANG, C. Water-soluble and highly luminescent Europium(III) complexes with favorable photostability and sensitive pH response behavior. **Inorg. Chem.**, v. 55, p. 10645–10653, 2016.

35 LIU, Y.; QIAN, G. D.; WANG, Z. Y.; WANG, M. Q. Temperature-dependent luminescent properties of Eu-Tb complexes synthesized in situ in gel glass. **Appl. Phys. Lett.**, v. 86, p. 071907, 2005.

36 MARCINIAK, Ł.; BEDNARKIEWICZ, A.; STEFANSKI, M.; TOMALA, R.; HRENIAK, D.; STREK, W. Near infrared absorbing near infrared emitting highly-sensitive luminescent nanothermometer based on Nd^{3+} to Yb^{3+} energy transfer. **Phys. Chem. Chem. Phys.**, v. 17, p. 24315–24321, 2015.

37 BRITES, C. D. S.; LIMA, P. P.; SILVA, N. J. O.; MILLÁN, A.; AMARAL, V. S.; PALACIO, F.; CARLOS, L. D. A luminescent molecular thermometer for long-term absolute temperature measurements at the nanoscale. **Adv. Mater.**, v. 22, p. 4499–4504, 2010.

38 GORRIS, H. H.; ALI, R., SALEH, S. M.; WOLFBEIS, O. S. Tuning the dual emission of photon-upconverting nanoparticles for ratiometric multiplexed encoding. **Adv. Mater.**, v. 23, p. 1652–1655, 2011.

39 CERÓN, E. N.; ORTGIES, D. H.; DEL ROSAL, B.; REN, F.; BENAYAS, A.; VETRONE, F.; MA, D.; SANZ-RODRÍGUEZ, F.; SOLÉ, J. G.; JAQUE, D.; RODRÍGUEZ, E. M. Hybrid nanostructures for high-sensitivity luminescence nanothermometry in the second biological window. **Adv. Mater**., v. 27, p. 4781–4787, 2015.

40 CHEN, D.; LIU, S.; WAN, Z.; JI, Z. EuF_3/Ga_2O_3 Dual-Phase Nanostructural Glass Ceramics with Eu^{2+}/Cr^{3+} Dual-Activator Luminescence for Self-Calibrated Optical Thermometry. **J. Phys. Chem. C**, v. 120, p. 21858–21865, 2016.

41 CHEN, D.; WAN, Z.; ZHOU, Y.; ZHOU, X.; YU, Y.; ZHONG, J.; DING, M.; JI, Z. Dual-phase glass ceramic: structure, dual-modal luminescence, and temperature sensing behaviors. **ACS Appl. Mater. Interfaces**, v. 7, p. 19484–19493, 2015.

42 CHEN, D.; WAN, Z.; LIU, S. A highly sensitive dual-phase nanoglass-ceramics self-calibrated optical thermometer. **Anal. Chem.**, v. 88, p. 4099–4106, 2016.

43 CHEN, D.; WAN, Z.; ZHOU, Y. Dual-phase nano-glass-ceramics for optical thermometry. **Sensors and Actuators B**, v. 226, p. 14–23, 2016.

44 XU, M.; CHEN, D.; HUANG, P.; WAN, Z.; ZHOU, Y.; JI, Z. A dual-functional upconversion core@ shell nanostructure for white-light-emission and temperature sensing. **J. Mater. Chem. C**, v. 4, p. 6516-6524, 2016.

45 MARCINIAK, L.; BEDNARKIEWICZ, A. Nanocrystalline NIR-to-NIR luminescent thermometer based on Cr^{3+},Yb^{3+} emission. **Sensors and Actuators B**, v. 243, p. 388–393, 2017.

46 MARCINIAK, L.; BEDNARKIEWICZ, A.; KOWALSKA, D.; STREK, W. A new generation of highly sensitive luminescent thermometers operating in the optical window of biological tissues. **J. Mater. Chem. C**, v. 4, p. 5559–5563, 2016.

47 ZHOU, J.; LIU, Z.; LI, F. Upconversion nanophosphors for small-animal imaging. **Chem. Soc. Rev.**, v. 41, p. 1323–1349, 2012.

48 HEMMER, E.; QUINTANILLA, M.; LÉGARÉ, F.; VETRONE, F. Temperature-induced energy transfer in dye-conjugated upconverting nanoparticles: a new candidate for nanothermometry. **Chem. Mater.**, v. 27, p. 235–244, 2015.

49 LI, Z.; ZHANG, Y.; JIANG, S. Multicolor core/shell-structured upconversion fluorescent nanoparticles. **Adv. Mater.**, v. 20, p. 4765–4769, 2008.

50 LI, C.; HOU, Z.; DAI, Y.; YANG, D.; CHENG, Z.; MA, P.; LIN, J. A facile fabrication of upconversion luminescent and mesoporous core–shell structured β-$NaYF_4$:Yb^{3+}, Er^{3+}@$mSiO_2$ nanocomposite spheres for anti-cancer drug delivery and cell imaging. **Biomater. Sci.**, v. 1, p. 213–223, 2013.

51 KOSTIV, U.; JANOUŠKOVÁ, O.; ŠLOUF, M.; KOTOV, N.; ENGSTOVÁ, H.; SMOLKOVÁ, K.; JEŽEK, P.; HORÁK, D. Silica-modified monodisperse hexagonal lanthanide nanocrystals: synthesis and biological properties. **Nanoscale**, v. 7, p. 18096–18104, 2015.

52 MOLINA, C.; DAHMOUCHE, K.; MESSADDEQ, Y.; RIBEIRO, S. J. L.; SILVA, M. A. P.; DE ZEA BERMUDEZ, V.; CARLOS, L. D. Enhanced emission from Eu(III) β-diketone complex combined with ether-type oxygen atoms of di-ureasil organic-inorganic hybrids. **J. Lumin.**, v. 104, p. 93–101, 2003.

53 DEBASU, M. L.; ANANIAS, D.; PASTORIZA-SANTOS, I.; LIZ-MARZÁN, L. M.; ROCHA, J.; CARLOS, L. D. All-in-one optical heater-thermometer nanoplatform operative from 300 to 2000 K based on Er^{3+} emission and blackbody radiation. **Adv. Mater.**, v. 25, p. 4868–4874, 2013.

54 BRITES, C. D. S.; MILLÁN, A.; CARLOS, L. D. Lanthanides in luminescent thermometry. In : BÜNZLI, J. C. G., PECHARSKY, V. K. (Eds.). **Handbook on the physics and chemistry of rare earths.** Amsterdam: Elsevier B.V., 2016. v. 49, p. 339–427.

55 VETRONE, F.; NACCACHE, R.; ZAMARRON, A.; SANZ-RODRIGUEZ, F.; MAESTRO, L. M.; RODRIGUEZ, E. M.; JAQUE, D.; SOLE, J. G.; CAPOBIANCO, J. A. Temperature sensing using fluorescent nanothermometers. **ACS Nano**, v. 4, p. 3254–3258, 2010.

56 SINGH, S. K.; KUMAR, K.; RAI, S. B. Multifunctional Er^{3+}-Yb^{3+} codoped Gd_2O_3 nanocrystalline phosphor synthesized through optimized combustion route. **Appl. Phys. B**, v. 94, p. 165–173, 2009.

57 BORISOV, S. M.; KLIMANT, I. New luminescent oxygen-sensing and temperature-sensing materials based on gadolinium(III) and europium(III) complexes embedded in an acridone-polystyrene conjugate. **Anal. Bioanal. Chem.**, v. 404, p. 2797–2806, 2012.

58 BORISOV, S. M.; WOLFBEIS, O. S. Temperature-sensitive europium(III) probes and their use for simultaneous luminescent sensing of temperature and oxygen. **Anal. Chem.**, v. 78, p. 5094-5101, 2006.

Chapter 7.

Upconversion nanocomposites for PDT

7.1. Introduction

Photodynamic therapy (PDT) is a minimally invasive, highly-selective and clinically approved modality for treatment of certain neoplastic and non-neoplastic pathologies. The PDT procedure consists simply of administering a photosensitizer (PS) drug followed by local irradiation at a specific wavelength. Photooxidative reactions are triggered in the presence of tissue oxygen, leading to the generation of reactive oxygen species, which are toxic to cells. These reactive species can cause serious damage to the cell membrane, mitochondria and nucleus, leading to cell death by apoptosis or necrosis, and thus destruction of the target tissue occurs.[1]

The Figure 7.1 shows a modified Jablonski diagram illustrating the photosensitization process. Upon irradiation, the PS absorbs a photon of light and is promoted from a ground singlet state (S_0) to a short-lived excited singlet state (S_1). The deactivation to the ground state may either occur by fluorescence emission (this property can be exploited for bioimaging), or by nonradiative internal conversion (loss of energy in the form of heat). The S_1 state may also proceed to the relatively long-lived triplet state (T_1) via intersystem crossing. Once in the T_1 state, the PS can undergo two reaction processes involving molecular oxygen, known as type I and type II reactions. Type I reaction consists of the interaction with a substrate in the biological environment (*i.e.* cell membrane or molecule) by transferring an electron or a proton to form a radical cation or anion, respectively. The formed ions react with oxygen to generate reactive oxygen species such as superoxide anion radicals, hydroxyl radicals, and hydrogen peroxides. Type II reaction occurs *via* energy transfer between the ground state of oxygen, which has triplet character, and the triplet state of PS molecule to give rise to singlet oxygen ($^1O_2$). This spin-allowed reaction presents a simpler mechanism, thus making the $^1O_2$ the main cytotoxic species responsible for the destruction of target cells. The $^1O_2$ generation can be detected by measuring phosphorescence emission at 1270 nm.[2]

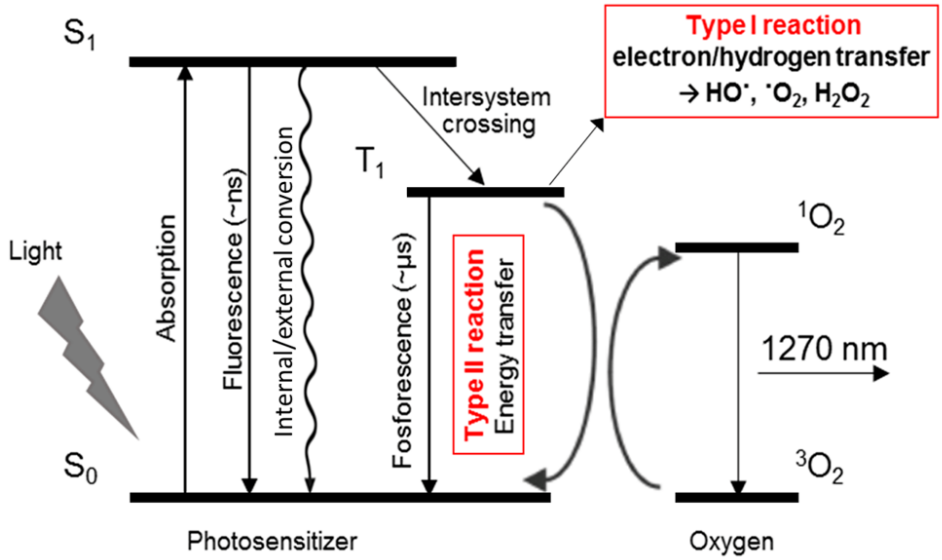

Figure 7.1. Jablonski diagram adapted for a typical photoactivation process. Vibrational sub-levels are not shown for reasons of clarity.

The clinical application of PDT is still not accepted as a first-line cancer treatment because of some limitations related to challenges in pharmaceutical formulation for efficient PS administration, the PS optical properties, the establishment of light dosimetry, and so forth.[3] The considerable hydrophobicity of PS molecules hampers their administration in a physiological environment. Toward this problem, researchers resorted to nanotechnology to develop drug delivery systems capable of encapsulating such hydrophobic molecules, carrying them in aqueous medium and delivering them to specific targets, thus enabling the use of PSs in therapy.[4]

Unfortunately, the visible light commonly used for the activation of PSs present low penetration depth into the tissues, limiting the volume of tissue treated in each session of therapy. Since the tissue transparency window is situated in the near infrared (NIR) region, luminescent materials that present the property of converting NIR light into visible light may be a solution to excite the photosensitive therapeutic agents indirectly under NIR radiation. The NIR excitation matches the biological transparency window, allowing deeper tissue penetration depth due to the minimal absorption and scattering of tissues at this spectral region. Materials based on trivalent lanthanide ions may present upconversion properties, *e.g.* visible emission obtained by excitation at NIR region in a multiphoton process. Additionally, NIR excitation enables sensitive detection without the usual interference from autofluorescence background.[5] Another advantage is the lower photo-damage potential because of the low-energy of NIR photons used for excitation.[6] For these reasons, lanthanide-based upconversion nanoparticles (UCNPs) are currently touted as being ideal candidates for bio-probes for biological labeling and imaging because of the possibility to excite their luminescence under NIR illumination and have attracted attention for PDT.[7,8]

In a previous work, we used bacterial cellulose (BC) membranes as a polymer-based drug delivery system for PDT skin cancer protocols. *In vitro* skin permeation and retention tests indicated that

the BC membranes incorporated with the PS chloroaluminum phtalocyanine (ClAlPc) offer adequate properties for topical administration of ClAlPc. In addition, BC-ClAlPc membranes did not present cytotoxic effects *in vitro* and singlet oxygen production was demonstrated.[9] As a sequel to this work, we have incorporated UCNPs in the BC membrane.[10] The UCNPs consisted of a YVO_4 host doped with Yb^{3+}:Ho^{3+} or Yb^{3+}:Er^{3+}. The synthesis and activator dopant ions were chosen to obtain high emission intensity in the wavelength range of ClAlPc absorption. The typical red emission of ClAlPc was observed in the presence of UCNPs under NIR excitation, because of the absorption of upconverted emission. However, this membrane-based system is limited by the localized topical administration of PS molecules. Additionally, the unfeasibility of particle dispersion hinders its cellular uptake and limits the optical pumping efficiency between UCNP and PS. The encapsulation of PSs in the surface of UCNPs in a core-shell design for facile particle dispersion is an alternative for adequate drug delivery to the target tissue, beyond the local site of application.

In this chapter, we describe the preparation of $NaGdF_4$:Yb^{3+}:Er^{3+}@SiO_2 nanoparticles containing the PSs eosin B (EO), erythrosine B (ER) and rose bengal (RB). Despite being hydrophilic molecules, such PSs may suffer from poor intracellular uptake ability.[11] The porous structure of silica shell was exploited as a carrier for PSs in aqueous solution.[12] Figure 7.2 displays the chemical structure of these halogen-xanthene dyes presenting a common ring skeleton. Rose bengal is commonly used as a corneal staining.[13,14] Erythrosin B is used as a red color additive for food and pharmaceutical forms.[15] Eosin B is extensively used in histology as the standard HE (haematoxylin and eosin) stain.[16] These dyes are well-known to exhibit intense absorption bands in the green region (480–550 nm), overlapping the Er^{3+} emission. Moreover, these molecules are well-known to produce singlet oxygen in high yield, allowing their use as active agents in PDT.[17–19] The capability of these core-shell nanocomposites in aqueous dispersion to generate singlet oxygen under near-infrared irradiation was investigated.

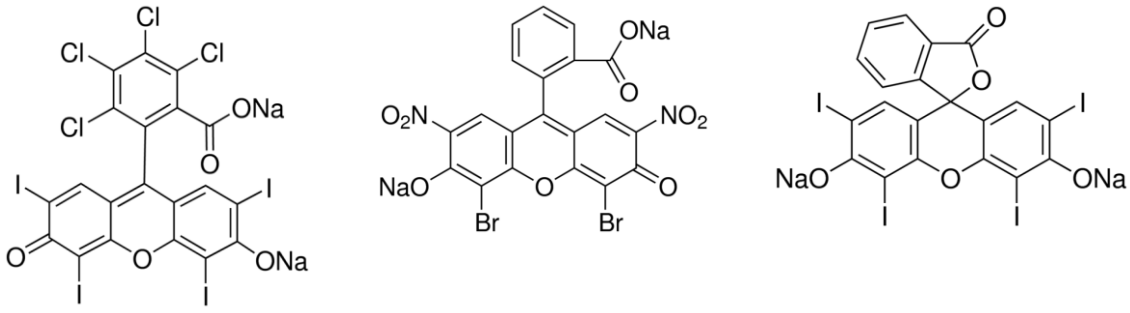

Rose bengal Eosin B Erythrosin B

Figure 7.2. Chemical structures of halogen-xanthene PDT sensitizers used in the present work.

7.2. Materials and methods

7.2.1 Materials

Eosin B, erythrosine B, rose bengal and deuterium oxide (D_2O) 99.9% were purchased from Sigma-Aldrich.

7.2.2. Preparation of UCNPs@SiO_2-PS

The $NaGdF_4$:Yb^{3+}:Er^{3+}@SiO_2 nanoparticles were prepared following the protocols described in Sections 5.2.2 and 5.2.3. The amino functionalization of UCNPs' silica shell was performed following the protocol described in Section 5.2.5.1.

Stock solutions of negatively- (UCNPs@SiO_2) and positively- (UCNPs@SiO_2–NH_2) charged nanoparticles were pipetted (1 mL) into microcentrifuge tubes. The solvent was separated by centrifugation at 846 RCF for 15 min. The particles were then redispersed by adding 1 mL of PS solutions in ethanol at three different concentrations (10, 50 and 100 nM) and placed on a thermomixer (Eppendorf) overnight at 800 rpm and 8 °C. The particles were centrifuged at 846 RCF for 15 min, washed twice with water and redispersed in 1.0 mL of D_2O for optical characterizations.

7.2.3. Characterization

The JEM-2100-JEOL LaB_6 (200 kV) transmission electron microscope (TEM) was used to determine the physical size of the particles and structural morphology. Zeta potential measurements of the particles dispersed in 1 mM MES buffer solution (pH = 6.1) were performed with a Malvern Zetasizer Nano ZS. The luminescence spectra were recorded using a FluoroLog fluorimeter from Horiba Jobin Yvon composed of a iHR-320i monochromator equipped with a photomultiplier tube (Hamamatsu, model R928P, spectral response: 185 to 900 nm), a InP/InGaAs array detector (Hamamatsu, model H10330-75, spectral response: 950 to 1700 nm) and a Xenon lamp as excitation source. The external 980 nm continuous wave diode laser (DMC Equipments, São Carlos-SP, Brazil) have been used as excitation source for the nanoparticles' upconversion luminescence spectra. UV-visible absorption spectroscopy was performed on a Varian Cary 5000 spectrophotometer.

The generation of singlet oxygen was determined by means of time-resolved phosphorescence analysis. Lifetime values were calculated from kinetic analysis phosphorescence decay curves of $^1O_2$ at 1270 nm. Decay curves were recorded with a time-resolved NIR fluorometer (Edinburgh Analytical Instruments) equipped with a pulsed Nd:YAG laser (Quantel) emitting at 1064 nm with a pulse duration of 5–8 ns and a repetition rate of 10 Hz. The Nd:YAG laser was coupled to a tunable optical parametric oscillator (OPO, Quantel, Rainboω), which converts the pumping wavelength in a tunable output to set the excitation wavelengths. The 516 nm, 526 nm and 549 nm excitation wavelengths were generated from the 1064 nm fundamental wavelength. An 850 nm long-pass filter (Thor Labs FGL850) was placed between laser excitation and sample. The emitted light was detected by photomultiplier (Hamamatsu Co. R5509)

cooled by liquid nitrogen (-80 °C) and raw data were processed using F910 acquisition software (Edinburgh Instruments). The measurements were performed in D_2O to increase the $^1O_2$ lifetime and under air-equilibrated conditions.

7.3. Results and discussion

Figure 7.3 shows TEM image of silica-coated UCNPs containing the photosensitizer ($NaGdF_4:Yb^{3+}:Er^{3+}@SiO_2$), demonstrating the hexagon shaped morphology of the core and the presence of a silica shell. The size distribution indicates the monodisperse core, with particle sizes of 29.0±1.7 nm, with a silica shell with thickness of about 4 nm.

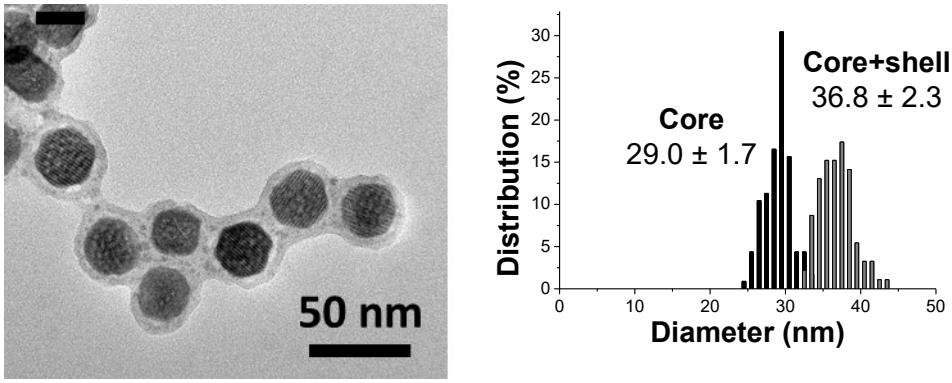

Figure 7.3. TEM image and particle-size distribution of UCNPs@SiO_2-PS.

The upconversion emission spectrum of UCNPs ($NaGdF_4:Yb^{3+}:Er^{3+}@SiO_2$) and the absorption spectra of PSs (EO, ER and RB in ethanolic solution) are shown in Figure 7.4. Assignments of the observed bands in the spectral regions of 510–536 nm, 536–575 nm and 625–700 nm have been already done in the discussions of Chapters 5 and 6 and correspond to Er^{3+} transitions $^4S_{3/2} \rightarrow {}^4I_{15/2}$, $^4F_{9/2} \rightarrow {}^4I_{15/2}$ and $^2H_{11/2} \rightarrow {}^4I_{15/2}$, respectively. The positions of maximum absorption are observed at 524 nm, 532 nm and 558 nm for EO, ER and RB respectively. The overlap between the green upconversion emission and the absorption band of the PSs suggests the potential to use of the visible light emitted by UCNPs under IR excitation to photosensitize the PS molecules.

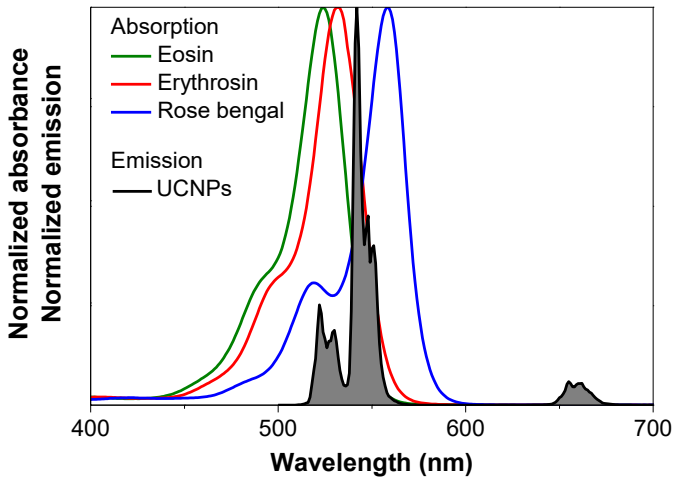

Figure 7.4. Absorption spectra of ethanolic solution of PSs (eosin, erythrosin and rose bengal) and upconversion emission spectrum of UCNPs ($NaGdF_4$:Yb^{3+}:Er^{3+}@SiO_2).

The incorporation of PS molecules in the silica shell of UCNPs was tested for negative- (UCNPs@SiO_2) and positively (UCNPs@SiO_2-NH_2) charged surfaces. The zeta potential of UCNPs@SiO_2 (-10.4 mV) became positive after amino functionalization (+26.0 mV). The incorporation yield of PSs into the silica shell of UCNPs from the PS solutions at different concentrations was studied. The absorption spectra were measured for the initial PS solutions and for the unbound PS that remained in the supernatant after incorporation and centrifugation (Figure 7.5). The unbound PS fraction for UCNPs@SiO_2 (red) present an absorbance close to that of the initial PS solution (black), suggesting low incorporation in the negatively charged UCNPs. The lower absorbance observed for UCNPs@SiO_2-NH_2 supernatants (blue) confirms that these negatively charged halogen-xanthene molecules are preferentially adsorbed in the positive surface, as expected.[20,21]

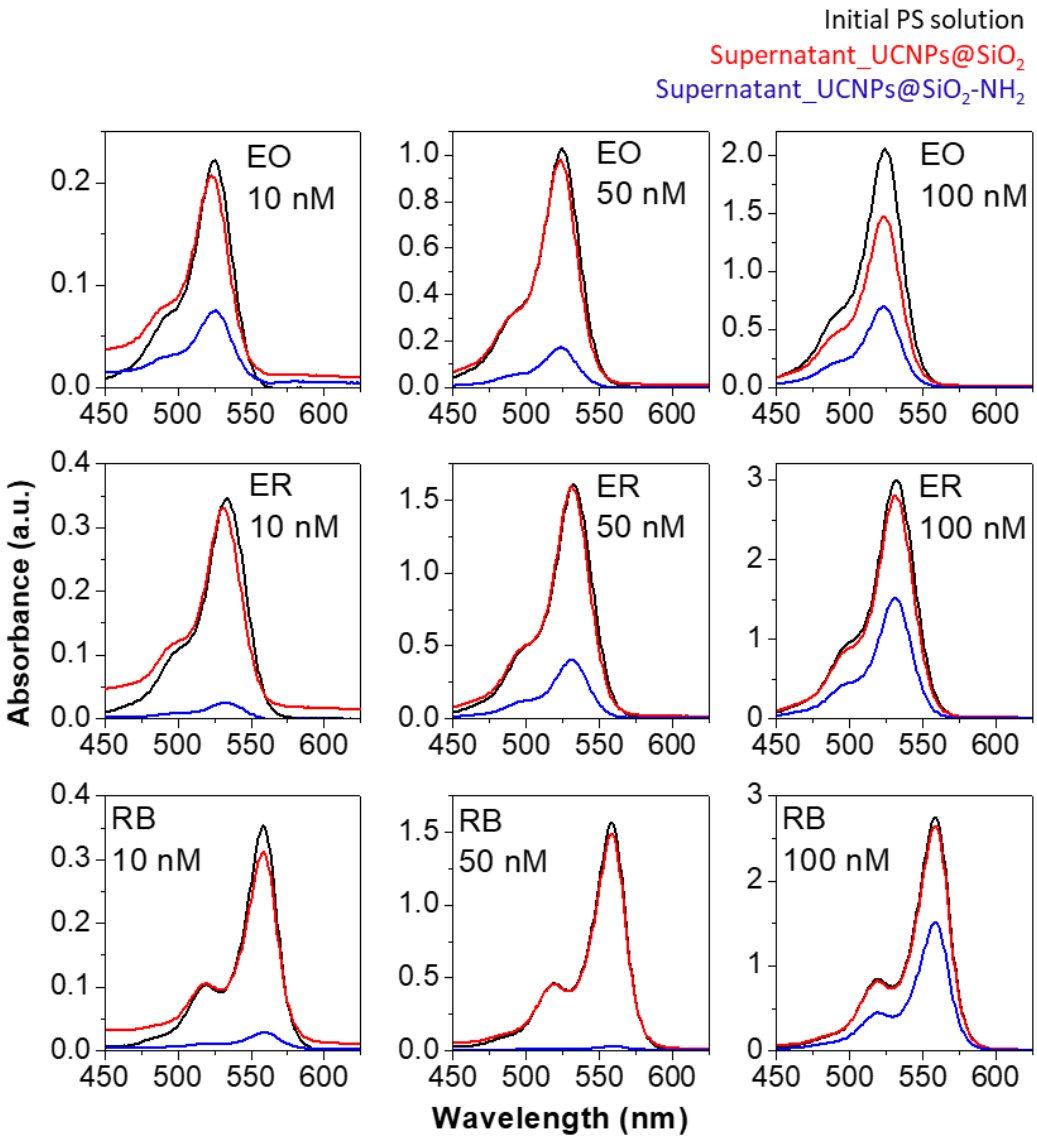

Figure 7.5. Absorption spectra for initial PS solution (black) and for the supernatant collected after incorporation in UCNPs@SiO_2 (red) and UCNPs@SiO_2-NH_2 (blue) for three initial PS concentrations (10, 50 and 100 nM).

Figure 7.5 shows the excitation and emission spectra of PS-containing UCNPs and the maximum excitation and emission wavelengths are presented on Table 7.1. The spectra of xanthene dyes at high concentrations (above ~10^{-5} M) may be shifted because of aggregation of molecules in solution.[22,23] Photosensitizers nanoencapsulated within the silica matrix have a maximum excitation and emission wavelengths similar to that for PS in the free form in solution, suggesting no aggregation of PS molecules.[12,18,23–26]

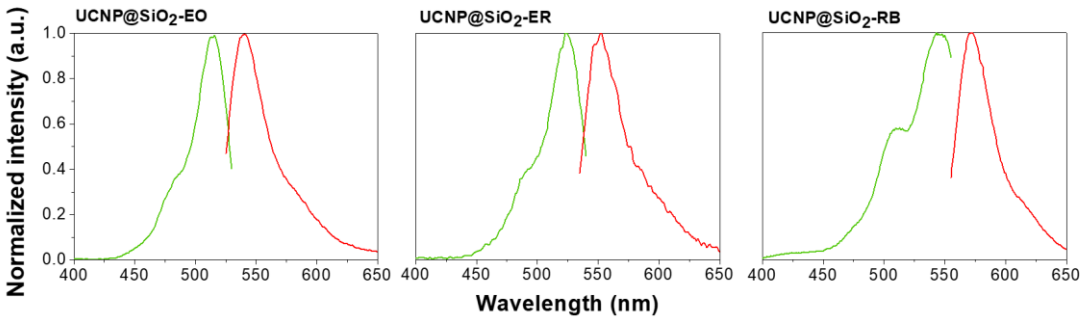

Figure 7.6. Excitation (green) and emission (red) spectra for PS-containing UCNPs@SiO_2.

Table 7.1. Maximum excitation and emission wavelengths for PS-containing UCNPs@SiO_2.

	λ_{exc} (nm)	λ_{em} (nm)
UCNPs@SiO_2-EO	516	540
UCNPs@SiO_2-ER	524	552
UCNPs@SiO_2-RB	543	572

The upconversion emission spectra (λ_{exc} 980 nm) of PS-containing UCNPs were acquired for different laser power levels and different concentrations of PS, as shown in Figure 7.7. The green upconversion emission attenuation for higher RB concentration is clearly observable. This effect is due to the increased absorption by RB in this wavelength region, since the maximum excitation of RB (543 nm) matches the maximum intensity or erbium emission (544 nm).

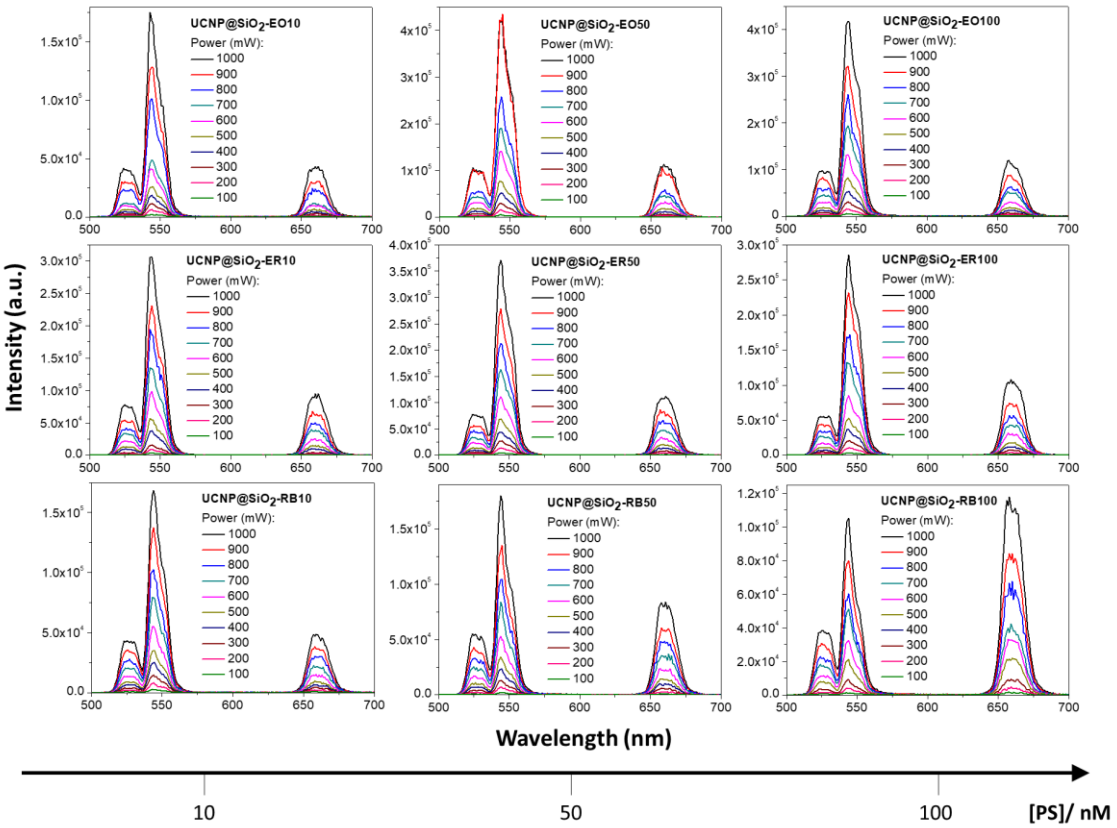

Figure 7.7. Upconversion emission spectra as a function of pumping power for PS-containing UCNPs@SiO_2 prepared with concentrations: 10, 50 and 100 nM.

The graph displayed in Figure 7.8 shows the red-to-green emission intensity ratio (calculated from the integrated areas) for PS-containing UCNPs@SiO_2 with different concentrations, as well as a control sample (PS-free UCNPs@SiO_2). Red-to-green band intensity ratios in the vicinity of ~0.3 were measured for the control sample as well as EO- and ER-containing nanoparticle suspensions in the three concentrations tested. In the case of RB, ratios of 0.5 and 1.1 were recorded for RB concentrations of 50 and 100 nM, respectively. This fact suggests that the green upconverted emission was absorbed by the RB molecules, suggesting the application of these UCNPs@SiO_2-RB composite systems in PDT processes activated by IR light.[10,27–31]

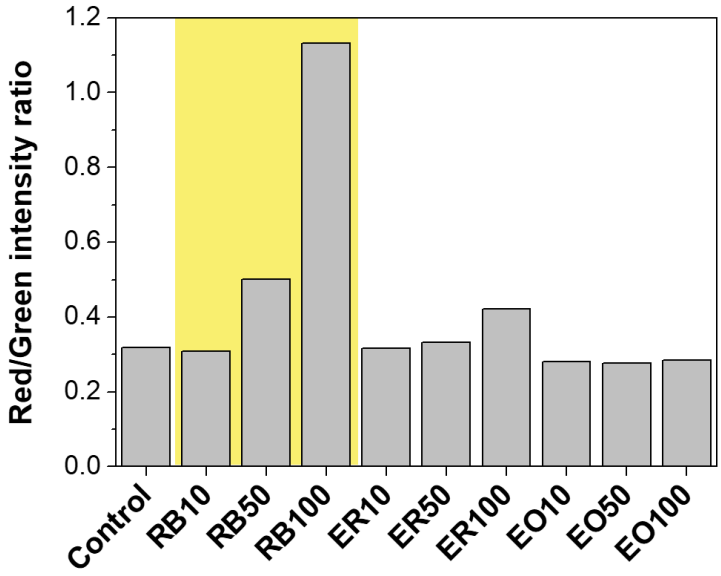

Figure 7.8. Red-to-green emission intensity ratio for UCNPs@SiO_2-PS (10, 50 and 100 are PS concentrations in nM). Control: PS-free UCNPs@SiO_2.

The singlet oxygen measurements were based on the direct determination of its characteristic phosphorescence at 1270 nm to determine the luminescence kinetics. PS solutions in deuterium oxide were used as control of singlet oxygen production. The concentration of control solutions was adjusted based on a maximum absorbance (then fixed as excitation wavelength) fixed at 0.3 in order to avoid any internal filter effects. Singlet oxygen decay curves and their exponential fit are presented in Figure 7.9 for UCNPs@SiO_2-PS (with concentrations: 10, 50 and 100 nM) dispersed in D_2O and free PS molecules dissolved in D_2O. The measured decay curves were fitted with a single exponential decay model (R^2 > 0.95), and the characteristic lifetimes are presented in Table 7.2. Singlet oxygen exhibits relatively long lifetimes in water (microseconds), long enough to diffuse over long distances and react with remote targets.[32] Lifetimes in solvents with OH vibrations are shorter (3.8 μs in H_2O) than in D_2O (62 μs).[33] The $^1O_2$ decay profiles and lifetime values are very similar among the three PSs for control solutions (~77 μs). The lifetimes obtained for nanoparticles are shorter (19-48 μs) compared to free PS in D_2O, which may be attributed to the presence of silica OH groups or to quenching due to the presence of an additional Ln^{3+} luminescent center. Moreover, traces of H_2O remaining in the silica pores could also be responsible for the shorter lifetimes. The higher PS concentration in UCNPs@SiO_2-RB100 may lead to an increased rate of triplet-triplet quenching, thus lowering the energy transfer to oxygen and further lowering $^1O_2$ lifetime.[34] Therefore, these data suggest that the silica carrier does not interfere with the production of singlet oxygen, an essential condition in the PDT process.

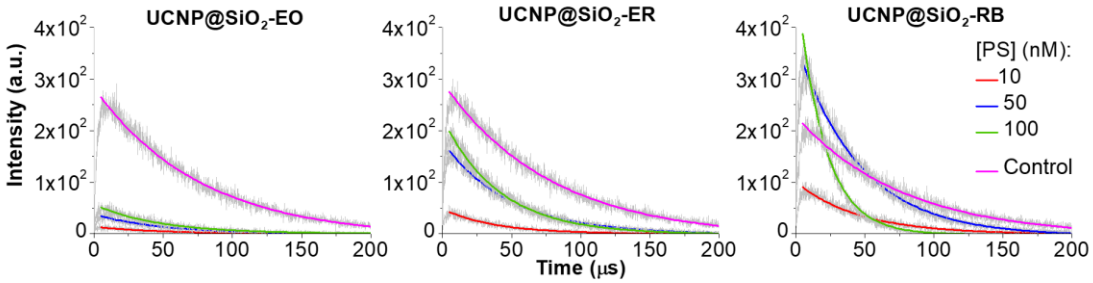

Figure 7.9. Singlet oxygen decay curve and exponential fit for EO (λ_{exc} 516 nm), ER (λ_{exc} 526 nm) and RB (λ_{exc} 549 nm) in UCNPs@SiO_2 dispersions in D_2O with PS concentrations of 10, 50 and 100 nM. Control: PS free in D_2O solution.

Table 7.2. Singlet oxygen lifetimes (τ) obtained from decay curves for the samples.

[PS] (nM)	τ (μs)		
	UCNPs@SiO_2-EO	UCNPs@SiO_2-ER	UCNPs@SiO_2-RB
10	48 ± 2	37.4 ± 0.5	45.67 ± 0.54
50	48 ± 1	47.9 ± 0.4	46.08 ± 0.28
100	45.8 ± 0.7	40.8 ± 0.3	19.78 ± 0.09
Control	76.6 ± 0.9	78.2 ± 0.8	77.18 ± 0.93

Control: PS free in D_2O solution.

7.4. Conclusions

In the present study, photosensitizers were added to the silica shell of UCNPs@SiO_2 and investigated as PDT agents. The use of IR excitation is advantageous for applications in biological systems, as it allows deeper penetration into tissues than the UV or visible radiation commonly used for direct excitation of PSs. The excitation bands of the PSs studied overlap with the UCNPs green emission. The study showed the feasibility of using the silica shell of UCNPs as a matrix for the incorporation of photosensitizers. The positively charged surface of UCNPs@SiO_2-NH_2 allowed for the incorporation of PSs in the silica shell with relatively high efficiency. The luminescent properties of UCNPs@SiO_2-PS prepared from starting solutions with different PS concentrations were studied. The green upconverted emission was absorbed by the RB molecules to a great extent than the other two PSs because of the favorable overlap between excitation band of RB (543 nm) and the maximum emission intensity of erbium (544 nm). The $^1O_2$ time-resolved phosphorescence measurements result in monoexponential lifetime decays with average lifetime of around 45 μs. The singlet oxygen generation capability of PSs is not defeeted by their incorporation in the silica shell of UCNPs. Therefore, UCNPs@SiO_2-PS offer potential as a photosensitizer for the treatment of neoplastic and non-neoplastic diseases susceptible to the photoactivation process.

References

1 DOLMANS, D. E. J. G. J.; FUKUMURA, D.; JAIN, R. K. Photodynamic therapy for cancer. **Nat. Rev. Cancer**, v. 3, n. 5, p. 380–387, 2003.

2 MACDONALD, I. J.; DOUGHERTY, T. J. Basic principles of photodynamic therapy. **J. Porphyr. Phthalocyanines**, v. 5, p. 105–129, 2001.

3 LUCKY, S. S.; SOO, K. C.; ZHANG, Y. Nanoparticles in photodynamic therapy. **Chem. Rev.**, v. 115, p. 1990–2042, 2015.

4 KONAN, Y. N.; GURNY, R.; ALLÉMANN, E. State of the art in the delivery of photosensitizers for photodynamic therapy. **J. Photochem. Photobiol.**, v. 66, p. 89–106, 2002.

5 TU, D.; ZHENG, W.; LIU, Y.; ZHU, H.; CHEN. X. Luminescent biodetection based on lanthanide-doped inorganic nanoprobes. **Coord. Chem. Rev.**, v. 273-274, p. 13–29, 2014.

6 YUAN, P.; LEE, Y. H.; GNANASAMMANDHAN, M. K.; GUAN, Z.; ZHANG, Y.; XU, Q. H. Plasmon enhanced upconversion luminescence of $NaYF_4$:Yb,Er@SiO_2@Ag core-shell nanocomposites for cell imaging. **Nanoscale**, v. 4, p. 5132–5137, 2012.

7 LIU, Q.; FENG, W.; LI, F. Water-soluble lanthanide upconversion nanophosphors: synthesis and bioimaging applications *in vivo*. **Coord. Chem. Rev.**, v. 273-274, p. 100–110, 2014.

8 CHENG, L.; WANG, C.; LIU, Z. Upconversion nanoparticles and their composite nanostructures for biomedical imaging and cancer therapy. **Nanoscale**, v. 5, p. 23–37, 2013.

9 PERES, M. F. S.; NIGOGHOSSIAN, K.; PRIMO, F. L.; SASKA, S.; CAPOTE, T. S. O.; CAMINAGA, R. M. S.; MESSADDEQ, Y.; RIBEIRO, S. J. L.; TEDESCO, A. C. Bacterial Cellulose Membranes as a Potential Drug Delivery System for Photodynamic Therapy of Skin Cancer. **J. Braz. Chem. Soc.**, v. 27, p. 1949–1959, 2016.

10 NIGOGHOSSIAN, K.; PERES, M. F. S.; PRIMO, F. L.; TEDESCO, A.C.; PECORARO, E.; MESSADDEQ, Y.; RIBEIRO, S. J. L. Infrared to visible up-conversion in biocellulose-yttrium vanadate nanoparticles composite membranes. Demonstration of chloroaluminum phthalocyanine light emission under up-converted light excitation. **Colloid and Interface Science Communications**, v. 2, p. 6–10, 2014.

11 FISCHER, E.; VARGA, F. Hepatic storage and biliary excretion of rose bengal in the rat. **Acta Physiol. Acad. Sci. Hung.**, v. 54, p. 89–94, 1979.

12 NECKERS, D. C. Rose bengal. **J. Photochem. Photobiol. A.**, v. 47, p. 1–29.

13 EFRON, N. Corneal staining. In: _____. **Contact lens complications.** 3rd ed. London: W.B. Saunders, 2012. chap. 16, p. 155–166.

14 FEENSTRA, R. P.; TSENG, S. C. Comparison of fluorescein and rose bengal staining. **Ophthalmology**, v. 99, p. 605–617, 1992.

15 ALLAM, K. V.; KUMAR, G. P. Colorants–the cosmetics for the pharmaceutical dosage forms. **Int. J. Pharm. Pharm. Sci.**, v. 3, p. 13–21, 2011.

16 APGAR, J. M.; JUARRANZ, A.; ESPADA, J.; VILLANUEVA, A.; CANETE, M.; STOCKERT, J. C. Fluorescence microscopy of rat embryo sections stained with haematoxylin-eosin and Masson's trichrome method. **J. Microsc.**, v. 191, p. 20–27, 1998.

17 GIANOTTI, E.; ESTEVÃO, B. M.; CUCINOTTA, F.; HIOKA, N.; RIZZI, M.; RENÒ, F.; MARCHESE, L. An efficient rose bengal based nanoplatform for photodynamic therapy. **Chem. Eur. J.**, v. 20, p. 10921–10925, 2014.

18 GANDIN, E.; LION, Y.; VAN DE VORST, A. Quantum yield of singlet oxygen production by xanthene derivatives. **Photochem. Photobiol.**, v. 37, p. 271–278, 1983.

19 PACZKOWSKI, J.; LAMBERTS, J. J. M.; PACZKOWSKA, B.; NECKERS, D. C. Photophysical properties of rose bengal and its derivatives (XII). **J. Free Radic. Biol. Med.**, v. 1, p. 341–351, 1985.

20 PELLOSI, D. S.; ESTEVÃO, B. M.; SEMENSATO, J.; SEVERINO, D.; BAPTISTA, M. S.; POLITI, M. J.; HIOKA, N.; CAETANO, W. Photophysical properties and interactions of xanthene dyes in aqueous micelles. **J. Photochem. Photobiol. A**, v. 247, p. 8–15, 2012.

21 CALORI, I. R.; PELLOSI, D. S.; VANZIN, D.; CESAR, G. B.; PEREIRA, P.; POLITI, M. J.; HIOKA, N.; CAETANO, W. Distribution of xanthene dyes in DPPC vesicles: Rationally accounting for drug partitioning using a membrane model. **J. Braz. Chem. Soc.**, v. 27, p. 1938–1948, 2016.

22 ROHATGI, K. K.; MUKHOPAD. A. K. Aggregation properties of anions of fluorescein and halofluorescein dyes. **J. Indian Chem. Soc.**, v. 49, p. 1310–1320, 1972.

23 XU, D.; NECKERS, D. C. Aggregation of rose bengal molecules in solution. **J. Photochem. Photobiol. A**, v. 40, p. 361–370, 1987.

24 KHAJEHPOUR, M.; TROXLER, T.; VANDERKOOI, J. M. Probing the Active Site of Trypsin with Rose Bengal: Insights into the Photodynamic Inactivation of the Enzyme. **Photochem. Photobiol.**, v. 80, p. 359–365, 2004.

25 CHAKRABORTY, M.; PANDA, A. K. Spectral behaviour of eosin Y in different solvents and aqueous surfactant media. **Spectrochim. Acta A**, v. 81, p. 458–465, 2011.

26 TERPETSCHNIG, E.; POVROZIN, Y.; EICHORST, J. Polarization standards. **J. Eichorst**, (Inc), 2002.

27 FU, Y.; LIU, H.; REN, Z.; LI, X.; HUANG, J.; BEST, S.; HAN, G. Luminescent $CaTiO_3$: Yb, Er nanofibers co-conjugated with Rose Bengal and gold nanorods for potential synergistic photodynamic/photothermal therapy. **J. Mater. Chem. B**, v. 5, p. 5128–5136, 2017.

28 LIANG, L.; CARE, A.; ZHANG, R.; LU, Y.; PACKER, N. H.; SUNNA, A.; QIAN, Y.; ZVYAGIN, A. V. Facile assembly of functional upconversion nanoparticles for targeted cancer imaging and photodynamic therapy. **ACS Appl. Mater. Interfaces**, v. 8, p. 11945−11953, 2016.

29 WANG, H.; HAN, R.-L.; YANG, L.-M.; SHI, J.-H.; LIU, Z.-J.; HU, Y.; WANG, Y.; LIU, S.-J.; GAN, Y. Design and synthesis of core−shell−shell upconversion nanoparticles for nir-induced drug release, photodynamic therapy, and cell imaging. **ACS Appl. Mater. Interfaces**, v. 8, p. 4416–442, 2016.

30 LU, S.; TU, D.; HU, P.; XU, J.; LI, R.; WANG, M.; CHEN, Z.; HUANG, M.; CHEN, X. Multifunctional nano-bioprobes based on rattle-structured upconverting luminescent nanoparticles. **Angew. Chem. Int. Ed.**, v. 54, p. 7915–7919, 2015.

31 LIU, K.; LIU, X.; ZENG, Q.; ZHANG, Y.; TU, L.; LIU, T.; KONG, X.; WANG, Y.; CAO, F.; LAMBRECHTS, S. A. G.; AALDERS, M. C. G.; ZHANG, H. Covalently assembled NIR nanoplatform for simultaneous fluorescence imaging and photodynamic therapy of cancer cells. **ACS Nano**, v. 6, p. 4054–4062, 2012.

32 NONELL, S.; FLORS, C. (Ed.). **Singlet oxygen: Applications in biosciences and nanosciences.** Cambridge: Royal Society of Chemistry, 2016. v. 2, 349 p.

33 STEINER, U. E. Fundamentals of photophysics, photochemistry, and photobiology. In: ABDEL-KADER, M. H. (Ed.). **Photodynamic therapy.** Heidelberg: Springer, 2014. chap. 2, p. 25–58.

34 DĚDIC, R.; VYKLICKÝ, V.; SVOBODA, A.; HÁLA, J. Singlet oxygen lifetime dependence on photosensitizer concentration in lipid films. **J. Lumin.**, v. 131, p. 442–444, 2011.

Chapter 8.

Conclusions

In summary, two main multifunctional systems were developed in this thesis work. The first one combined an optical heater and a temperature probe. The design was based on AuNSs with the surface decorated with UCNPs. AuNSs were used to produce heat when illuminated at their SPR band in the NIR aiming for the use of the produced heat to induce well-localized thermal damage of cancer cells in PTT. In this work we were able to measure the temperature increase induced by the AuNSs by monitoring the Yb^{3+}-Er^{3+} upconversion emission, showing the potential of the system for guiding PTT process, in which a temperature detector with high spatial resolution is necessary, to minimize the damage of surrounding tissues.

The second system developed is a dual-mode nanothermometer combined with an UV light sensor. These multifunctional nanoparticles displayed temperature-dependent emissions in the visible region from both UV pumped downshifting Eu^{3+} luminescence and NIR pumped Yb^{3+}-Er^{3+} upconversion. In addition, the Eu^{3+} emission intensity presented an exponential decay with exposure time and is therefore sensitive to the UV exposure dose, indicating its potential to guide UV light activated therapies.

Since both systems are essentially based on UCNPs of $NaGdF_4$ doped with the ions Yb^{3+}-Er^{3+}, the first part of the work was mainly focused on the synthesis conditions *via* thermal decomposition of fluoride precursors. The structure and morphology were investigated to establish the synthetic protocol to obtain monodisperse nanocrystals in the pure hexagonal phase, which is known to present higher emission intensity. The luminescence properties of cubic and hexagonal crystal phases were compared. The UCNPs in the hexagonal phase showed to be more suitable for application as a temperature sensor than the cubic phase, due to its lower red-to-green emission ratio and higher thermal sensitivity.

After studying the structural and optical properties of the hydrophobic oleate-capped nanocrystals, the phase transfer to aqueous media was necessary with regards to their intended use for biological applications. The surface of UCNPs was modified by coating with a thin silica shell. The method based on reverse microemulsion route was optimized to prevent silica interparticle polymerisation might otherwise affect water dispersability. Dynamic light scattering analysis of micellar systems at different stages of synthesis and of the final nanoparticles was performed. Optimized reaction parameters comprised: UCNPs initial concentration; surfactant and TEOS concentration, reaction time, centrifugation speed and catalyst (dimethyl ammonium or ammonium hydroxide). A uniform silica shell on the nanocrystal surface was obtained. The core-shell UCNPs presented the property of converting infrared

energy into visible light and offered suitable properties for application as a temperature sensor. Optical characterization in the vicinity of the physiological range revealing excellent temperature sensing linearity.

The next step was the coupling of UCNPs core-silica shell onto the surface of metal core-silica shell nanoparticles. Three strategies were investigated for the fabrication of UCNP-metal nanocomposites: (i) through a covalent ''click'' cycloaddition methodology;[1] (ii) based on electrostatic interaction between anionic UCNPs@SiO_2 and the positively charged metallic surface obtained by modification with the polyelectrolyte poly(diallyldimethylammonium chloride) (PDADMAC);[2] (iii) by functionalization of UCNPs@SiO_2 with amine groups. The latter coupling strategy showed the best results. However, the most important factor was the comparative size of the nanocomponents. Initially, silica coated silver nanoparticles with a silver core diameter of 70 nm were used to develop the synthesis protocol, but these studies were further extended to gold and silver nanostructures with different shapes (spheres, rods and shells). Ultimately, UCNPs@SiO_2 of about 40 nm could be successfully coupled with much larger gold nanoshells of around 300 nm.

The heating properties of the obtained AuNSs@UCNPs nanocomposites were demonstrated by irradiating the colloidal solution at different laser power to excite the SPR of Au and by measuring the Yb^{3+}-Er^{3+} upconversion emission spectra. In the presence of AuNSs the temperature reached around 40 °C. The multifunctional system behaved as a combined heater and a temperature sensor under NIR excitation.

The functionalities of the UCNPs@SiO_2 nanothermometers were then extended by adding a second active luminescent center. The attachment of a Eu^{3+}/tta complex to the silica shell was confirmed by the observation of the characteristic and unique luminescence properties (photoluminescence excitation and emission spectra), which agreed with data published in the literature for the well-known complex [$Eu(tta)_3(H_2O)_2$], and a composite that was prepared from an organic-inorganic hybrid host and the complex (presented in Figure 6.2). It must be said that the small amount of complex was not detectable by infrared vibrational spectroscopy or Raman spectroscopy. The Eu^{3+} emission spectrum of the obtained UCNPs@SiO_2–$Eu(tta)_3$ showed a broadening of emission lines compared to literature spectra. Such broadening in Eu^{3+} complexes when grafted to different surfaces is well known and is mostly due to the contribution of coordinating groups from the surface (silanol groups for example) to the Eu^{3+} first coordination sphere in the case of the complex considered here by substituting for water molecules in the Eu^{3+} coordination sphere. To support this hypothesis, results obtained by us before for a completely different host (organic-inorganic "ureasil" hybrid) are instructional. In that case, the contribution from oxygen atoms to the host is considered. The identification of the grafted species as "$Eu(tta)_3$" could be considered oversimplifying, but we do think that it introduces important errors or misconceptions. The exact formulation for the grafted species should be established in a systematic spectroscopic study for each host studied.

Temperature determination using the Eu^{3+} system presents a drawback compared to Er^{3+}, since a nonratiometric thermal parameter is used. Ratiometric methods are indeed more reliable and present

many advantages in comparison with those based on the intensity of only one transition due to their self-referencing feature. However, the Eu^{3+}-based thermal sensor proposed in this work presented suitable features, such as the linear luminescence thermal dependence and quite high thermal sensitivity.

However, we did not observe UV degradation of the Eu^{3+}-based thermometer, since a linear correlation was observed, whereas the correlation is known to be exponential in the case of UV degradation. The effects of UV degradation on luminescence intensity decay are different for each sensor due to different mechanisms. For UV sensing, degradation of the tta ligand hinders the antenna effect and is thus responsible for the intensity exponential decay. Meanwhile, for temperature sensing, the Eu^{3+} energy levels are directly influenced by effects such as: redistribution of electronic state population, quenching mechanisms and non-radiative transitions. It must be pointed out that the incident UV power was 5x larger for the degradation tests compared with the temperature measurements.

Optimization of UV light activated therapeutic processes is necessary to minimize the detrimental effects associated with overexposure, such as DNA damage. We proposed a UV light sensor to ensure that the effective dose is delivered to the patient by controlling the exposure time for a given UV power density. As UV light intensity and experimental setup were constant over the measurement time, it is possible to determine the time required to reduce the Eu^{3+} emission intensity to 50% (from the curve presented in Figure 6.7). This result may be extrapolated for different power density values.

This thesis brings original and interesting results concerning the use of lanthanides for sensing applications based on lanthanide luminescence, and stimulates the study of multifunctional materials. The new materials presented in this work could find interesting applications in luminescent thermometry under ultraviolet or near-infrared excitation, UV light sensing, as well as photodynamic therapy and photothermal therapy. The new nanoplatforms are dispersible in aqueous environment, thus being attractive for applications in nanomedicine for guiding light activated therapies to avoid photodamage and overheating of normal tissues.

References

1 ASSELIN, J.; ROY, C.; BOUDREAU, D.; MESSADDEQ, Y.; BOUCHAREB, R.; MATHIEU, P. Supported core–shell nanobiosensors for quantitative fluorescence imaging of extracellular pH. **Chem. Commun.**, v. 50, p. 13746–13749, 2014.

2 MA, Z.; DING, T. Bioconjugates of glucose oxidase and gold nanorods based on electrostatic interaction with enhanced thermostability. **Nanoscale Res. Lett.**, v. 4, p. 1236–1240, 2009.